Behavior of nanoparticles on surfaces exposed to EUV environments

Citation for published version (APA):
Shefer, D. (2023). *Behavior of nanoparticles on surfaces exposed to EUV environments*. [Phd Thesis 1 (Research TU/e / Graduation TU/e), Applied Physics and Science Education]. Eindhoven University of Technology.

Document status and date:
Published: 05/10/2023

Document Version:
Publisher’s PDF, also known as Version of Record (includes final page, issue and volume numbers)

Please check the document version of this publication:

• A submitted manuscript is the version of the article upon submission and before peer-review. There can be important differences between the submitted version and the official published version of record. People interested in the research are advised to contact the author for the final version of the publication, or visit the DOI to the publisher's website.
• The final author version and the galley proof are versions of the publication after peer review.
• The final published version features the final layout of the paper including the volume, issue and page numbers.

Link to publication

General rights
Copyright and moral rights for the publications made accessible in the public portal are retained by the authors and/or other copyright owners and it is a condition of accessing publications that users recognise and abide by the legal requirements associated with these rights.

- Users may download and print one copy of any publication from the public portal for the purpose of private study or research.
- You may not further distribute the material or use it for any profit-making activity or commercial gain
- You may freely distribute the URL identifying the publication in the public portal.

If the publication is distributed under the terms of Article 25fa of the Dutch Copyright Act, indicated by the “Taverne” license above, please follow below link for the End User Agreement:

www.tue.nl/taverne

Take down policy
If you believe that this document breaches copyright please contact us at:

openaccess@tue.nl

providing details and we will investigate your claim.

Download date: 08. Feb. 2024

Behavior of nanoparticles on surfaces exposed to EUV environments

PROEFSCHRIFT

ter verkrijging van de graad van doctor aan de Technische Universiteit Eindhoven,
op gezag van de rector magnificus prof.dr. S.K. Lenaerts, voor een commissie
aangewezen door het College voor Promoties, in het openbaar te verdedigen op
donderdag 5 oktober 2023 om 16:00 uur

door

Dmitry Shefer

geboren te Novosibirsk, Rusland

Dit proefschrift is goedgekeurd door de promotoren en de samenstelling van de promotiecommissie is als volgt:

Voorzitter:	prof.dr. C. Storm
Promotoren:	dr.ir. J. Beckers prof.dr. V. Y. Banine
Promotiecommissieleden:	dr.ir. J. Beckers prof.dr V. Y. Banine prof.dr.ir. G. M. W. Kroesen prof.dr.ir. J. P. H. Benschop (Universiteit Twente, TN) prof.dr. F. Bijkerk (Universiteit Twente, Science and Technology) prof.dr. D. N. Ruzic (University of Illinois at Urbana-Champaign, Department of Nuclear, Plasma and Radiological Engineering)

Het onderzoek of ontwerp dat in dit proefschrift wordt beschreven is uitgevoerd in overeenstemming met de TU/e Gedragscode Wetenschapsbeoefening.

Behavior of nanoparticles on surfaces exposed to EUV environments

Dmitry Shefer

Preparation. LaTeX documentation system in OverLeaf.
Printing. Print Service / proefschriftmaken.nl
Cover photo. Evgeny Boyko

A catalog record is available from the Eindhoven University of Technology Library.
ISBN. 978-90-386-5852-0

Financial support. This work was sponsored by ASML and conducted in CIM labs.

Keywords: particles, morphology, hydrogen plasma, laser scattering, tin allotropy

Summary

Extreme ultraviolet (EUV) lithography is a process for high-volume manufacturing of integrated circuits with linear dimensions of the finest elements around 10 nm. Lithography machines have critical components, like a reticle (mask), with specific and stringent cleanliness requirements for contaminating particles larger than 20 nm in size on their surface. At the same time, the formation of EUV-induced hydrogen plasma is an unavoidable part of the technology. Tiny contaminating particles from the Laser-Produced Plasma (LPP) source and from surrounding surfaces become exposed to EUV-induced hydrogen plasma. As for many cases, the resulting electrical forces exerted on the particles are too small to explain the observation of plasma-induced particle release. Some hypotheses - regarding hydrogen-etching of particle material, hydride formation, and hydrogen diffusion into the particle's bulk causing its embrittlement are proposed and further investigated in this thesis.

When pulses of EUV radiation propagate through low-pressure background hydrogen, the gas is partly ionized and an EUV-induced hydrogen plasma is produced. The EUV-induced hydrogen plasma is transient in time and space and thus can be reasonably divided into two parts: a hot ballistic part (a few microseconds after the pulse, when energetic electrons reach surfaces without collisions) and EUV afterglow which slowly propagates from the EUV beam through a scanner under the ambipolar diffusion. In this work, we experimentally reproduced a hydrogen plasma with energy parameters close to EUV afterglow, but 100 times more intense in terms of ion flux.

The work in this thesis reports on experimental studies regarding fragmentation, morphology, and bulk alterations of micrometer-sized particles. Scanning Electron Microscopy (SEM) accompanied by Focused Ion Beam (FIB) cross-sectioning was utilized for the demonstration of plasma influence on particle morphology. An extensive set of materials that is relevant for EUV lithography was studied, including particles made of Sn, Pb, PbO, CeO, Ni, Si, stainless steel, and others. The particles were purchased in powder form and were nominally 0.5–30 µm in size. The change of particle adhesion to a substrate exposed to plasma and within a directed flushing gas flow was studied by adapting Laser Light Scattering (LLS) as an in-situ diagnostic. We used particle sizes in the micrometer range to enable the measurement of the plasma effect on a large ensemble of similar particles (100—10,000) using LLS accompanied by long-distance microscopy. These adhesion changes were measured by LLS and correlated with the SEM/FIB measurements. From the experiments, it was concluded that the morphology of most of the particles was changed. Particles with high permittivity of hydrogen radicals and ions tend to form gaseous bubbles under the surface, while others can form stable volatile hydrides toward etching, following chemical sputtering. A more thorough study of the behavior of tin in hydrogen plasma as a function of temperature and ion dose revealed the previously unknown ability of plasmas to affect its allotropy form. Tin is allotropic, meaning that it has different crystal structures at different temperatures and pressures. Two of its allotrope forms exist at near-normal conditions (white Sn is a metal and gray tin is a semiconductor). SEM photographs of particles after the plasma exposure clearly depict the cracking of particles, which must be atypical for normal plastic deformation of metals. The direct measurements, using Energy-Dispersive X-ray (EDX) microscopy, as well as Transmission Electron Microscopy (TEM) of tin particles on a thin slice (lamella) after exposure to hydrogen plasma did not reveal any gray tin. This result can be associated with intermediate exposure to open air between the measurements. However, the cracking mechanism hints at the presence of a gray tin phase inside of white tin particles for plasma exposures up to 60–80 °C.

All plasma exposures were conducted using an Electron Cyclotron Resonance (ECR) plasma source. The ECR source generates plasma with merely comparable electron and ion profiles to the EUV afterglow. However, the interaction energies of ions in sheathes of these two plasmas are very similar which allows us to use the ECR source as a cheaper backup of EUV afterglow. The use of the ECR plasma for these studies was intended to accelerate all accumulation effects compared to EUV-induced plasma afterglow by about 100 times (in terms of a flux of ions) which can be translated to acceleration by 100 times in EUV exposure time compared to normal conditions in an EUV scanner.

Overall, from the obtained results it can be concluded that a wide range of materials is susceptible to the influence of hydrogen plasma. The primary contribution to contamination arises from the chemical interaction of particles with hydrogen radicals and ions. Further investigation of this issue is absolutely essential for the advancement of nanolithography.

Contents

Chapter 1

Introduction

1.1 EUV lithography

Extreme Ultraviolet (EUV) lithography has emerged as a state-of-the-art technology in semiconductor manufacturing, enabling the production of cutting-edge devices with shrinking feature sizes. Traditional optical lithography faces limitations as feature sizes approach the nanometer scale, necessitating the adoption of innovative techniques like EUV lithography to achieve the demands of modern chip fabrication.

In order to reduce the size of integrated circuits and increase their density, modern nanolithography has reduced the wavelength of the illuminating radiation and overcome the Rayleigh criterion limit [1]. The technology process involves the optical transfer of the future chip image from the reticle onto a wafer patterned with photoresist. ASML's current nanolithography is capable of printing 3 nm images. EUV pulses are generated by the excitation of tin (Sn) droplets by a highly energetic CO_2 laser at a frequency of about 50 Hz [2]. Tin re-emits light in EUV spectra mostly at a wavelength of 13.5 nm, i.e. the photon energy is 92 eV. At the same time, the use of hydrogen gas is necessary for EUV lithography for a number of reasons, such as the protection of reflective mirrors from carbon deposition, as well as the usage of gas flows to repel contaminants. When the EUV radiation passes through the rarefied hydrogen (at low pressure such as 5 Pa, which is a typical pressure used in EUV environments [3]), it is partially ionized with the concomitant production of energetic primary electrons, which, in turn, when colliding with gas molecules, causes cascade ionization, thereby forming an EUV-induced hydrogen plasma.

While EUV lithography is now beyond the promise of being a major driver in innovation and essential for the semiconductor nodes, it also presents a unique challenge related to contamination.

1.1.1 Particle contamination

The term "particle contamination" in the context of EUV lithography refers to the deposition of micro and nanoparticles on critical components of the scanner, such as a collector mirror, projection optics, a reticle (integrated circuit photomask), a wafer, etc. A reticle is particularly vulnerable to particles larger than 20 nm [2, 4, 5, 6]. The consequences of such particle contamination on the reticle can lead to recurring lithographic projection defects on printed integrated circuits (Figure 1.1) [7]. Therefore, reducing the number of these defects has a significant impact on performance and product yield.

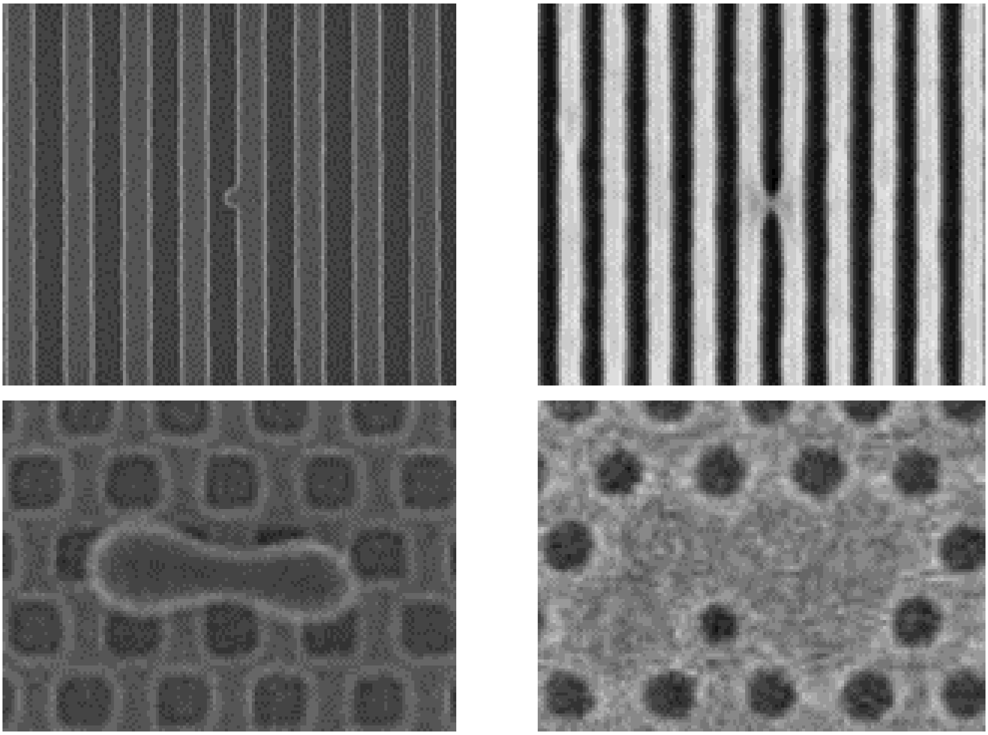

Figure 1.1: The SEM images of a contaminant deposited on a reticle (chip mask) and the resulting defect on a wafer. The image has been taken with permission from [8].

EUV-induced plasma influences contamination. Experimental studies conducted on EUV scanners during EUV lithography operations have shown a correlation between the presence of EUV-induced plasma and the number of defects on the reticle (Figure 1.2). EUV-induced plasma is an unavoidable part of modern nanolithography, and currently, there are no adequate alternatives to using hydrogen as the working gas. Hence, it is necessary to address the emerging contamination issues by investigating the interaction between EUV-induced plasma and materials, as well as micro/nanoparticles in particular, to prevent such events from occurring.

The retention of particles on a surface in a hydrogen plasma environment is important. Exposure to hydrogen plasma can alter the morphology of micro-particles [9, 10, 11]. Moreover, morphology alteration can weaken the adhesion force of particles to the surface and result in their spontaneous detachment. Adhesion loss is the most noticeable effect of plasma on particles as even small amounts of particles can have a significant impact on scanner imaging defects.

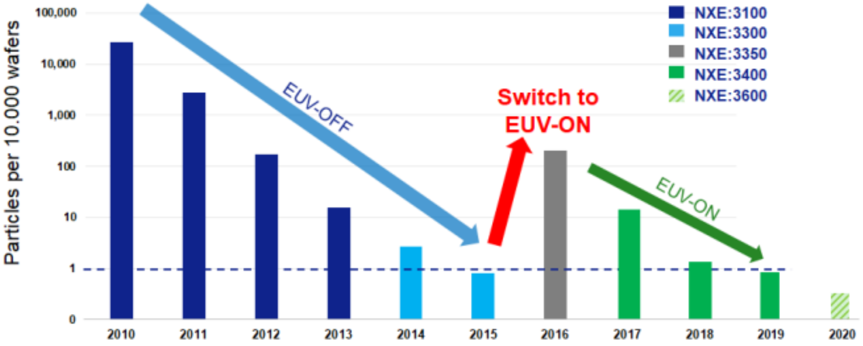

Figure 1.2: The downward trend in the number of defects achieved at ASML over the years. It is clearly seen the contamination outbreak after the integration of the EUV source. The image is taken with permission from [7].

Contamination control is not only of concern for EUV lithography. The phenomena can occur in nature. For example, NASA's study of the lunar and Mars surfaces confirmed suspended dust without settling [12, 13, 14]. This effect is attributed to UV or plasma charging and may have a negative impact since there are several technologies that are sensitive to plasma-induced particle release. For example, the mobility of micrometer-sized particles in plasma presents a challenge to solar panel longevity. Another example is the nuclear fusion plasma vessels (e.g. in ITER). Plasma-facing walls may release particles that deteriorate the gas mix. In case of loss of vacuum accidents (LOVa), this can result in an outbreak of radioactive particles [15, 16]. Finally, material surface activation may be of interest for catalyst and etching reactions [17]. With respect to all these applications, the study of the behavior of micrometer-sized particles attached to a surface and interacting with plasma is important. To enable further studies, the development of new in-situ diagnostic tools is highly relevant.

1.2 Plasma as a natural phenomenon

Plasma is the "fourth state of matter" and is conceived as ionized gas in which its components are carrying a charge while remaining quasineutral. Plasmas are not confined to laboratory settings but occur naturally in various contexts. One of the most prominent examples of natural plasmas is found in stars, including our Sun. The immense temperatures and pressures within stellar cores lead to the ionization of atoms and the formation of the plasma state, enabling nuclear fusion reactions and the release of vast amounts of energy. Furthermore, plasma phenomena extend beyond stellar environments and can be observed in lightning discharges, auroras, and in the Earth's ionosphere.

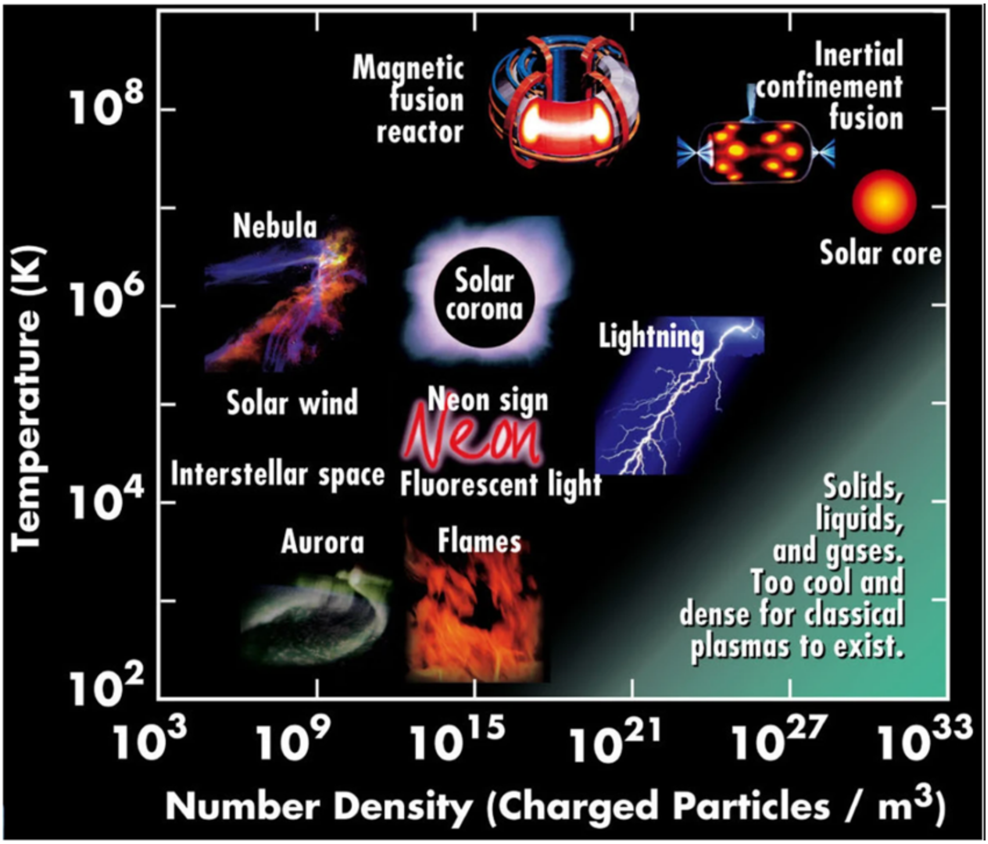

Figure 1.3: The plasma universe. The image has been taken from [18] with permission from the author.

In addition to celestial phenomena, plasma also plays a major role in many terrestrial processes. For example, the Earth's ionosphere, a region of the upper atmosphere, contains ionized gases that interact with solar radiation and influences radio wave propagation. Plasma discharges occur during thunderstorms, resulting in the dramatic display of lightning bolts. Moreover, plasmas are integral to many technological applications, including fluorescent lights, plasma displays, and plasma etching in semiconductor manufacturing (Figure 1.3).

In this work, we will focus on a low-temperature (around 10^4 K or 1 eV) and low-density plasma (10^{14}–10^{17} m^{-3}) which is of great interest in fields where it can be applied for commercial purposes. Our area of interest is non-thermal plasma ($T_e \gg T_i$, where T_e and T_i are the electron and ion temperatures respectively). The introduction of energy to a gas (f.e. thermally or by means of EUV irradiation), leads to an increase in the kinetic energy of its molecules, atoms, and electrons, resulting in a higher frequency of collisions. As soon as the kinetic energy overcomes the bond energy of the electrons in an outer orbit, the atoms, and molecules become ionized. When the kinetic energy surpasses the bond energy of the electrons in the outer orbit, ionization occurs, converting atoms and molecules into charged species composed of ions and electrons or plasma.

The equilibrium[1] plasma consists of stationary ions and fast electrons. Electrons, due to their much lower mass ($>$ 1000 times lower) compared to ions, have higher mobility and therefore may more quickly redistribute themselves in plasma than ions, screening charge fluctuations or probe charges and maintaining quasi-neutrality.

Plasmas have some unique properties compared to normal gases. First of all, they are electrically conductive, and at the same time, they are quasi-neutral due to the net equal amount of positive and negative charges. As a result, plasmas possess collective behavior, with electrons and ions responding collectively to electromagnetic forces. Furthermore, the increased potential energy of the constituent species of the plasma might be released during chemical or physical interaction with materials.

In the study of the contamination problem, the complex interaction between plasma and various materials plays a crucial role. As we delve into the specific realm of EUV lithography, the role of EUV-induced hydrogen plasma becomes paramount. By understanding the unique attributes of EUV-induced hydrogen plasma, we can reduce contamination and contribute to the advancement of cutting-edge semiconductor manufacturing processes.

1.3 EUV-induced plasma

Reproducing EUV-induced plasma in laboratory conditions is expensive and requires significant efforts to maintain the operation of EUV sources. Therefore, in our study, we employed an Electron Cyclotron Resonance (ECR) plasma source [19], which is easy to use. The generated ECR RF-powered plasma is comparable to the energy spectrum of electrons in EUV-induced plasma, but not entirely. For example, the ECR source produces plasma with an electron temperature reported in a range of 2–5 eV, while EUV afterglow is generally considered to have only 1 eV [20]. Furthermore, the mean ion kinetic energy of ECR is higher. However, taking into account the potential energy of hydrogen radicals and ions, the kinetics of the interaction of plasma with a surface is very similar. Thus, the results obtained using ECR plasma can be extrapolated to effects in EUV afterglow.

Furthermore, EUV-induced plasma is weak (in the reticle region, EUV power ranges from 50–100 W, with only a portion of it converted into plasma), and significant time is required to accumulate stress in the particles. In reports on the number of particles found on the reticle, the average time between contamination outbreaks spans several months. One particle for 100,000 wafers is what ASML has currently achieved in lithography [7]. To expedite this process, a hydrogen plasma with a density of 100

---

[1] The equilibrium term in this context means that plasma parameters remain constant over time

times higher than in EUV-induced plasma was utilized.

Thus, the ECR hydrogen plasma chosen for the experiments represents the conditions of the afterglow of the EUV-induced hydrogen plasma with a boost factor. The EUV-induced plasma fluxes of ions and radicals require hundreds of hours of exposure to cause particle release in the vicinity of critical surfaces [7]. Having a hundredfold more intense flux and approximately 5 times higher energy of the ions compared to the EUV-induced plasma [20], the experiment conditions are expected to accelerate the effects on the particles by approximately 100 times. Working with low pressures, temperatures, and under supersaturation conditions of dissolved hydrogen, we assume the scaling is reasonable [21].

1.4 Research questions

The knowledge gaps in EUV-induced plasma-material interaction and retention of micrometer-sized particles on a surface have been described earlier in this chapter. Related to these gaps in knowledge, this section outlines three research questions that aim to contribute to an increased understanding of the underlying physical mechanisms and reduce contamination.

Understanding volatile hydride formation on the surface and processes in the bulk of the particle caused by hydrogen plasma will help to reduce these gaps.

Research question I: What is the effect of hydrogen plasma on the structure and morphology of micrometer-sized particles?

Another research need is to monitor the morphology and adhesion of the particles in-situ. While studying the adhesion of the particles to the surface, non-invasive methods are required. Removing weakly adhered particles to the surfaces into the air when approaching post-exposure methods like SEM, AFM, TEM, XRD, and others will recover a particle's native oxide. The van der Waals force acts on a scale of a few manometers. Thus, the conditional cannot be a reliable source of information anymore.

Research question II: Can Laser Light Scattering (LLS) be used as an in-situ diagnostic method to monitor the adhesion and morphology of particles exposed to plasma?

The final research line focuses on the tension created by inflated hydrogen bubbles in the particle bulk. It is believed that inner tension can potentially create the conditions for the allotrope transformation of tin particles.

Research question III: Can hydrogen plasma cause allotrope transformations of tin micrometer-sized particles?

1.5 Thesis structure

The structure of this thesis as follows:

- **Chapter 2** is linked to the research line I. The chapter describes the morphology and bulk changes of the hydrogen plasma-exposed Sn, Pb, and PbO micrometer-sized plasma particles. Thermodynamics of hydride formation is demonstrated and the mechanisms of plasma influence on the morphology and bulk of the particles are suggested.
- **Chapter 3** is linked to the research line II and proposes using the LLS method for in-situ monitoring the behavior of micrometer-sized particles on a substrate exposed to plasma or to a directed gas jet. The calibration of the method is discussed. The method was applied to a broad set of materials. The interpretation of the LLS graphs for studying the morphology change in plasma is discussed.
- **Chapter 4** is linked to the research line III and represents the study of plasma-assisted allotrope forms transformation of tin particles. The mechanism of plasma influence on allotropy and its impact on contamination is discussed.

The thesis is completed with a conclusive chapter. **Conclusion** summarizes the results, concludes this thesis by relating the results to the research questions, and promotes perspectives of future research.

1.6 Bibliography

[1] Christian Wagner and Noreen Harned. Euv lithography: Lithography gets extreme. *Nature Photonics*, 4:24–26, 1 2010.

[2] Mark van de Kerkhof and et al. Advanced particle contamination control in EUV scanners. In Kenneth A. Goldberg, editor, *Extreme Ultraviolet (EUV) Lithography X*, volume 10957, pages 191 – 203, 2019.

[3] Mark A. van de Kerkhof, Ernst Galutschek, Andrei Yakunin, Selwyn Cats, and Christian Cloin. Particulate and molecular contamination control in EUV-induced h2-plasma in EUV lithographic scanner. In Carlos E. Soares, Eve M. Wooldridge, and Bruce A. Matheson, editors, *Systems Contamination: Prediction, Control, and Performance 2020*. SPIE, August 2020.

[4] Roderik van Es and et al. EUV for HVM: towards an industrialized scanner for HVM NXE3400B performance update. In Kenneth A. Goldberg, editor, *Extreme Ultraviolet (EUV) Lithography IX*, volume 10583, pages 102–113, 2018.

[5] Beckers, Ven, Horst, Astakhov, and Banine. EUV-induced plasma: A peculiar phenomenon of a modern lithographic technology. *Applied Sciences*, 9(14):2827, July 2019.

[6] Nan Fu, , Yanxiang Liu, Xiaolong Ma, and Zhanfeng Chen. EUV lithography: State-of-the-art review. *Journal of Microelectronic Manufacturing*, 2(2):1–6, 2019.

[7] Mark A. van de Kerkhof, Andrei Yakunin, Vladimir Kvon, Ferdi van de Wetering, Selwyn Cats, Luuk Heijmans, Andrey Nikipelov, Adam Lassise, and Vadim Banine. Understanding EUV-induced plasma and application to particle contamination control in EUV scanners. In Nelson M. Felix and Anna Lio, editors, *Extreme Ultraviolet (EUV) Lithography XI*. SPIE, March 2020.

[8] Richard Bruls. ASML internal report, 2017.

[9] C. Quiros, J. Mougenot, G. Lombardi, M. Redolfi, O. Brinza, Y. Charles, A. Michau, and K. Hassouni. Blister formation and hydrogen retention in aluminium and beryllium: A modeling and experimental approach. *Nuclear Materials and Energy*, 12:1178–1183, August 2017.

[10] S. Ratynskaia, A. Bortolon, and S. I. Krasheninnikov. Dust and powder in fusion plasmas: recent developments in theory, modeling, and experiments. *Reviews of Modern Plasma Physics*, 6(1), August 2022.

[11] Dmitry Shefer, Andrey Nikipelov, Mark Kerkhof, Zahra Marvi, Vadim Y Banine, and J Beckers. The impact of hydrogen plasma on the structure and morphology of tin and lead micrometer sized particles. *Journal of Physics D: Applied Physics*, January 2023.

[12] Mihály Horányi. Charged dust dynamics in the solar system. *Annual Review of Astronomy and Astrophysics*, 34:393–398, 1996.

[13] A. A. Sickafoose, J. E. Colwell, M. Horányi, and S. Robertson. Experimental levitation of dust grains in a plasma sheath. *Journal of Geophysical Research: Space Physics*, 107, 2002.

[14] Nima Afshar-Mohajer, Chang-Yu Wu, Jennifer Sinclair Curtis, and James R. Gaier. Review of dust transport and mitigation technologies in lunar and martian atmospheres. *Advances in Space Research*, 56(6):1222–1241, September 2015.

[15] Panagiotis Tolias, S. Ratynskaia, M Angeli, G. De Temmerman, Dario Ripamonti, G Riva, I. Bykov, Andrey Shalpegin, Ladislas Vignitchouk, Frédéric Brochard, Kirill Bystrov, Sébastien Bardin, and Andrey Litnovsky. Dust remobilization in fusion plasmas under steady state conditions. *Plasma Physics and Controlled Fusion*, 58:025009, 02 2016.

[16] S. Brezinsek and et al. Plasma–wall interaction studies within the EUROfusion consortium: progress on plasma-facing components development and qualification. *Nuclear Fusion*, 57(11):116041, August 2017.

[17] Costel Cojocaru, A Senger, and Francois Le Normand. A nucleation and growth model of vertically-oriented carbon nanofibers or nanotubes by plasma-enhanced catalytic chemical vapor deposition. *Journal of nanoscience and nanotechnology*, 6:1331–8, 06 2006.

[18] Xu Yan, Jiting Ouyang, Chenyang Zhang, Zhongfang Shi, Boran Wang, and Kostya (Ken) Ostrikov. Plasma medicine for neuroscience—an introduction. *Chinese Neurosurgical Journal*, 5(1), October 2019.

[19] Kouun Shirai, Takashi Iizuka, and Shun ichi Gonda. Electric probe measurements in an ECR plasma CVD apparatus. *Japanese Journal of Applied Physics*, 28(Part 1, No. 5):897–902, may 1989.

[20] T. H. M. van de Ven, P. Reefman, C. A. de Meijere, R. M. van der Horst, M. van Kampen, V. Y. Banine, and J. Beckers. Ion energy distributions in highly transient EUV induced plasma in hydrogen. *Journal of Applied Physics*, 123(6):063301, February 2018.

[21] R. Kirchheim and A. Pundt. Hydrogen in metals. In *Physical Metallurgy*, page 25972705. Elsevier, 2014.

Chapter 2

The impact of hydrogen plasma on the structure and morphology of Sn, Pb and PbO micrometer-sized particles

Preface. The stability of micrometer-sized particles in hydrogen plasma is essential for Extreme Ultraviolet (EUV) lithography and the application of hydrogen plasma etching. We experimentally investigated the morphological evolution of tin (Sn), lead (Pb), and lead (II) oxide (PbO) micrometer-sized particles on a surface that is exposed to a low-pressure hydrogen plasma and the impact of morphology on adhesion of the particle. Post-exposure particle cross-sections obtained by a Scanning Electron Microscope (SEM) accompanied by a Focused Ion Beam (FIB) demonstrated a significant influence of hydrogen plasma exposure on both the surface and the bulk material of the particles. Chemical sputtering on the surface and accumulation of pressurized hydrogen bubbles in cavities in the bulk material are the main drivers of the morphological changes. These mechanisms may influence the adhesion of particles to the surface through the introduction of asperities, increase of contact spot area, or fragmentation after the accumulation of mechanical stress.

The results of this chapter were partially published as D. Shefer, A. Nikipelov, M. van de Kerkhof, Z. Marvi, V. Banine, and J. Beckers, *The impact of hydrogen plasma on the structure and morphology of tin and lead micrometer-sized particles*, Journal of Physics D: Applied Physics, vol. 56, n. 8, February 2023. DOI: 10.1088/1361-6463/acb3d9.

2.1 Introduction

This section covers the study of particles at the micro level using Scanning Electron Microscopy (SEM), accompanied by Focused Ion Beam (FIB), and Energy-Dispersive X-ray (EDX) spectroscopy. The combined use of these methods enables the examination of surface and internal particle changes before and after exposure to plasma, as well as tracking their chemical composition.

To determine the conditions under which hydrogen plasma (or EUV-induced plasma) is capable of detaching a particle from a surface, primary forces that retain the particle on a surface and forces exerted by plasma must be examined.

This chapter is organized as follows. Section 2.2 introduces the basics of the plasma and estimation of the particle adhesion force to a substrate. Section 2.3 describes the experimental methods used in this chapter including the description of the plasma setup, deposition methods, and details of SEM/FIB measurements. Section 2.4 presents the results of the conducting experiments and hypothetical explanations. Section 2.5 denotes a discussion of the results. Finally, Section 2.6 draws the conclusion of this chapter.

2.2 Adhesion of a particle to substrate in plasma

2.2.1 Plasma basics

In order to characterize the interaction of plasma with particles, we have to introduce some important parameters. In plasma physics, a parameter that describes the length at which electrons screen the Coulomb interaction between charged species in a plasma environment is called the Debye length. In other words, the Debye length implies that deviations from neutrality might occur on a length that is smaller than a certain length. For Maxwellian electron energy distribution, the Debye length is expressed as

$$\lambda_D = \sqrt{\frac{\epsilon_0 k_B T_e}{e^2 n_e}} \tag{2.1}$$

where k_B is the Boltzmann constant, and n_e is the concentration of electrons or ions respectively. The characteristic time scale at which electrons are spatially reorganized for effective screening is $\tau_e = 1/\omega_{pe}$, where $\omega_{pe} = \sqrt{e^2 n_e/\epsilon_0 m_e}$ is the plasma frequency, ϵ_0 is the permittivity of free space, m_e is the mass of an electron. Similarly, for ions $\tau_i = 1/\omega_{pi}$, where $\omega_{pi} = \sqrt{e^2 n_i/\epsilon_0 m_i}$. The typical values for conditions of our experiments is $\lambda_D \cong 0.1$ mm, $\tau_e \cong 10^{-9}$ s, $\tau_i \cong 10^{-7}$ s.

The high velocity of electrons enables them to leave the bulk plasma and pull the ions behind until the resulting electric field keeps the remaining electrons in and increases the motion of ions out of the plasma bulk. This mechanism of spreading plasma in volume or, particularly, in the vacuum chamber, is called ambipolar diffusion. Under this mechanism, plasma can reach surfaces far from its source.

2.2.2 Plasma sheath

When plasma comes into contact with a solid surface, the higher mobility of electrons leads to their loss to the surface, which subsequently charges negatively, while the boundary zone of the plasma charges positively due to excess concentration of less mobile ions. The resulting electric field repels the approaching electrons and attracts ions from the plasma. After the equilibrium of electron and ion fluxes to the surface is established, a zone, which is depleted of electrons, is formed near the negatively charged surface. This zone is called the plasma sheath.

The properties of the plasma sheath can vary greatly depending on the characteristics of the plasma. For plasma in local thermal equilibrium, with electron energy distribution obeying Maxwellian law, the plasma sheath is determined mainly by the electron temperature and electron concentration. The space-charge region in the area of the interaction of plasma with a surface is shown in Figure 2.1.

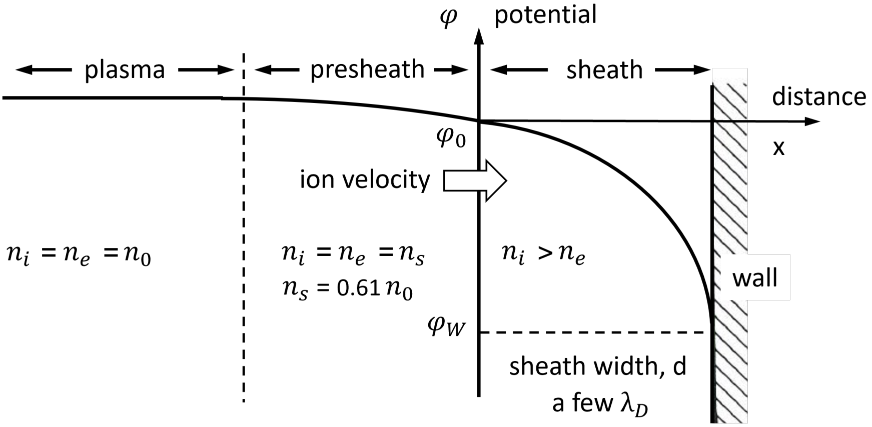

Figure 2.1: Schematic drawing of the plasma sheath and pre-sheath with the potential.

The width of the plasma sheath d for a not-biased wall is a few Debye lengths and may be estimated as [1]:

$$d \cong 3 \cdot \lambda_{D_e} = 3 \cdot \sqrt{\frac{\epsilon_0 k_B T_e}{e^2 n_e}} \tag{2.2}$$

The typical value of the plasma sheath in our conditions is a few hundred micrometers. The plasma-to-wall potential is the function of the electron temperature:

$$\varphi_w = T_e \cdot ln \left(\frac{m_i}{2\pi m_e} \right)^{1/2} - \frac{1}{2} T_e \tag{2.3}$$

where the term presheath Bohm potential $\frac{1}{2}T_e$ is added [2]. As $n_e n_i = n_s^2$, the concentration of electrons and ions in the pre-sheath can be estimated by the function

$$n_s = n_o \cdot e^{\varphi_w / T_e} \tag{2.4}$$

The dominant hydrogen ion in our experiments is H_3^+ ($m_i = 3$ amu)[1]. Thus, the kinetic collision energy of this ion accelerated in the plasma sheath equals [3]

$$E_k = \frac{q}{e}\varphi_w = 4 \cdot T_e \tag{2.5}$$

Thus, for a plasma with an electron temperature of 1 eV, the kinetic energy E_k of H_3^+ ions is 4 eV. However, the energy transfer by the impinging ions is not limited to the kinetic energy. The potential ionization energy $R_H = 13.6$ eV carried by each ion must be taken into account. Thus the total energy of the ion is [3]

$$E_{total} = \frac{q}{e}\varphi_w + R_H = 4 \cdot T_e + 13.6\ eV \tag{2.6}$$

which exceeds or comparable to many common characterized energies of a solid body like work function ($\cong$ 5 eV), molecular bond energy ($\cong$ 3–10 eV), photoionization energy ($\cong$ 10 eV), atom displacement energy ($\cong$ 15 eV). In other words, even a so-called cold plasma, described above, is energetically capable of altering the surface.

The electron/ion flux toward the surface is given by

$$\Gamma_{i,e} = n_s v_T = n_s \sqrt{\frac{eT_e}{m_i}} \tag{2.7}$$

For a plasma with the concentration $n_0 = 10^{14}$ m^{-3} the ion flux results in around 10^{18} m^{-2}. The radical flux is assessed to be 10 to 100 times higher than the concentration of H_3^+ ions or 10^{19}–10^{20} m^{-2}.

Finally, the electric field which is directly perpendicular to the surface near the wall is approximately equal to [1]

$$E_s \cong -2.5\sqrt{\frac{en_eT_e}{\epsilon_0}} \tag{2.8}$$

Now let's examine the forces acting on the particle which is located on a substrate within the plasma sheath.

2.2.3 Adhesion force

A spontaneous detachment of particles from surfaces under external conditions (for example, when placed in plasma) poses a serious problem for several technologies with contamination control. It is generally accepted that the process of dust adhesion to a surface is called "adhesion" while the interaction of particles with each other is called "autohesion" [4]. The detachment of dust particles depends on the magnitude and direction of the force applied to a particle. If the normal force is applied to a contaminated surface (for instance, under the influence of a plasma sheath), then for the particles to be attached, we must have $F_{det} > F_{ad}$ where F_{det} and F_{ad} are the detachment and adhesion forces respectively. At the same time, F_{det} is generally

---

[1] The used plasma source will be described later in this chapter.

considered to be a normal force, perpendicular to the surface. However, tangential forces, which exert practically no influence when in plasma, require our attention, as we use the directed gas flow (flushing) in the experimental part of this thesis.

In general, a particle on a surface exposed to low-temperature plasma is subjected to several forces: electrical, molecular, and gravitational forces, and under some conditions, plasma exposure is known to cause the release of nanometer and micrometer-sized particles from surfaces, as studied by Heijmans [5]. Plasma charges particles and surfaces negatively and induces repelling force between the particle and the surface. However, molecular forces such as the van der Waals (vdW) force, capillary forces due to residual water, and the chemical interaction between the particle and the surface prevent the particle from removal. In Figure 2.2 the force balance is depicted for a conductive particle on a conductive substrate without an electrical connection between them. Where F_m – is the mirror force, F_g – gravitational force, F_{vdW} – the vdW force, N – normal force, and F_s – is the force caused by the plasma sheath.

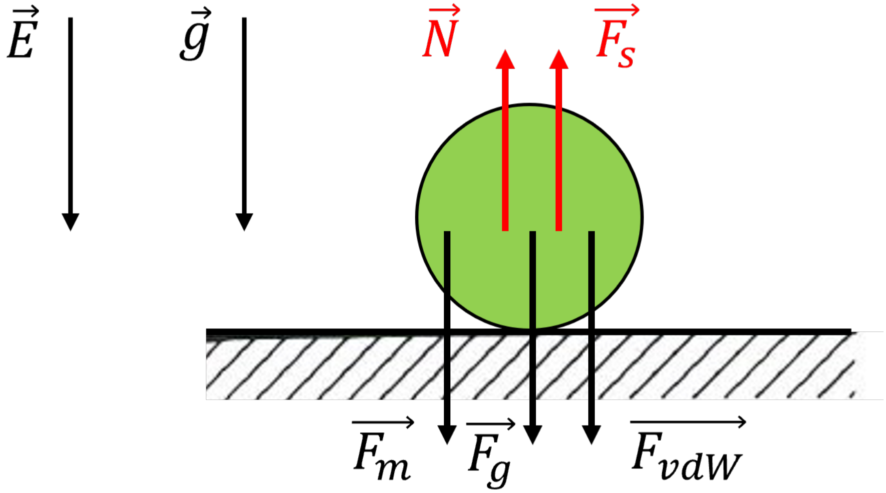

Figure 2.2: The main forces acting on a particle located on a substrate when exposed to plasma. For convenience, all forces adhering particles to the surface are shown in black, while all forces pulling particles into the plasma are shown in red. The capillary force and chemical bonding are not included.

To identify the acting forces, it is essential to assess their magnitude and derive scaling with the size of a particle. As a convention, we will examine the forces acting on a tin (Sn) particle with a size of 1 µm in diameter and density $\rho \cong 7.3$ g/cm^3 [6]. Such particles are relevant for our experiments and typical for metals. The gravitational force then equals $\sim 10^{-14}$ N and is proportional to the particle's volume or $\sim r^3$. Heijmans [5] indicated that the gravitational force is insignificant for particles smaller than 30 µm and can be disregarded. Being in the electric field of a plasma sheath, the particle is subjected to the constant electric force $F_{\text{sheath}} = qE_s$ pulling the particle into the plasma, where q is the particle charge and E_s is the electric field from Equation 2.8.

For ECR plasma ($n_e \sim 10^{16}$ m^{-3}, $T_e = 5$ eV), the electric field $|E_s| \cong 7 \cdot 10^4$ V/m. In the simple spherical capacitor model, the maximal charge carried by a particle with a radius r equals

$$q = C_p \varphi_w = 4\pi\epsilon_0 r \varphi_w \tag{2.9}$$

where ϵ_0 is the free vacuum permittivity, and φ_w is the surface potential from Equation 2.3. Hence, F_{sheath} equals 10^{-10} N and scales linearly with a radius. Another electric force appears between a charged particle and an induced charge (or simply a mirror charge) on a surface that is calculated as

$$F_m = \frac{q^2}{4\pi\epsilon_0 \cdot R^2} \tag{2.10}$$

where R is the constant distance between two charges (for estimation, we assumed $R = r$). Thus the force acting between a charged particle and its mirror charge equals 10^{-7} N and scales as q^2 or r^2 (see Equation 2.9). In practical scenarios, the particle will not attain the maximum charge as predicted by Equation 2.9 due to its interaction with a surface, leading to the potential charge loss through leak currents. The vdW force occurs due to the dipole interaction between molecules of the particle and molecules of the surface. The vdW force can be written as [7]

$$F_{vdW} = A \cdot \frac{H_m}{6d_0^2} r \tag{2.11}$$

where d_0 is the distance with the minimal potential energy in this interaction and is commonly taken as 0.4 nm [7], H_m is the Hamaker constant ($H_m = 10^{-19}$ J for many inorganic materials [8]). It results in a maximum force value of $\sim 10^{-7}$ N. In this model, it is the interaction of a perfectly smooth sphere with a flat surface. The constant A is used here to take into account asperities that are always present on real particles and substrates. The vdW force may be significantly lowered by the correction factor A, which may reduce the vdW force by several orders of magnitude [9]. Practically, the vdW force typically is dominant for particles smaller than 5 µm, while electrostatic forces predominate between 5 µm and 30 µm. Capillary force is calculated as $F_{cap} = 4\pi\gamma \cdot r \cdot cos(\theta)$ and is negligible at low pressures [10], such as in our experiments (5 Pa). Chemical bonding is proportional to U_b/d, where U_b is the bond energy, and d is the distance to the surface. The force was reported to be important for small particles, but negligible for our experiments [1]. The discussed acting forces, their order of magnitude values, and scaling with the particle's radius are listed in descending order in Table 2.1.

The range of particle sizes (diameters) chosen in our work lies between 2 µm and 10 µm which is on the boundary of dominance by vdW and electrostatic forces, and hence, the indication of the dominant force is not trivial. Most of the particles in the selected range are firmly held on the substrate and remain when an electrostatic force from a plasma sheath is applied [5]. However, the effect of hydrogen plasma is not limited to charging. Radicals and ions of hydrogen plasma are highly reactive and often form volatile compounds with the material of the particle, leading to their etching. Also, it is well known that the diffusion of hydrogen plasma components

№	Force	Magnitude (N)	Scaling
1	gravitation	10^{-14} (negligible)	$\sim r^3$
2	plasma sheath	10^{-10}	$\sim r$
3	mirror charge	10^{-8}	$\sim r^2$
4	van der Waals	10^{-7} – 10^{-11}	$\sim r$
5	capillary	negligible	$\sim r$
6	chemical bonds	negligible	-

Table 2.1: The main components of the adhesion force and its scaling with the particle's radius r. Force magnitudes are calculated for a particle of 1 µm in diameter on a surface without an electrical connection.

in some metals is high [11]. Radicals and ions can penetrate under the surface of particles, diffuse into the bulk, and form pressurized bubbles of molecular hydrogen. The rupture of these bubbles can lead to reactive detachment, formation of cracks, and generation of smaller particles. The plasmas in noble gases, such as argon, do not have a chemical interaction component. However, due to a higher ion mass, they have a greater physical sputtering yield. The goal of the experiments in this chapter is to study the influence of hydrogen plasma on the morphology of micrometer-sized particles which affects adhesion.

Table 2.1 suggests two conclusions: 1) The real acting forces in the selected particle size and plasma conditions are: the force from the plasma sheath, the force from the mirror charge, and the vdW force. 2) In simple charging conditions the removal of the plasma sheath is too weak to cause particle detachments.

The tangential force F_{tan} that was mentioned earlier depends on friction with a surface and on applied momentum. The rolling is initiated when a cleaning momentum (tangential) exceeds the adhesion momentum. Experimentally, it was demonstrated that rolling is difficult for small particles [10]. The conclusion of the section is as follows:

1. Rolling is the dominant mechanism when tangential forces create a moment that overcomes the moment created by the adhesion force (and in the act of rolling, the contact area is reduced and release is facilitated; this is the case when particles are subjected to removal forces acting with an angle (f.e. a directed gas jet). Friction typically prevents sliding and thus, rolling is the first motion by tangential forces.

2. The detachment force (normal to the surface) is dominant in plasma. Detachment occurs when it exceeds the adhesion force.

3. Due to adsorbates, charge fluctuation, and the reduced vdW force, removal accidents can happen [12]. Furthermore, the chemical aspect of plasma is not included. In the experimental section, it will be shown that plasma can significantly change the morphology which affects the vdW force and cause particle detachment.

2.3 Experimental methods

The experiments were carried out in three steps. First, non-spherical particles of Sn, Pb, or PbO (yellow) from Sigma-Aldrich with an indicated size distribution of 1–5 µm were mechanically dispersed on a 1 inch sapphire wafer covered with a 100 nm thick Cr coating. Second, the samples were exposed to hydrogen plasma with various doses and constant ion flux and energy. The samples were divided into several groups by their exposure time: from nil (virgin, without being exposed) to 70 h of hydrogen plasma exposure with one wafer exposed at a time (see Table 2.2). Third, cross-sections of the particles were analyzed in a SEM/FIB. It should be noted that air exposure between plasma exposure and analysis was unavoidable in the current experiments, and the particles could be partially oxidized.

2.3.1 ECR plasma setup

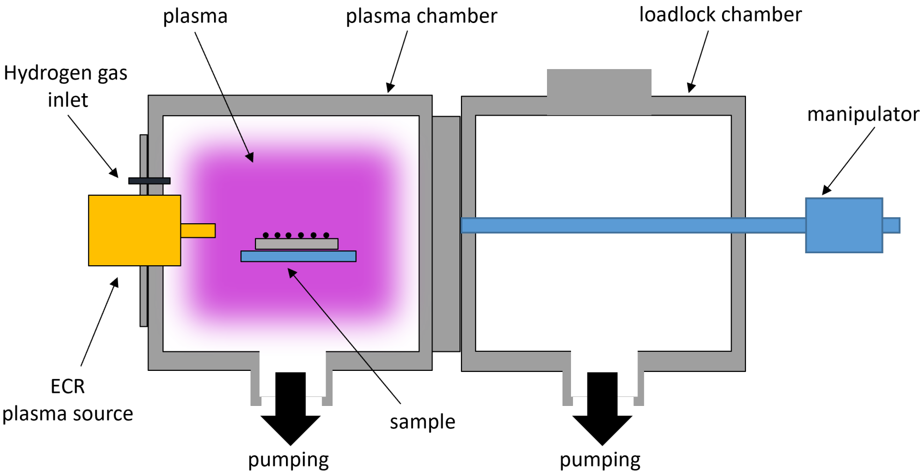

Figure 2.3: Schematic drawing of the experimental setup. The setup comprised the main vessel and the load-lock chamber, separated by a gate valve. The sample with deposited micrometer-sized particles was mounted in the main vessel facing (and 10 cm apart from) the ECR plasma head.

Figure 2.3 shows a schematic overview of the setup used in the experiments. The 3D model of this setup is shown in Figure 2.4. The setup comprised two vacuum vessels (a main vessel for the plasma and a load-lock vessel) separated by a VAT gate valve that remained closed during experiments. The sample faced the plasma head and was located 10 cm apart in the middle of the vessel. The sample holder and the sample were connected to the rest of the vessel and served as ground. The hydrogen plasma was driven by an Electron Cyclotron Resonance (ECR) plasma source Aura-Wave™ from Sairem [13]. Hydrogen was supplied at 20 sccm into the chamber and evacuated by a turbo molecular pump (Pfeiffer THU 200 MP) connected to a scroll dry pre-pump (Edwards XDS10). The pressure inside the chamber was monitored by Philips vacuum gauges (HPT 200 Pirani/Bayard-Alpert and PPT 200 AR, both hydrogen calibrated). Before samples were exposed to the plasma and without hydrogen supply, a base pressure of less than 10^{-4} Pa was obtained. The plasma was maintained at 5 Pa pressure with 100–200 W input RF power at 2.45 GHz by automatically adjusting the resonance frequency mode (tuning mode). During plasma exposures, the sample temperature remained in the range from 20 to approximately 60 °C.

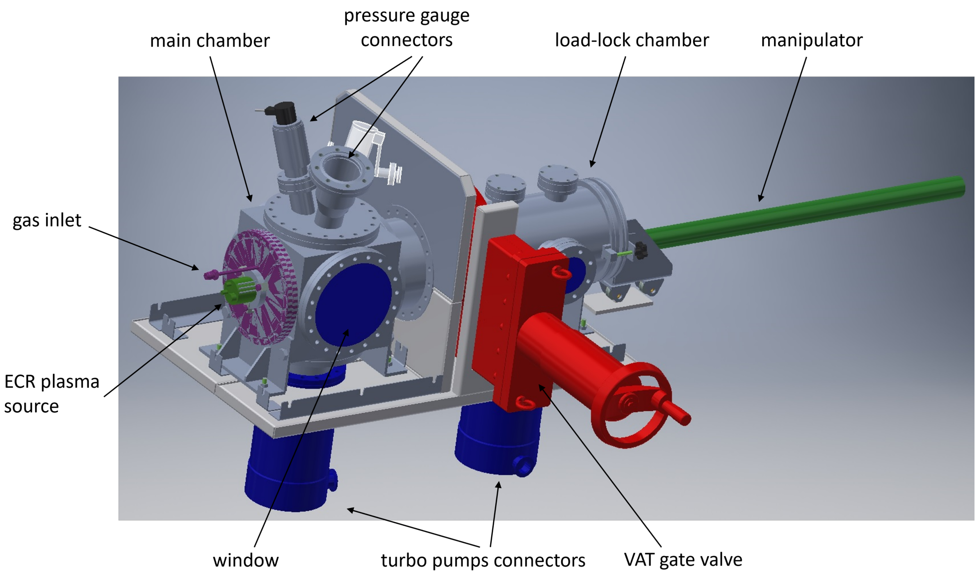

Figure 2.4: 3D model of the experimental setup used for plasma exposures.

The ECR source produces a low-temperature plasma with a smooth distribution of plasma characteristics, e.g. plasma density and electron temperature gradually decay with distance from the source. Values for the electron temperature $T_e \cong$ 5 eV and density $n_e \sim 10^{16}$ m^{-3} were used from Shirai *et al.* [13]. From those parameters, it is estimated that the substrate was exposed to a uniform flux of ions of about I $\sim 10^{15}$ cm^{-2} (1 Am^{-2}) with energies obtained in the plasma sheath of about $E_i = 4 \times T_e$ or 20 eV [14]. The radical flux was 10–100 times higher than the ion flux due to the 10% chance of radical association at stainless steel walls of the main vacuum chamber, compared to $\sim$ 100% chance of H^+ loss by neutralization at the walls [15].

Prior to and post-exposure to hydrogen plasma, the particles were examined in a SEM/FIB. The SEM images comprising the top view of the particles were reported earlier in our previous work [16]. Hereby, we report on the addition of SEM images of the particles' cross-sections produced by an ion beam.

№	Material	Exposure time (RF power)		
1	Sn (Figure 2.9)	virgin	7 h (150 W)	70 h (100 W)
2	Pb (Figure 2.11)	virgin	3 h (200 W)	18 h (100 W)
3	PbO (Figure 2.12)	virgin	3 h (200 W)	18 h (100 W)

Table 2.2: Plasma exposure time and applied power of the samples.

2.3.2 Particle deposition methods

Particle deposition on a substrate plays a crucial role in various scientific and technological fields [17]. Achieving an even distribution of particles is particularly important for studying their adhesion properties and morphology transformation to exclude interaction forces between the particles and clustering. Each particle will be considered isolated. Furthermore, in the context of LLS experiments, the average distance between particles becomes essential to prevent mutual re-irradiation.

In our study, we evaluated several deposition methods to achieve a uniform distribution of particles on the substrate. Mechanical dispersion over a wafer was one such method. This technique is the fastest method but with the lowest distribution quality. Electrostatic deposition was another utilized method, leveraging the attraction between charged particles and oppositely charged surfaces. This approach allowed for precise control over the particle placement and size, resulting in a well-distributed deposition pattern. In another method, we dispersed pills of particles over a wafer using an agitated sonic tip. This technique involved agitating the back side of a wafer using high-frequency vibrations generated by a sonic generator. The resulting dispersion ensured a homogeneous distribution of particles on the substrate.

To assess the quality of the deposition, we employed various characterization techniques. Optical imaging provided a macroscopic view of the particle distribution, allowing for a qualitative evaluation of uniformity and coverage. Additionally, we utilized a SEM coupled with an EDX to obtain detailed information about particle morphology, elemental composition, and their distribution on the substrate. These comprehensive characterization techniques ensured accurate evaluation and validation of the deposition quality.

Mechanical dispersion

One of the simplest deposition methods is the mechanical dispersion over a wafer using a contaminated tweezer/spoon. This method is suitable for relatively large (a few micrometers in diameter) conductive and dry particles that are not clustered by themselves and have weak adhesion to a substrate. After transferring the particles onto a clean wafer, the particles can be rolled to non-occupied spaces by shaking the wafer. Practically, the method worked well only for Pb and PbO particles that have poor adhesion to a substrate. At low concentrations of Pb and PbO, relatively good dispersion can be achieved. A good (or bad) dispersion is defined by the number of clusters and particle deposition density (a higher number of particles is better for enhanced statistics).

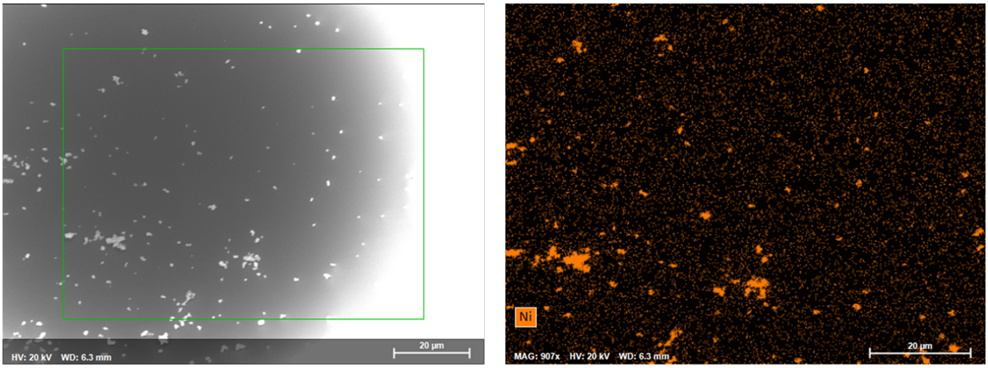

Figure 2.5: SEM images of 2 µm Ni particles deposited by mechanical dispersion (on the left figure). The green rectangle indicates the area of EDX measurements which are depicted on the right figure.

Applying mechanical dispersion to smaller clustered particles may lead to an excessively elevated level of clustering. As an example, Figure 2.5 demonstrates SEM images of mechanically dispersed Ni particles (2 µm, Sigma-Aldrich) over the wafer. The deposition quality was additionally characterized using EDX to ensure the deposited particles were not mixed with ambient contaminants.

Electrostatic deposition

Electrostatic deposition is a well-established method for depositing micrometer-sized particles onto various substrates. The technique utilizes electrostatic force to attract and deposit particles onto a charged substrate. The charged particles are subjected to an electric field, which causes them to move toward the oppositely charged substrate and adhere to its surface. The setup is shown in Figure 2.6.

Electrostatic deposition has many advantages over other deposition methods, including its ability to produce uniform coatings with high precision and accuracy. Additionally, this method can be used to deposit particles of various sizes and shapes onto different types of substrates.

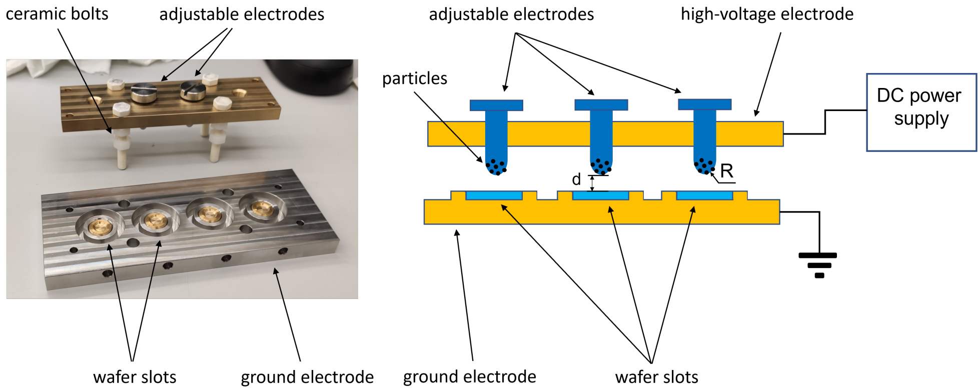

Figure 2.6: The overview of the electrostatic deposition setup. The photo of the electrodes is shown in the figure on the left, the schematic setup is shown on the right. The dusty adjustable electrodes were placed above the clean wafers at a distance d of 0.5–3 mm. The curvature of the electrode's tip R was 2 mm. The applied voltage was used in the range of 1–10 kV.

In another configuration, a flat electrode was used instead of stainless steel bolts. The advantage of flat electrodes lies in the uniform distribution of the electric field, which leads to a more uniform distribution of particles on the clean substrate. In sharp electrode tips, the electric field is concentrated, thereby increasing the range of particles it can detach. For fine powders, the use of sharp electrodes is the only possible way to transfer particles from the tip to the substrate. By experimenting with different electrode shapes, we have selected the appropriate electrode, gap distance, and applied voltage for each powder to optimize the deposition of particles.

Figure 2.7 demonstrates the deposition of Ni particles onto a substrate with Cr coating using the described electrostatic deposition method. Due to the small size of the particles, electrodes with sharp tips, a voltage of 5 kV, and a distance of 1 mm between the electrodes were utilized for the deposition process. Under these conditions, the electric field of the flat capacitor is estimated to be 5 MV/m, which is a lower-bound approximation since the density of the electric field lines is significantly higher at the sharp tip of the power electrode. Assuming a charge on the particle to be $4\epsilon\epsilon_0\pi R$ in the model of an electrostatic spherical capacitor (with $\epsilon = 1$ (vacuum), $\epsilon_0 = 8.85 \times 10^{-12}$ F/m and R = 1 µm), the electric force is calculated to be at least 5.5×10^{-8} N. In the case of a curved electrode, the spatial density of electric field lines significantly increases. Consequently, the actual detachment force may exceed our assessment by several times. This force exceeds most of the vdW forces described in Table 2.1 at the beginning of the chapter, confirming the effectiveness of the method. The method is size-dependent. It means that it is possible to threshold small particles and the final distribution will be narrower. Furthermore, the visual number of clusters did not exceed 10%.

Figure 2.7: The distribution of Ni particles on the wafer using the electrostatic deposition method. The SEM measurements were taken in the middle of the wafer. The deposition method demonstrates the low number of clusters (the distance between particles on average significantly exceeds their size) and high deposition density which enhances statistics. However, the distribution is close to uniform.

Particle deposition using sonic-agitated tip

Another method that demonstrated exceptional efficiency in terms of the balance between ease of use and deposition quality was the dispersion of micro-particles onto the substrate by transferring vibrations from an agitated sonic tip to the backside of the substrate. Using this method, it was effortlessly possible to deposit conducting particles up to 3 µm and with some dexterity down to 1 µm. The Branson Sonifier™ was used as the source of the sonic signals. The variable parameters included the frequency of pulsations, their duration, and amplitude. We utilized a 10% maximum intensity setting and a 10 s total actuation time. The deposition quality achieved using this method was comparable to electrostatic deposition.

An example of sonic deposition can be seen in Figure 2.8 measured by LLS which will be described in detail in Section 3. The distance between the particles is significantly larger compared to their size. The amount of clusters is less than 10% which confirms the effectiveness of this method.

Among the demonstrated deposition methods the most effective was found to be electrostatic deposition because of its size dependency and coaxial symmetry around the projection point of the tip on the wafer. However, it requires more preparation time and several interations of deposition. As sonic deposition demonstrated sufficient quality and short preparation time it was used the most.

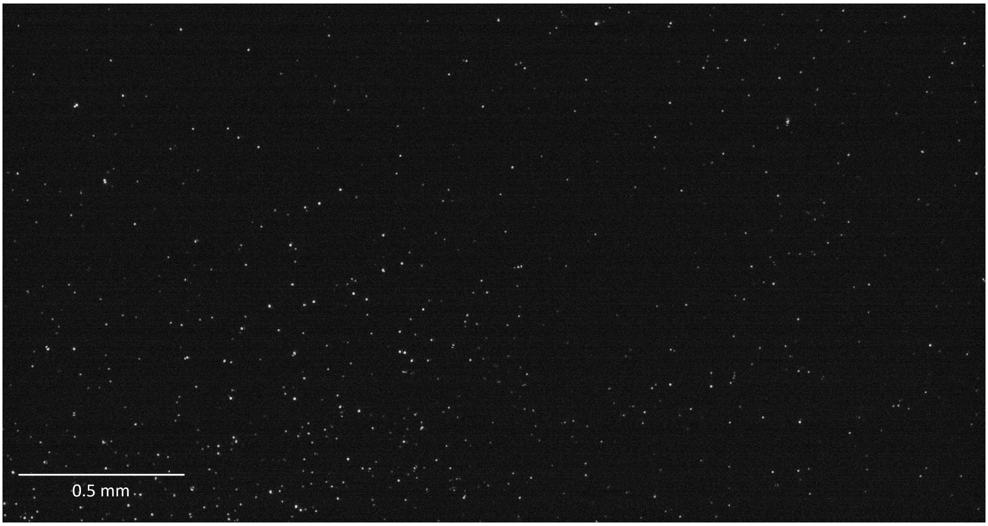

Figure 2.8: The distribution of Pb particles seen in LLS obtained by the sonic deposition method. The deposition method demonstrates the low number of clusters (the distance between particles on average significantly exceeds their size) and high deposition density which enhances statistics. However, the distribution is not uniform.

2.3.3 SEM/FIB measurements

The evaluation of morphology transformations in micrometer-sized particles can be effectively carried out using a SEM/FIB tool (NovaNanolab 600i). SEM plays a crucial role in this analysis as it provides high-resolution imaging, enabling detailed examination of particle surfaces and their structural changes. In addition to SEM, FIB measurements were conducted using a gun that emits gallium (Ga) ions. FIB enables cutting particles and studying the bulk effects.

In order to reduce damage, heating, and sputtering by electron and ion beams, the SEM/FIB parameters were set to minimal values: SEM beam energy was limited to 10 kV and current to 0.4 nA, FIB Ga ion beam energy was limited to 10 kV and current to 0.46 nA. For SEM imaging we used both an in-lens detector and a detector for secondary electrons (SE).

It is worth noting that prolonged exposure of particles to electrons in the SEM environment, which typically operates at around 10^{-3} Pa (10^{-5} mbar), may result in carbon deposition on the surface. This occurs due to the presence of residual gases in the SEM chamber.

2.4 Results

This section is divided into three subsections according to the corresponding type of particles: tin (Sn), lead (Pb), and lead monoxide (PbO). Each section contains the SEM/FIB cross-sections of particles prior to and post-exposure to various doses of plasma. Per subsection, we provide suggestions for the possible damaging mechanism(s). Samples and exposure times are listed in Table 2.2.

2.4.1 Exposure of Tin particles to hydrogen plasma

Tin particles exposed to hydrogen plasma show a significant change with respect to both surface and bulk properties (Figure 2.9). As can be seen from Figure 2.9b and Figure 2.9c, Sn particles under high plasma load develop bubbles in their bulk material and spikes at their surface. The number of these structural changes appears to increase with the exposure time. Interestingly, the bubbles are non-spherical and tend to be shaped along a body-centered tetragonal lattice. The typical size of these plasma-induced structures ranges from a few tens of nanometers to a few tens of micrometers. One explanation for the appearance of these H_2 bubbles is that they build up at interstitial sites in the host lattice and crystal defects, serving as a sink for hydrogen atoms. Hoping between neighboring interstitial sites, hydrogen atoms can diffuse over a big distance from the surface [18].

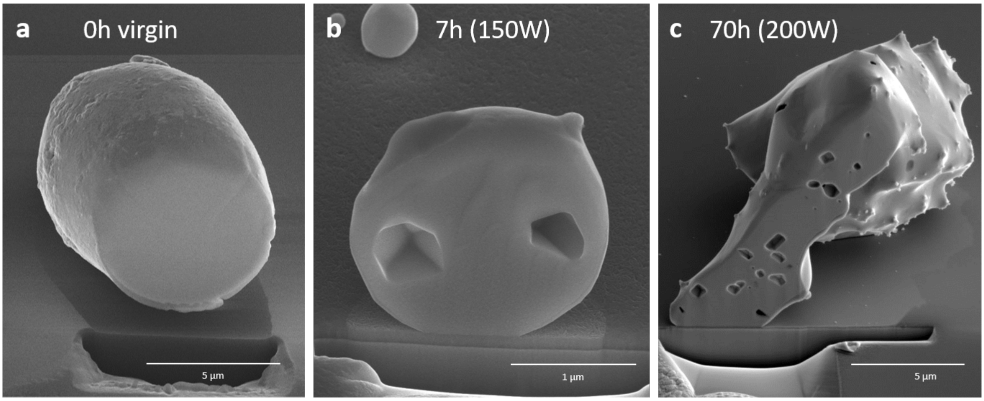

Figure 2.9: SEM images of Sn micrometer-sized particles' cross-sections after exposure to hydrogen plasma. From left to right by exposure time: not exposed (a), 7 h of exposure at 150 W (b), 70 h of exposure at 200 W (c).

Low-energy hydrogen ion implantation is limited only to a few tens of nanometers. Ions are incident normal to the substrate, while bubbles are, obviously, evenly distributed across a Sn particle's volume. This indicates the diffusive nature of the process (while ion implantation may be more relevant in the ITER diverter damaging a wall, and forming a tungsten foam of bursting spherical bubbles), and the significance of the role of hydrogen atom diffusion in a particle. Sn, exposed to a mild hydrogen plasma with a threshold energy of a few tens of electron volts, demonstrated that the growth of the bubble is limited by diffusion of atomic hydrogen in the well-ordered and, probably, crystalline walls. Thus, it corresponds to the tensor nature of a material's tensile strength. The evidence of the tin crystallinity will be demonstrated in the next chapter, based on the measurements of SEM/FIB/TEM data.

Reactions with radicals and ions, relevant for etching are barrier-free reactions. In this case the Gibbs free energy ($\triangle G^\circ$) fully defines the kinetics of the reaction. For a molecule to be unstable, the decomposition reaction's Gibbs energy must be negative and negativity determines the decomposition rate of the molecules.

The bubbles, with trapped hydrogen pressure approaching the Ultimate Tensile Strength (UTS) of Sn, which is 220 MPa [19], grow along the crystalline planes. The explosion or burst of such bubbles may cause the fragmentation or release of the particles from the surface exposed to plasma, and so this effect must be accounted for in applications that are critical with respect to defectivity.

Spikes at the surface in Figure 2.9c likely correspond to the formation/decomposition of stannane (SnH_4) as reported by Tamaru [20]. Stannane is a gas at room temperature [21] for which the formation reaction with hydrogen radicals is endothermic with a standard entropy energy $\triangle S^\circ$ and enthalpy $\triangle H^\circ$ at 298 K being equal to -282 $JK^{-1}mol^{-1}$ and -709.2 $kJmol^{-1}$, respectively (Table 2.3). This yields a total $\triangle G^\circ = -625.2$ $kJmol^{-1}$. The formation of stannane upon the interaction between Sn and hydrogen radicals follows the reaction

$$Sn(s) + 4H(g) \rightarrow SnH_4(g) \tag{2.12}$$

where s and g indicate the surface and gas phase respectively. The reaction with molecular hydrogen is exothermic and, thus, less likely.

According to our calculations, the decomposition of stannane on catalytically active surface proceeds spontaneously with the corresponding Gibbs free energy of $\triangle G^\circ =$ -187.8 $kJmol^{-1}$ (which is close to those, reported by Ugur *et al.* [22]). Using X-ray Photoelectron Spectroscopy (XPS) the authors confirmed the decomposition of stannane on a metal surface into pure metallic Sn by

$$SnH_4 \rightarrow Sn + 2H_2 \tag{2.13}$$

In this respect, Ugur *et al.* suggested a possible mechanism for the decomposition of SnH_4 under various hydrogen fluxes (ranging from 5.4×10^{16} to 3.2×10^{17} $cm^{-2}s^{-1}$). The author contended that for low radical flux ($\sim 5 \times 10^{16}$ $cm^{-2}s^{-1}$) the majority of atoms will likely recombine on the surface into H_2 molecules with only a few of them interacting with Sn as was suggested in a similar study on Ru and resulting in the low etching rate [23]. At higher flux $\sim 3 \times 10^{17}$ $cm^{-2}s^{-1}$, corresponding to conditions similar to our experiments ($\sim 10^{17}$ $cm^{-2}s^{-1}$), the efficiency of the reaction of impinging radicals with Sn is growing as more H_2 molecules desorb and more Sn spots on the surface are available. This means the suggested mechanism of surface mass transfer is reliable.

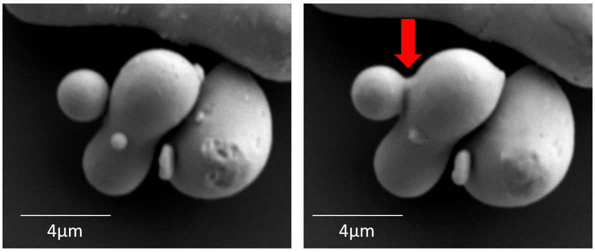

Figure 2.10: SEM images of Sn particles particle before (on the left) and after 1.5 h of exposure to hydrogen plasma at 100 W (on the right), during exposure Sn remained below the melting point. The arrow indicates the emerging bridge between the particles, confirming Sn transfer along the particle's surface.

The catalytic activity of tin's surface for stannane seems to be higher compared to the wafer's surface coated with native oxide Cr_2O_3. Figure 2.10 shows the surface migration of Sn atoms between two physically connected particles, forming a bridge. The effect was achieved already after 1.5 h of exposure to the plasma. We didn't observe such effects on the particles, separated by a gap in the wafer surface. Furthermore, the original particle was rough as can be seen in Figure 2.9a. The exposed Sn particle in Figure 2.9c is smoother except for individual spikes, which also supports our hypothesis of Sn transport along the particle surface in a cycle of formation and decomposition of stannane. In addition, for some Sn particles after exposure, we also observed the increased contact spot area to the Cr-coated wafer (Figure 2.9b and Figure 2.9c), which is unexpected for pristine aspherical particles. With this, we can conclude that plasma-induced surface Sn transfer contributes to the growing adhesion force over time of exposure. This is in contrast to the commonly reported effect of reducing the vdW force.

2.4.2 Exposure of Lead particles to hydrogen plasma

Similarly to tin, the formation of a lead hydride is very likely. Plumbane (PbH_4) was reported by many authors as a very unstable hydride and it lacks accurate measurements [24, 25]. In Table 2.3 we assessed plumbane's formation and decomposition $\triangle G^\circ$ by extrapolating the enthalpies $\triangle H^\circ$ of the similar reactions with C, Si, and Sn. Indeed, plotting enthalpies of the hydride formation/decomposition of the reactions listed in Table 2.3 versus their bond energies C–H, Si–H, Sn–H and Pb–H (337 kJ/mol, 300 kJ/mol, 267 kJ/mol and 176 kJ/mol respectively) [26], the formation and decomposition enthalpies of plumbane can be assessed to -405 kJ/mol and -460 kJ/mol respectively. As can be seen, the entropies of the reaction are nearly equal. Assuming the same entropy for plumbane reactions as for stannane (-282 J/mol and 84 J/mol respectively), the Gibbs free energy was also assessed.

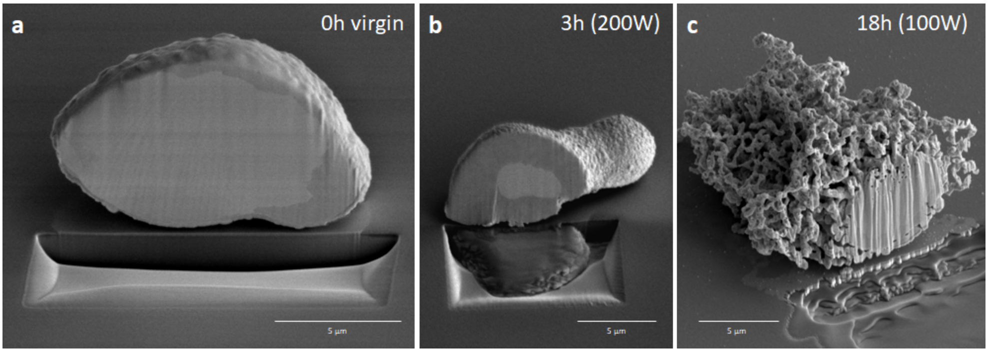

Figure 2.11: SEM images of Pb micrometer-sized particles' cross-sections after exposure to hydrogen plasma. From left to right by exposure time: not exposed (a), 3 h of exposure at 200 W (b), 18h of exposure at 100 W (c).

Plumbane, being formed in the reaction

$$Pb(s) + 4H(g) \rightarrow PbH_4(g) \tag{2.14}$$

is much less stable compared to the stannane molecule [27], confirmed by the strong negativity of the assessed $\triangle G^{\circ}$ reaction. Thus, the plumbane is likely to decompose on the surface before having a chance to leave it, and the redeposition of Pb is even more likely than the redeposition of Sn (Figure 2.11). Though, the assessed $\triangle G^{\circ}$ of stannane production is more negative compared to plumbane (which translates into the higher etching speed for Sn), from Figure 2.11 we can conclude that Pb's morphology changes faster than Sn's. Therefore, the dominant mechanism for Pb morphology evolution is the formation of bubbles. The bubbles inflate and rupture near the surface (Figure 2.11c), which explains the "etching" effect.

The different phases within the Pb particles' cross-sections can be associated with the Pb's response to the electron beam. The pristine particle (Figure 2.11a) may have a native oxide shell with a different density which seems darker in the SEM images. The hydrogen-exposed particles (see Figure 2.11b and Figure 2.11c) appear to have a hydrogen-rich zone which appears as a dark area, whereas the pristine (hydrogen-free) Pb area appears brighter.

2.4.3 Exposure of Lead (II) oxide particles to hydrogen plasma

Lead (II) oxide particles demonstrate even the fastest change when exposed to hydrogen plasma compared to the Sn and Pb particles (see Figure 2.12).

Note that the retrieving of oxygen, occurring in the reaction

$$PbO + 2H \rightarrow Pb + H_2O \tag{2.15}$$

is a more likely process than plumbane formation, since fewer reactants are needed to form it and since the water formation Gibbs free energy (-237.1 according to Dean [28]) is more negative than, for instance, plumbane formation $\triangle G^\circ$. Thus, the dominant process in PbO particles is etching and it is likely to proceed via PbO → (partial oxide) → Pb → PbH_4. The low-density partial oxide will yield a low-density Pb that in turn is easier to etch or blister due to the abundance of active sites.

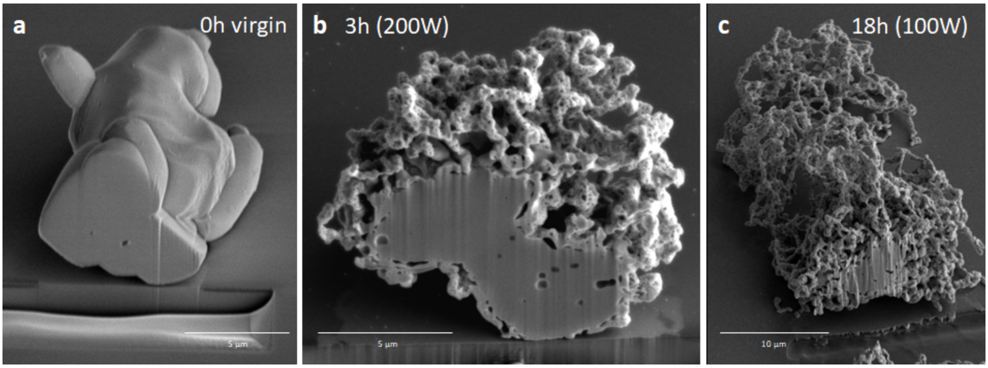

Figure 2.12: SEM images of PbO micrometer-sized particles' cross-sections after exposure to hydrogen plasma. From left to right by exposure time: not exposed (a), 3 h of exposure at 200 W (b), 18 h of exposure at 100 W (c).

2.5 Discussion

We can classify various cases of hydrogen interaction with the particles based on the observations. The particle may be subjected to three independent mechanisms: etching, bubble formation, and physical sputtering. Some properties of the materials must be considered when evaluating the dominant mechanism: formation/decomposition rate of the hydrides (if present), diffusion properties of hydrogen atoms in the particle, and the material's UTS. The diffusion of radicals was studied only in C and Si. There is a lack of information about diffusion in Sn, Pb, and PbO.

2.5.1 Etching and surface mass transfer

The ability of some materials to form volatile hydrides determines the possibility of etching those materials in hydrogen plasma, and consequently the chance of material transfer in the cycle of formation and decomposition of hydrides. The stability of volatile hydrides decreases moving from C to Pb within the 4th group of the periodic table along with the formation of the Gibbs free energy (Table 2.3). It is likely that hydrides from C to Si are so stable that redeposition and material transfer are insignificant. Sn hydride is intermediate in its stability, so the material transfer is noticeable. Pb hydride is so unstable that material transfer is likely happening on a small scale, possibly smaller than the particle itself. Pb is not on the list, as plumbane may even decompose before it diffuses far from the surface. However, PbO is etchable, because of oxygen extraction by the plasma. As an example, dry etching of Si in hydrogen and halogen-containing plasmas was widely studied [29]. The etching of C by hydrogen plasma was assessed by Park to 0.1 nm/min at room temperature [30]. Carbon etching in EUV-induced plasma was calculated by both Astakhov and van Leuken, resulting in an etch rate of about 0.3 nm/min [31, 32]. The etching of amorphous Si by hydrogen plasma is of an order of 1 nm/min [33]. The etching of Sn by hydrogen radicals in EUV-induced plasma applications was studied by van Herpen *et al.* [34], resulting in etch rates of about 50 nm/min on a Si substrate and 28 nm/min on a Ru substrate. The etching of Sn particles by hydrogen plasma was described by Elg *et al.* [35] with etch rates at room temperature of about 1-10 nm/min for typical Capacitively Coupled Plasma (CCP) or typical conditions for hydrogen radical generators [36]. There is no literature data regarding Pb etching by hydrogen plasma.

Surface migration of Sn atoms by formation and decomposition of stannane is significant for both: the particle's shape and region of contact (translated into the particle's adhesion force). The exposed Sn particle presented the increased plane-to-plane contact area, which is unexpected as typically plasma is known to suppress the vdW force by inducing nanoasphericities. For contamination control, it might be relevant to investigate which of the processes wins: the emerging spikes increasing the particle/substrate separation and promoting the release or the increasing sticking coefficient, preventing the particle from release. The mechanism of surface migration seems to be important for materials with unstable volatile hydrides. As a result, such an effect wasn't reported for Si, i.e. the silane molecule is stable and does not decompose near the particle. However, in our experiments, we didn't observe the increased contact spot for Pb particles that could confirm the trend, presumably due to the dominant bubbles rupturing near the surface.

Due to a lack of reliable information regarding the etching of lead and lead oxides by hydrogen plasma, we will refer to our experiments and a previous publication [16]. As was demonstrated before, PbO has a higher tendency toward etching (Figure 2.12) because of the production of water. Etching-induced asperities or stress-induced dislocations in subsurface layers may impede the diffusion of atomic hydrogen deeper into the bulk by trapping it and thus promote bubbles near the surface and suppress bubbles in the bulk.

2.5.2 Bubble inflation/particle fragmentation

Trapping of molecular hydrogen under the particle's surface in bubbles and subsequent particle fragmentation may occur even if the incident energy of ions is too low to create a physical displacement. The atomic or ionic hydrogen from the plasma adsorbs on a surface or near the surface (some nanometers after implantation), diffuses into the bulk, and precipitates on low-energy sites such as cavities and vacancy clusters or dislocations. The recombination of hydrogen atoms to H_2 in such cavities or at such vacancy sites leads to the accumulation of H_2 gas at increasing pressure and deformation. This eventually leads to the formation of blisters (f.i., Figure 2.9c).

Growing blisters are associated with stress, centered on the blister (see Figure 2.13, the enlarged scheme) which exponentially relaxes toward the surface of the particle.

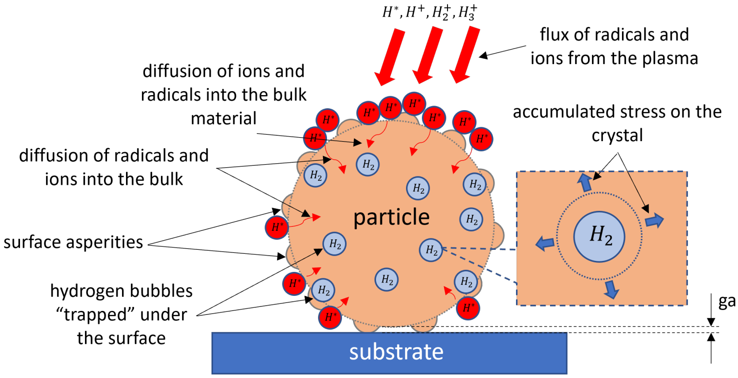

Figure 2.13: An illustration of a particle exposed to hydrogen plasma and a schematic displaying the propagation of atomic hydrogen within the crystal, i.e. the diffusion of hydrogen radicals to low-energy sites such as cavities or crystal defects. The pointed spots promote the formation of molecular hydrogen leading to an increased hydrogen pressure locally.

As shown in Figure 2.13, blister growth depends on the relative rates of hydrogen supply by the diffusion process to and escape from the cavity and on the equilibrium between molecular and atomic hydrogen densities locally [37, 38]. If outgassing exceeds the supply of hydrogen, the blister will collapse.

The rate of hydrogen supply to the cavity depends on bulk diffusion properties and on the occupancy of sites on the surface. The dissolved hydrogen atoms energetically tend to accumulate into bubbles on vacancy defects and near dislocations. The distribution of bubbles is determined not only by the diffusion length of hydrogen atoms but also by screening effects of defects and existent bubbles. For instance, the higher diffusion coefficient for Pb compared to Sn is compensated by a larger number of dislocations (the number of dislocations is inversely proportional to the material’s UTS [39]), so in Pb (and in partial lead oxide) bubbles are concentrated in the layer at a fraction of a micrometer from the particle surface. In Sn, as expected, the bubbles are distributed evenly in bulk, which indicates that diffusion spreads atomic hydrogen concentration only after precipitation takes place.

In order to form a blister or even a bubble, some conditions must be fulfilled. First, materials with a high enthalpy of the solution $\triangle$H and, as a consequence, with a high concentration of dissolved hydrogen (when subjected to hydrogen plasma) are naturally prone to bubble formation [18]. Alternatively, if hydrogen dissolution is a barrier reaction, ion implantation should promote saturation of the bulk. Second, the diffusion of radicals must be sufficient to supply atomic hydrogen to the emerging bubble faster than outgassing tries to deflate it. Hydrogen radicals, as discussed before, diffuse in metals by hopping between interstitial sites. It was found that the dense packing of the Si structure enabled hydrogen incorporation depth of only about 10 nm

Reaction	$\triangle G^{\circ}$ kJmol^{-1}	$\triangle H^{\circ}$ kJmol^{-1}	$\triangle S^{\circ}$ JK^{-1}mol^{-1}	Ref
$C + 4H \rightarrow CH_4$	-864.7	-946.9	-276	21, 40
$CH_4 \rightarrow C + 2H_2$	50.7	74.9	81	21, 40
$Si + 4H \rightarrow SiH_4$	-757.0	-837.5	-270	21, 40
$SiH_4 \rightarrow Si + 2H_2$	-46.2	-34.3	40	21, 40
$Sn + 4H \rightarrow SnH_4$	-625.9	-709.2	-282	21
$Sn + 2H_2 \rightarrow SnH_4$	187.8	162.8	-84	21
$SnH_4 \rightarrow Sn + 2H_2$	-187.8	-162.8	84	21, 22
$Pb + 4H \rightarrow PbH_4$	-321.0	-405.0	-282	assessed
$PbH_4 \rightarrow Pb + 2H_2$	-485.0	-460.0	84	assessed
$PbO + 2H \rightarrow Pb + H_2O$	-455.0	-503.7	-160	21, 41

Table 2.3: The Gibbs free energy, entropy, and enthalpy of the formed and decomposed volatile hydrides given at 298 K. The data for materials interacting with hydrogen is given for solid bodies. Formation and decomposition of plumbane (PbH_4) were empirically assessed based on the stannane (SnH_4) data.

under incident energies of 300 eV, and once implanted, atomic hydrogen stayed in place. That means that the formation of blisters in Si is excluded and etching is dominant. Third, the mechanical properties of the particle must be taken into account. The pressure inside of the growing bubble exceeds UTS, so materials with low UTS are also prone to bubble formation.

Condon proposed three basic criteria to conclude if the blisters appear to qualify for growth [42]. The first criterion is the supersaturation of dissolved hydrogen. The remaining criteria depend on the level of hydrogen supersaturation. In cases where the saturation is under a certain threshold, the additional criterion of vacancy supersaturation is needed. To make this mechanism possible, the concentration of metal vacancies must be greater than expected for the equilibrium state. This may happen in the presence of impurities or crystal defects. The upper limit of supersaturation determines whether the process goes to the formation of cavities or to the formation of hydrides. This criterion states that the supersaturation level must remain below the concentration for hydride formation. The supersaturation effect was also observed by Ou *et al.* [43], as well as the research of Kamada [44].

Xie *et al.* [45] showed that, in general, the growth of a blister near the surface begins with the appearance of a nanoscale gas bubble (with a certain radius of curvature

R), promoted by the internal gas pressure P, which plastically deforms the covering layer that becomes visible on a particle's surface in SEM. Based on their review for hydrogen blistering in Al, the pressure P within this blister with saturated hydrogen must exceed the yield strength σ_Y of the material in the covering layer and its surface energy γ. The critical blister radius R_C before explosion depends on P with the following relationship [45]:

$$P - \frac{4\sigma_Y t^2}{3{R_C}^2} - \frac{2\gamma}{R_C} > 0 \tag{2.16}$$

where t denotes the thickness of the capping layer. Using the values (220 MPa, 0.5×10^{-6} m, 0.5×10^{-6} m, 10^{-9} Jm^{-2}) for the given parameters (σ_Y, R_C, t, and γ) respectively, which are typical in these experiments, the pressure within the bubble reaches of about 290 MPa that exceed the material's yield strength and therefore corresponds with the observations.

2.5.3 Physical sputtering damage

The maximum momentum transfer in a collision between the heaviest hydrogen-ion (H_3^+) in the ECR hydrogen plasma used in this work and the lightest target element (Sn) with a bond energy of about 3 eV is limited to 10% with a total threshold for ions of around 25 eV. Therefore, the effect of physical sputtering by hydrogen ions can be neglected [38].

One should note here that, probably, all the damaging processes listed above might act on each of the chosen materials collectively. However, the bulk properties dictate which mechanism is dominant. The relative sensitivities of Pb and PbO particles to hydrogen plasma compared to that of Sn particles is reflected in the decreasing stability of their hydrides moving down in the periodic table (from C to Pb). As discussed in this section, the increasing stability of hydrides at hydrogen supersaturation conditions decreases blister formation and promotes chemical etching. Furthermore, the low yield strength of 16–17 MPa [46] for Pb and PbO compared to 220 MPa for Sn particles means a much lower pressure inside the bubbles is required to enable bubble inflation in these low yield strength materials. However, the bubbles are barely formed deep in the bulk of Pb and PbO particles as atomic hydrogen precipitates on the abundant dislocations and lattice defects, more concentrated in Pb and PbO (partially reduced, stressed) compared to Sn.

2.6 Conclusion

Tin, lead, and lead (II) oxide particles exposed to hydrogen plasma were investigated using SEM in combination with FIB. The core objective of this study is the elucidation of the plasma interaction with the selected particles.

With the obtained results we confirm that reactive materials (subjected to etching or trapping of molecular hydrogen under the surface) in hydrogen or EUV-induced plasmas may impact the adhesion. The adhesion alteration is associated with two mechanisms. In the first mechanism, the surface mass transfer leads to the morphology change and increased contact area between the particle and the substrate. The second mechanism is the rupture of blisters that is associated with particle fragmentation.

We discussed the difference between bubbles formed by the physical implantation of ions (fusion plasma) and bubbles formed by diffusion mechanisms acting in Pb and Sn. Bubbles in a tungsten wall have a round shape, but no crystalline planes, because of implantation-induced damage of the lattice. Contrary to that, the bubbles, followed by diffusive mechanisms (Pb and Sn) are limited by diffusion of atomic hydrogen. Bubbles in Pb in our study were similar to fusion plasma, while the bubbles in Sn demonstrated sharp crystalline edges and a tensor nature of the material's tensile strength.

In order to use hydrogen plasma as a tool for selective etching we advise avoiding the materials with a high coefficient of atomic hydrogen diffusion due to the bubbling inflation in the bulk and their possible subsequent rupture.

2.7 Bibliography

[1] Marcus Adrianus van de Kerkhof. *EUV-induced Plasma, Electrostatics and Particle Contamination Control.* PhD thesis, Applied Physics and Science Education, August 2021. Proefschrift.

[2] Appendix a: Collision dynamics. In *Principles of Plasma Discharges and Materials Processing*, pages 723–726. John Wiley & Sons, Inc., Hoboken, NJ, USA, January 2005.

[3] T.H.M. van de Ven. *Ion fluxes towards surfaces exposed to EUV-induced plasmas.* PhD thesis, Applied Physics and Science Education, July 2018. Proefschrift.

[4] Anatolii D. Zimon. Fundamental concepts of particle adhesion. In *Adhesion of Dust and Powder*, pages 1–30. Springer US, 1982.

[5] L. Heijmans and Sander Nijdam. Dust on a surface in a plasma: A charge simulation. *Physics of Plasmas*, 23:043703, 04 2016.

[6] https://webbook.nist.gov/cgi/cbook.cgi?ID=7440-31-5.

[7] H. Krupp. Particle adhesion theory and experiment. *Advances in Colloid and Interface Science*, 1(2):111–239, May 1967.

[8] Lennart Bergström. Hamaker constants of inorganic materials. *Advances in Colloid and Interface Science*, 70:125–169, July 1997.

[9] Jacob N Israelachvili. Historical perspective. In *Intermolecular and Surface Forces*, pages 3–22. Elsevier, 2011.

[10] N.A. Lammers. *Laser-induced shock wave cleaning of EUV photomasks.* PhD thesis, Applied Physics and Science Education, 2012.

[11] J. Volkl and G. Alefeld. Diffusion of hydrogen in metals. In *Topics in Applied Physics*, pages 321–348. Springer Berlin Heidelberg, 1978.

[12] Mark van de Kerkhof, Andrei M. Yakunin, Vladimir Kvon, Andrey Nikipelov, Dmitry Astakhov, Pavel Krainov, and Vadim Banine. EUV-induced hydrogen plasma and particle release. *Radiation Effects and Defects in Solids*, 177(5-6):486–512, mar 2022.

[13] Kouun Shirai, Takashi Iizuka, and Shun ichi Gonda. Electric probe measurements in an ECR plasma CVD apparatus. *Japanese Journal of Applied Physics*, 28(Part 1, No. 5):897–902, may 1989.

[14] T. H. M. van de Ven, P. Reefman, C. A. de Meijere, R. M. van der Horst, M. van Kampen, V. Y. Banine, and J. Beckers. Ion energy distributions in highly transient EUV induced plasma in hydrogen. *Journal of Applied Physics*, 123(6):063301, February 2018.

[15] Miran Mozetič, Matija Drobnič, and Anton Zalar. Recombination of neutral hydrogen atoms on AISI 304 stainless steel surface. *Applied Surface Science*, 144-145:399–403, April 1999.

[16] Dmitry Shefer, Andrey Nikipelov, Mark van de Kerkhof, Vadim Banine, and Job Beckers. Morphology change and release of tin and lead micro-particles from substrates in hydrogen plasma. In Nelson M. Felix and Anna Lio, editors, *Extreme Ultraviolet (EUV) Lithography XII*, volume 11609, pages 116 – 123. International Society for Optics and Photonics, SPIE, 2021.

[17] Jaehong Park, Jimin Jeong, Chul Kim, and Jungho Hwang. Deposition of charged aerosol particles on a substrate by collimating through an electric field assisted coaxial flow nozzle. *Aerosol Science and Technology*, 47(5):512–519, May 2013.

[18] R. Kirchheim and A. Pundt. Hydrogen in metals. In *Physical Metallurgy*, page 25972705. Elsevier, 2014.

[19] G. W. C. Kaye. *Tables of physical and chemical constants and some mathematical functions.* Longman, London New York, 1986.

[20] Kenzi Tamaru. The thermal decomposition of tin hydride. *The Journal of Physical Chemistry*, 60(5):610–612, May 1956.

[21] OECD and Nuclear Energy Agency. *Chemical Thermodynamics of Tin, Volume 12.* OECD, 2012.

[22] D. Ugur, A. Storm, Rogier Verberk, J.C. Brouwer, and Wim G. Sloof. Decomposition of snh4 molecules on metal and metal-oxide surfaces. *Applied Surface Science*, 288:673–676, 01 2014.

[23] Nadir Faradzhev and Vadim Sidorkin. Hydrogen mediated transport of sn to ru film surface. *Journal of Vacuum Science & Technology A: Vacuum, Surfaces, and Films*, 27(2):306–314, March 2009.

[24] Patryk Zaleski-Ejgierd, Roald Hoffmann, and N. W. Ashcroft. High pressure stabilization and emergent forms of pbh4. *Physical Review Letters*, 107(3), July 2011.

[25] Thomas A. Hein, Walter Thiel, and Timothy J. Lee. Ab initio study of the stability and vibrational spectra of plumbane, methylplumbane, and homologous compounds. *The Journal of Physical Chemistry*, 97(17):4381–4385, Apr 1993.

[26] E. Lippert. The strengths of chemical bonds, von t. l. cottrell. butterworths publications ltd., london 1958. 2. aufl., x, 317 s., geb.t—/32/—. *Angewandte Chemie*, 72(16):602–602, August 1960.

[27] Xuefeng Wang and Lester Andrews. Infrared spectra of group 14 hydrides in solid hydrogen: Experimental observation of pbh4, pb2h2, and pb2h4. *Journal of the American Chemical Society*, 125(21):6581–6587, May 2003.

[28] J.A. Dean and N.A. Lange. *Lange's Handbook of Chemistry*. Number v. 15 in Lange's Handbook of Chemistry. McGraw-Hill, 1999.

[29] Tomokazu Ohchi, Shoji Kobayashi, Masanaga Fukasawa, Katsuhisa Kugimiya, Takashi Kinoshita, Toshifumi Takizawa, Satoshi Hamaguchi, Yukihiro Kamide, and Tetsuya Tatsumi. Reducing damage to si substrates during gate etching processes. *Japanese Journal of Applied Physics*, 47(7):5324–5326, jul 2008.

[30] S. Park and R.M. Walser. Hydrogen plasma etching of pyromeric carbon films. *Carbon*, 23(6):701–706, 1985.

[31] D. I. Astakhov, W. J. Goedheer, C. J. Lee, V. V. Ivanov, V. M. Krivtsun, O. Yakushev, K. N. Koshelev, D. V. Lopaev, and F. Bijkerk. Numerical and experimental studies of the carbon etching in euv-induced plasma, 2015.

[32] D. P. J. van Leuken, C. A. de Meijere, R. van der Horst, V. Y. Banine, E. A. Osorio, and J. Beckers. An atomic hydrogen etching sensor for h2 plasma diagnostics. *Review of Scientific Instruments*, 92(6):063518, June 2021.

[33] Aomar Hadjadj, Fadila Larbi, Mickaël Gilliot, and Pere Cabarrocas. Etching of a-si:h thin films by hydrogen plasma: A view from in situ spectroscopic ellipsometry. *The Journal of chemical physics*, 141:084708, 08 2014.

[34] Maarten Van Herpen, D.J.W. Klunder, W. Soer, R. Moors, and V. Banine. Sn etching with hydrogen radicals to clean euv optics. *Chemical Physics Letters - CHEM PHYS LETT*, 484:197–199, 01 2010.

[35] Daniel Elg, Gianluca Panici, Jason Peck, Shailendra Srivastava, and David Ruzic. Modeling and measurement of hydrogen radical densities of in situ plasma-based sn cleaning source. *Journal of Micro/Nanolithography, MEMS, and MOEMS*, 16:023–501, 04 2017.

[36] Dren Qerimi, Gianluca Panici, Arihant Jain, Daniel Jacobson, and David N. Ruzic. Study of a linear surface wave plasma source for tin removal in an extreme ultraviolet source. *Journal of Vacuum Science & Technology B*, 38(5):052601, September 2020.

[37] A S Kuznetsov, M A Gleeson, and F Bijkerk. Temperature dependencies of hydrogen-induced blistering of thin film multilayers. *J. Appl. Phys.*, 115(17):173510, May 2014.

[38] Mark A. van de Kerkhof, Ernst Galutschek, Andrei Yakunin, Selwyn Cats, and Christian Cloin. Particulate and molecular contamination control in EUV-induced h2-plasma in EUV lithographic scanner. In Carlos E. Soares, Eve M. Wooldridge, and Bruce A. Matheson, editors, *Systems Contamination: Prediction, Control, and Performance 2020*. SPIE, August 2020.

[39] Brian Lawn. *Fracture of Brittle Solids*. Cambridge University Press, June 1993.

[40] M Chase. *NIST-JANAF Thermochemical Tables, 4th Edition.* American Institute of Physics, -1, 1998-08-01 1998.

[41] D. Risold, J. Nagata, and Ryosuke Suzuki. Thermodynamics of the pb-o system. *Journal of Phase Equilibria*, 19:213–233, 06 1998.

[42] J.B. Condon and T. Schober. Hydrogen bubbles in metals. *Journal of Nuclear Materials*, 207:1–24, 1993.

[43] W. Ou, R.S. Al, J.W.M. Vernimmen, S. Brons, P. Rindt, and T.W. Morgan. Deuterium retention in sn-filled samples exposed to fusion-relevant flux plasmas. *Nuclear Fusion*, 60(2):026008, jan 2020.

[44] Kohji Kamada. Hydrogen implantation effects in the subsurface layer of aluminum -bubble pressure and surface modifications. *Journal of Nuclear Materials*, 169:141–150, December 1989.

[45] De-Gang Xie, Zhang-Jie Wang, Jun Sun, Ju Li, Evan Ma, and Zhi-Wei Shan. In situ study of the initiation of hydrogen bubbles at the aluminium metal/oxide interface. *Nature Materials*, 14(9):899–903, June 2015.

[46] Colin J Smithells. *Smithells metals reference book.* Butterworth-Heinemann, Woburn, MA, 8 edition, May 2014.

Chapter 3

Laser light Scattering to monitor the morphology of macrometer-sized particles in hydrogen plasma

Preface. Laser Light Scattering (LLS) measurements, combined with a long-distance microscope, were utilized to detect micrometer-sized particles on a flat metal substrate. In-situ monitoring of hundreds of particles was carried out to investigate the effect of plasma exposure on particle adhesion, morphology, and composition. The morphology change in plasma leads to particle fragmentation, blistering, and other processes that may cause the detachment of particles and produce unwanted defectivity in a lithographic tool. Calibration of the LLS method was conducted on the monodisperse melamine resin spheres with known sizes. This calibration demonstrated a lowest achievable noise level of approximately 3% for counting particles 5.26 µm in diameter. For collections of non-monodisperse particles, their size distribution was obtained by converting the effective scattering cross-section of individual particles to the dimension of a sphere using the Mie theory. We examined the effect of low-temperature plasma using in-situ LLS and an ex-situ Scanning Electron Microscope (SEM) on the detachment of micrometer-sized particles made of various materials, including Si, Sn, Pb, PbO, Ni, Zn, CeO, and stainless steel because of their relevance in industrial applications. The shape transformation was confirmed by correlated SEM/FIB and LLS measurements, revealing the emergence of asperities, enhanced surface smoothness, surface diffusion, and the precipitation of pressurized bubbles within the bulk material. The discussed hypotheses for morphology changes during exposure to plasma can be used in applications.

The results of this chapter were partially published as D. Shefer, A. Nikipelov, M. van de Kerkhof, V. Banine, and J. Beckers, *Laser light scattering (LLS) to observe plasma impact on the adhesion of micrometer-sized particles to a surface*, Journal of Physics D: Applied Physics, vol. 56, n. 45, August 2023. DOI: 10.1088/1361-6463/aceb02

3.1 Introduction

In the semiconductor industry, Laser Light Scattering (LLS) is a widely used surface inspection method for defects in addition to SEM and AFM inspection [1, 2]. The method follows the light scattering at different angles from a relatively small spot [3] (typically, 10 µm). Particles bigger than the wavelength scatter most of the light in the forward direction. Hence, a reflective substrate is a convenient method to improve such particle visibility. A substantial change in particle morphology affects the forward-scattered light intensity, which can be used as a diagnostic method. In this chapter, we apply the LLS method combined with long-distance microscopy to image micrometer-sized particles. It will be demonstrated that the LLS method can be adapted for the in-situ observation of micrometer-sized particles on a surface placed in plasma or other stressed conditions such as removal flow caused by a gas jet. The scattered light was collected from particles on the surface of several square millimeters which enabled following hundreds and thousands of particles for better statistics. In addition, the Mie theory was applied to determine the size distribution of the particles. The results are compared to traditional SEM accompanied by FIB inspection to demonstrate the impact of hydrogen plasma on the surface of particles and in their bulk.

The advantage of LLS over traditional SEM measurement is the noninvasive in-situ manner of measuring, which directly shows the impact of plasma treatment on particles during exposure, high speed, and sensitivity to particle optical properties. The disadvantage of LLS, as adopted in the semiconductor industry, is the need for a high numerical aperture (NA) to enhance resolution and light collection efficiency, which means that the method is used only in ex-situ types of inspections.

This chapter is divided into eight main sections:

1. Introduction (Section 3.1) provides the motivation and the general introduction to the research,
2. Mie theory basics (Section 3.2) provides empirical information and the context of the effect,
3. LLS setup (Section 3.3) describes the experiment and used equipment,
4. Particle recognition software (Section 3.3.4) describes the process of particle evaluation from LLS measurements,
5. Setup calibration (Section 3.4) provides inclusive information on the approaching Mie theory in LLS measurements,
6. Morphology transformation of particles on a substrate exposed to plasma (Section 3.5) describes the undergoing physics of micrometer particles exposed to hydrogen plasma,
7. Discussion (Section 3.6) presents the mechanisms of the influence of plasma on particles and their implications,
8. Conclusion (Section 3.7) summarizes the results.

3.2 Mie theory basics

3.2.1 Introduction to the Mie theory

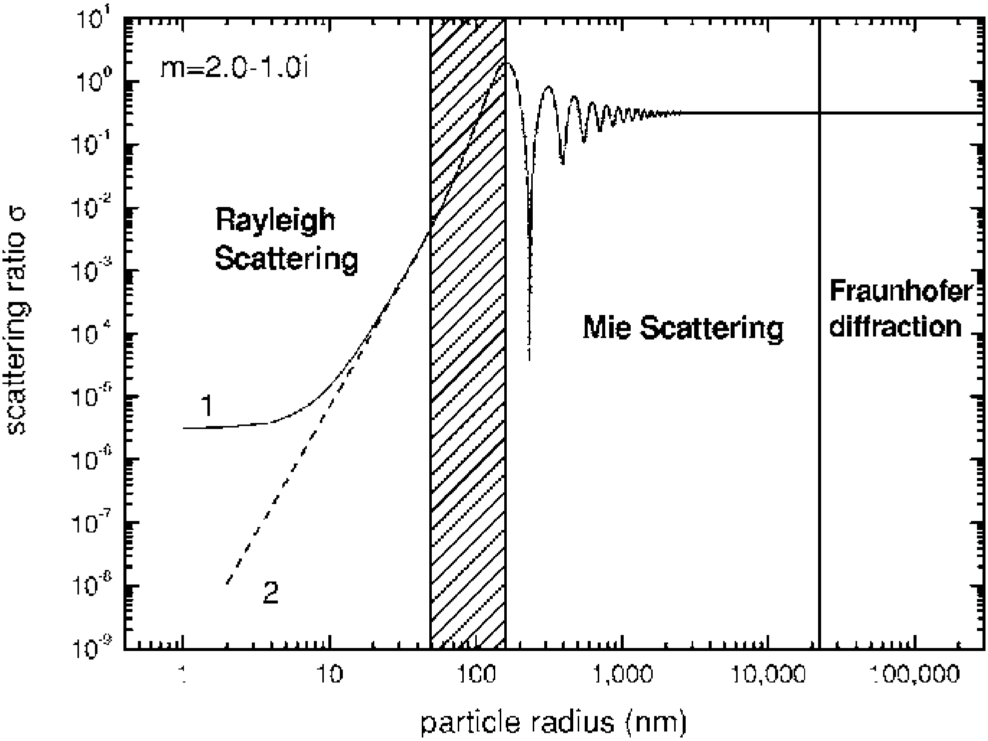

Figure 3.1: The scattering regimes depending on the particle size, calculated at a wavelength of 488 nm. Mie scattering is an intermediate case between two theories with analytical solutions [4]. Labels indicate calculations with (1) and without (2) small particle approximation [5]. The filled area indicates the transition area from Rayleigh to Mie scattering. The image was used with the permission of the author [4].

To describe the scattering mechanisms on particles, there exist Rayleigh diffraction, the Mie theory, and Fraunhofer diffraction, which conditionally classify the scattering of electromagnetic waves into three types based on the size parameter $x = \pi D/\lambda$ (where D is the particle diameter and λ is the wavelength of incident light) and are special cases of solutions to Maxwell's equations. The approximate boundaries of these theories were presented by Hong [4] and shown in Figure 3.1. Scattering on large particles that significantly exceed the wavelength tends toward geometric optics with wave reflections according to Fraunhofer's laws, while scattering on small particles is more complex and depends on multiple parameters.

Fraunhofer diffraction occurs for particles with the size parameter $x = 60$ (> 10 µm in diameter at the wavelength of 532 nm) and larger, according to Figure 3.1. The theory only takes into account the diffraction phenomena occurring at the contour of the particle. Fraunhofer diffraction focuses on the far-field region, considering plane wavefronts. The Fraunhofer diffraction depends on the refractive index of the material and with the first order of approximation nearly independent from the particle size (or curvature). It is widely used to analyze patterns produced by apertures and obstacles [6].

Rayleigh scattering, on the other side, occurs when the incident light interacts with particles whose dimensions are smaller than or comparable to the wavelength, leading to scattering in all directions. The intensity of the scattered light decreases as $\sim d^6$ with particle size and as λ^4 with the wavelength. This wavelength dependency results in the blue color of the sky during daylight, as shorter blue wavelengths are scattered more efficiently by the molecules in the Earth's atmosphere compared to longer wavelengths (Figure 3.2). Rayleigh scattering is an essential process in various fields, including atmospheric science, remote sensing, and optics, and it provides valuable insights into the interaction of light with small particles (less than 80 nm) or molecules.

Figure 3.2: Mie and Rayleigh scattering examples. The figure is denoted to demonstrate two types of scattering: a) Fraunhofer diffraction on large water droplets in clouds. The wavelength does not change, and the clouds seem white; b) Rayleigh scattering of sunlight on atmosphere molecules. The sky seems blue as shorter wavelengths are scattered more efficiently than long red ones.

The Mie theory, at its fundamental level, utilizes Maxwell's equations, which depict the characteristics of electromagnetic waves, to investigate the scattering of light caused by spherical particles. This theory considers not only the diffraction occurring at the particle's boundary but also factors in refraction, reflection, and absorption phenomena both within the particle and on its surface. As a result, the Mie theory is more suitable than Fraunhofer theory for analyzing particles that are comparable to the same order with the wavelength of the light source, such as the suspended water droplets in clouds (as shown in Figure 3.2). However, one of the main limitations of this theory is the requirement for accurate knowledge of the particle's material properties and shapes, including the complex refractive index and absorption coefficient. According to Figure 3.1, the theoretical minimum detection limit for green laser diffraction using the Mie theory is approximately 50 nm.

3.2.2 Mie dependence on complex refractive index

The refractive index n determines the speed of light within a medium and the change in direction (refraction) experienced by light when transitioning from one medium to another. In the context of the Mie theory, knowing the refractive index allows for an accurate calculation of the electromagnetic fields scattered by spherical particles. It accounts for the interaction of light with the particle's surface, including the effects of refraction, reflection, and transmission.

The extinction coefficient k, also referred to as the absorption coefficient, quantifies the rate at which light is absorbed by the material as it propagates through it. In the Mie theory, incorporating the extinction coefficient enables a comprehensive analysis of the absorption phenomena occurring within the particle and at its surface. Knowing k is particularly important when studying particles with optical properties that lead to significant light absorption.

By precisely determining the values of n and k for the material constituting the spherical particle, the Mie theory can provide accurate predictions and insights into the scattering behavior of light. This knowledge allows for the investigation of various phenomena, such as the angular distribution of scattered light, the size and composition characterization of particles, and the determination of particle concentrations.

When light passes through a medium, some part of it will always be absorbed. This can be conveniently taken into account by defining a complex refractive index. The light scatters (or absorbs) at different angles with different amplitudes depending on the complex refractive index m, determined as

$$m = n - ik \tag{3.1}$$

where n is the refractive index or a phase velocity, and k is the index of attenuation. The equation for the light propagation is written as

$$E(z,t) = E_0 e^{i(\tilde{k}z - \omega t)} \tag{3.2}$$

where $\tilde{k}$ is the complex wave number. Rewriting $\tilde{k}$ through a sum of its real and complex components

$$\tilde{k} = k_{re} - k_{im} = 2\pi(\frac{n}{\lambda_{vac}} - i\frac{k}{\lambda_{vac}}) \tag{3.3}$$

and

$$E(z) = \frac{1}{2}c\epsilon|E^2| = E_0 \cdot exp(-2k_{im}z) = E_0 \cdot exp(-\alpha z) \tag{3.4}$$

therefore

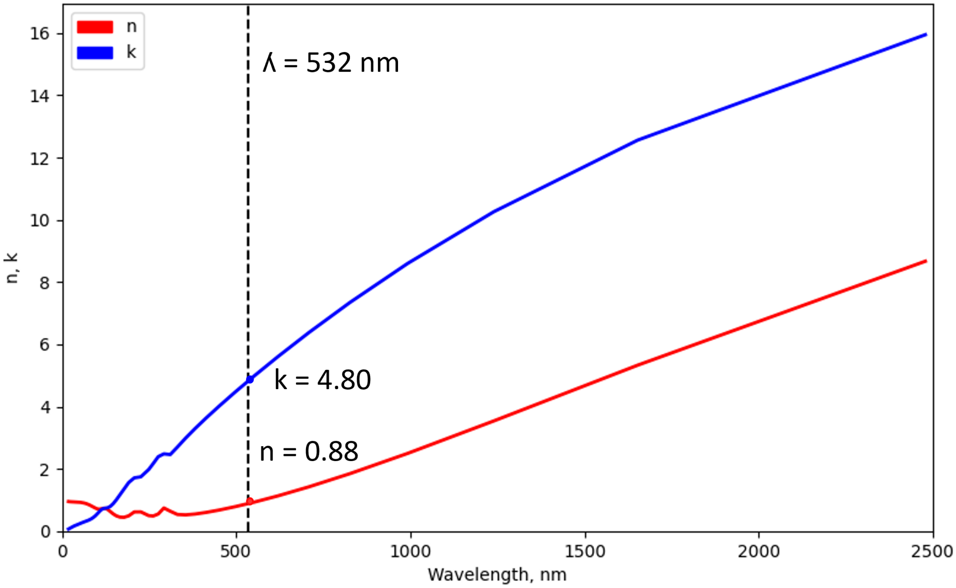

Figure 3.3: Optical constants n and k for zinc (bulk) depending on the wavelength of incident radiation [7]. The dashed line indicates the wavelength of 532 nm corresponding to a green laser used in our experiments. Zinc particles were chosen for demonstration as they were used in our experiments and have a significant extinction coefficient.

$$\alpha = 2k_{im} = 4\pi \cdot \frac{k}{\lambda_{vac}} \tag{3.5}$$

Thus, knowing k_{im} of the complex refractive index ($\tilde{k}$), the absorption coefficient α can be calculated, which will be measured in wavelengths. Here and later we will be referring to k_{im} when using the k letter. For instance, in Figure 3.3, the n and k of bulk Zn (zinc) are demonstrated, taken from Werner [7]. The indicated $n = 0.88$ and $k = 4.80$ obtained by approximation of the given data correspond to the wavelength used in our experiments. It is seen from the graph that the n and k can vary in a wide range. For example, the highest $n = 4.15$ corresponds to Si, and the highest $k = 6.35$ corresponds to Sn, both approximated at $\lambda = 532$ nm [8].

Figure 3.4 illustrates the scattering dependencies of a 1 µm particle with $n = 2.14$, $k = 0$ (left) and a particle with $n = 2.14$, $k = 0.1$ (right) in the wavelength range from 300 to 800 nm. Considering the range of k values presented in Figure 3.3 for Zn, a slight addition in the form of an absorption coefficient can significantly alter the scattering efficiency. Furthermore, the wavelength dependence of the incident radiation should also be taken into account. The dependencies of Mie scattering on various n and k values will be examined in the experimental section below.

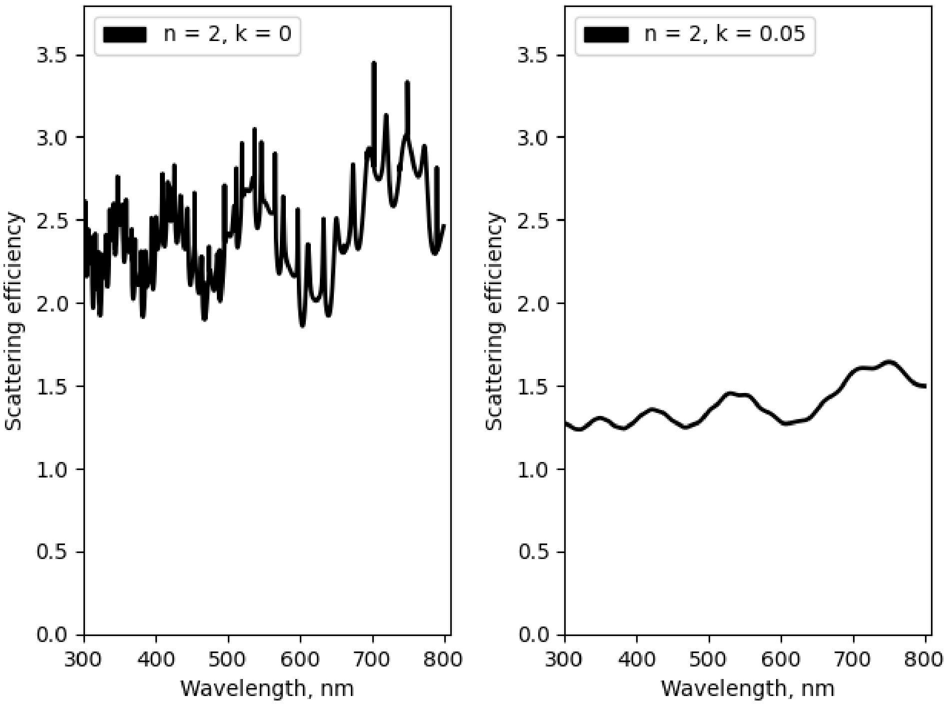

Figure 3.4: Mie dependence on the wavelength for an abstract 1 µm particle with $n = 2$, $k = 0$ (left) and $n = 2$, $k = 0.05$ (right). The figure demonstrates the importance of taking into account the extinction coefficient.

3.2.3 Scattering efficiency and cross-section

Scattering efficiency is a quantity that describes the ratio of scattered photons to the number of incident photons. In other words, this quantity can be considered as a measure of the scattering effectiveness without knowing information about the particle itself.

Scattering efficiency Q can be divided into space-related efficiencies: total scattering, back-scattering, and extinction Q_{scat}, Q_{back}, and Q_{ext} correspondingly. At which

$$Q_{ext} = Q_{scat} + Q_{back} \tag{3.6}$$

The sphere has a finite size, and the incident plane wave is theoretically infinite. The scattering cross section σ_{diff} allows us to characterize the interaction between the two. It is defined as the ratio between the scattered power (in W) and the illumination of the incident wave (in Wm^{-2}). Intuitively, it is clear that the shadow cast by an opaque sphere of radius a has a surface area of πa^2, so we often compare the scattering cross-section with this cross-section, determining the scattering efficiency Q_{diff}. Scattering and absorption cross sections σ have units of area and can be obtained from the efficiencies by multiplying them by the geometric cross section πr^2 of the sphere.

$$\sigma = \pi r^2 \cdot Q \tag{3.7}$$

therefore

$$\sigma_{abs} = \sigma_{ext} + \sigma_{scat} \tag{3.8}$$

3.3 LLS setup

3.3.1 Vacuum and plasma

A schematic overview of the used setup is depicted in Figure 3.5. The setup comprised two vacuum chambers (a main chamber for the plasma and gas jet exposures and a load-lock chamber) separated by a VAT gate valve that remained closed during experiments. The main chamber was a 20 x 20 x 20 cm^3 cube with one of the flanges used for connecting to the plasma source and the gas supply. A second flange of this chamber had an integrated window with an anti-reflective coating for LLS imaging. A third flange of this chamber was equipped with Philips vacuum gauges (HPT 200 Pirani/Bayard-Alpert and PPT 200 AR), which were both hydrogen calibrated. The flange with the plasma head also held a stainless steel wafer holder and allowed the swapping of wafers via the load-lock. The ultimate pressure in the vacuum chamber, achieved by a turbo-molecular pump (Pfeiffer THU 200 MP) and a scroll dry pre-pump (Edwards XDS10), was 10^{-4} Pa.

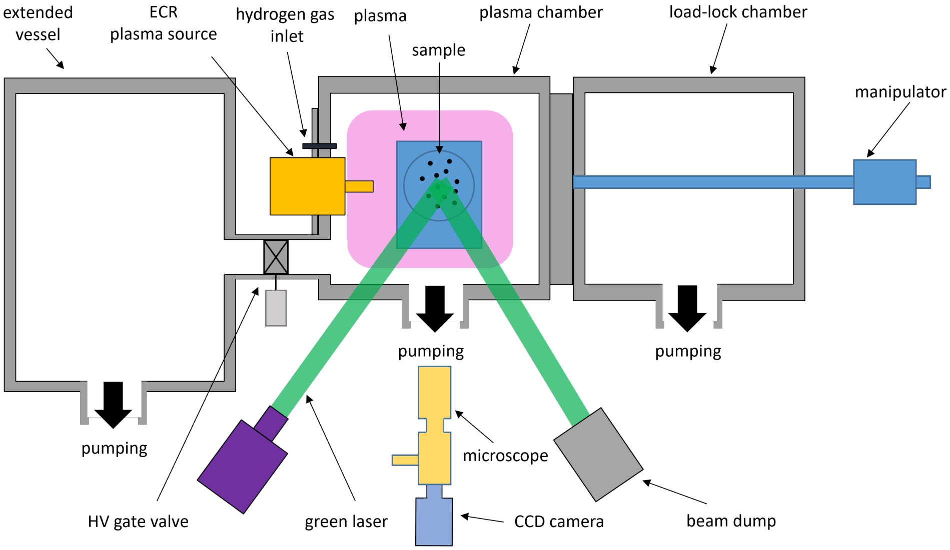

Figure 3.5: Schematic illustration of the used setup.

The hydrogen plasma in the experiments simulated the conditions of EUV-induced plasma with increased intensity. A release of particles near critical surfaces in EUV-induced plasma is rare and typically requires prolonged exposure to radicals and ions [9]. The experiment conditions in this study featured a 100x higher ion flux and 5x higher ion energy compared to EUV-induced plasma [10]. Thus, we expect a significant (100x) acceleration of the plasma-induced effects on the particles, assuming that most effects, based on etching or accumulation of hydrogen, should scale with ion dose or faster, as described by Kirchheim [11]. Plasma was maintained at 5 Pa, a typical pressure used in EUV environments [12]. The input RF power for hydrogen plasma was 100 W. The RF generator was tuned in a resonance frequency mode at about 2.45 GHz. During plasma exposures, the sample temperature reached about 50–70 °C. The Aurawave ECR source generated plasma with $T_e \cong 5$ eV and $n_e \sim 10^{16}$ m^{-3}, same as the one used by Shirai *et al.* [13].

Similarly to the previous chapter, we estimated that we have a uniform flux of ions to the wafer I $\sim 10^{14} - 10^{15}$ cm^{-2} (0.1–1 Am^{-2}) with ion energy obtained in the plasma sheath $E_i = 4 \times T_e$ or 20 eV [10]. Hydrogen radical (H*) flux is assessed to be 10 to 100 times higher than the H$^+$ flux due to a ∼ 10% chance of H* association at the walls of the main vacuum chamber compared to the ∼ 100% chance of H$^+$ loss by neutralization at the walls [14]. In addition, recombination of H_3^+ or H_2^+ ions generates ≅ 2 radicals per event [15].

As demonstrated in the previous chapter, SEM or Atomic Force Microscopy (AFM) inspection are widely used methods to study the presence of particles and changes in particle morphology in stresses such as plasma [16, 17]. One can evaluate the adhesion of the particles based on the surface and particle morphology and the basic sphere-to-surface interaction model, with the expansion of the model including asperities, particle resettling, rolling, etc. Here, we combine the SEM/FIB measurements with the light scattering on particles.

3.3.2 Imaging of particles

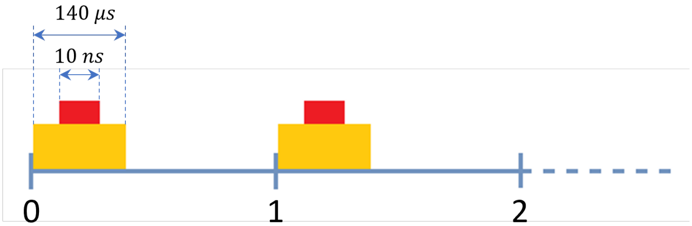

Figure 3.6: Schematic illustration of the synchronization timing between the camera and the laser system. The red parts represent the laser pulse durations, and the orange parts represent the open time of the camera's shutter. Numbers 0, 1, 2 ..N indicate the laser pulses. The time between the pulses was 1.4 s.

For typical experiments, a sample with particles was brought through the load-lock chamber to the middle of the main chamber using a manipulator and mounted vertically, facing the window with an anti-reflecting coating. A pulsed laser (EverGreen EVG00200, 70-200 mJ and 10 ns long pulses at 532 nm with 100-1000x attenuation by a grey filter) illuminated the wafer with a repetition rate of 0.71 Hz (1.4s between pulses). The laser beam, guided by mirrors, was expanded to 0.5 cm in diameter by two plano-convex lenses and entered the chamber through the window at about 10°, reflected from the metal surface of the wafer, exited the chamber at 10°, and was finally directed to a beam dump. The light scattered by particles on the surface was collected by a long-distance microscope (Distamax K2) with a working distance of 180 mm and a fully open aperture with a CMOS camera (FLIR Grasshopper3) mounted on it. Pulsed laser illumination was chosen instead of illumination by a CW laser to reduce the blurriness caused by the vacuum pump-induced vibrations transferred to the microscope.

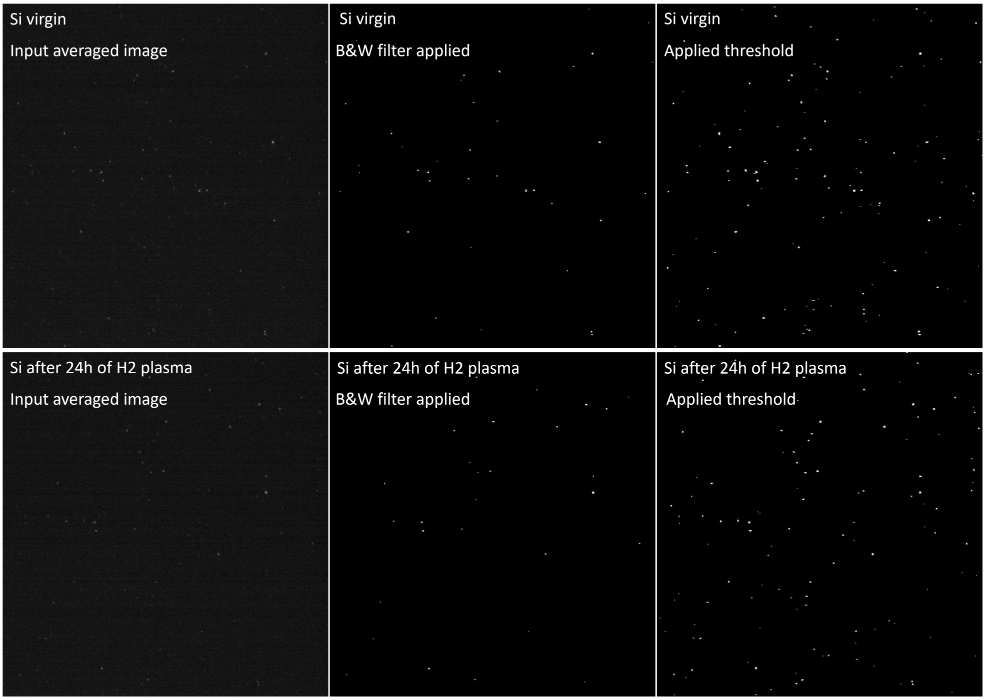

Figure 3.7: The images of Si particles captured with the camera (virgin on the top and exposed to a hydrogen plasma for 6 h on the bottom) and recognition filters applied.

The camera shutter was synchronized (Figure 3.6) with the laser pulse with a signal delay generator (Model 577, BNC). Relatively short (140 µm) camera exposures helped to reduce the impact of the light from the plasma on the image background signal. The camera was configured to save 24-bit images with a resolution of 4,096 x 2,160 pixels. The pixel size was 3.45 x 3.45 µm^2, the quantum efficiency was 64%, and the dynamic range was 65.15 dB. The maximal camera noise was 40.3 dB. The CMOS matrix size, in combination with magnification by Distamax K2 and the distance to the sample (around 18 cm), produced a field of view (FoV) of 3 x 2 mm. This microscope FoV with a fully opened diaphragm was aligned with the illumination laser spot and the contaminated center of the wafer. The following camera settings were used: gain 48, gamma 0, black level 0, balance ratio 1.14, digital zoom - off, picture enhancer - off, full automatic control - off, auto exposure - off, auto white balance - off, black & white compensation – off. The camera's gain had the greatest influence on the recognition of particles in post-processing steps.

The acquired images (Figure 3.7) were analyzed by a self-developed Python script described in Section 3.3.4. This script extracted the number of particles, their coordinates, and total integrated intensities and sizes. Following is a discussion of how the Mie theory was used to determine particle size distributions. To minimize the impact of laser beam power density fluctuations (Figure 3.8), the script applied a running average of 5 over the images, which was found to be an optimal value for the trade-off between the noise level and the time resolution achieved. The averaged total integrated scattering (TIS) of an image was computed by the script by summing the intensities of all pixels.

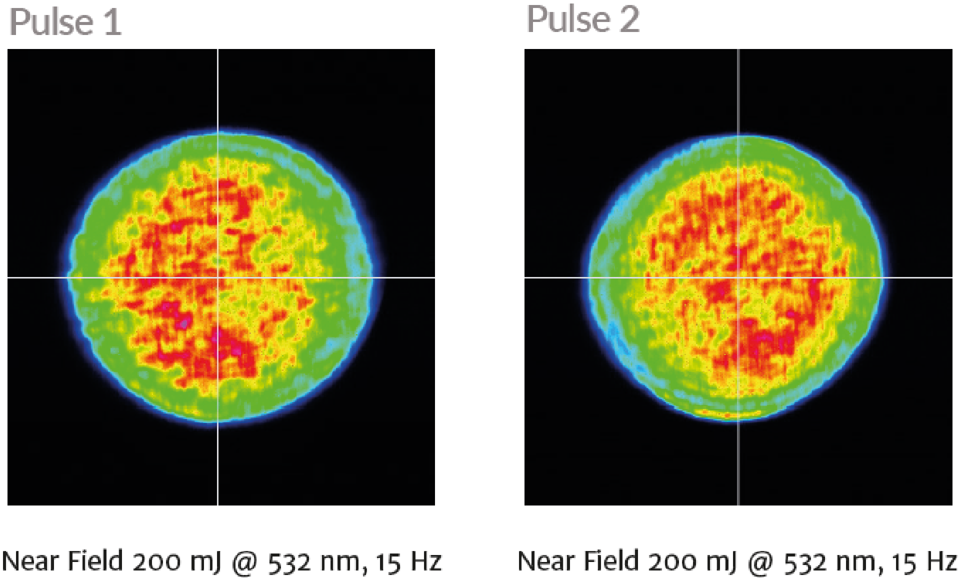

Figure 3.8: A typical energy distribution in a laser beam profile used in the experiments for two different shots [18].

In addition, to ensure the accuracy of the LLS setup calibration for measuring the sizes of Si (silicon) particles, a sample with silicon particles was additionally (measured on a similar, but not the same sample) qualified using SEM. The size distribution diagram obtained by SEM in a scanned area of 3 x 3 mm and analyzed by self-developed software was compared with the size distribution diagram obtained by LLS.

3.3.3 Flushing

The main chamber was also equipped with a flushing jet, which exhausted gas pulses through a 4 mm nozzle tube placed at a 5 mm distance from the wafer and facing its center at 45°. The internal part of the vacuum chamber and the orientation of the flushing tube are depicted in Figure 3.9. The left figure clearly shows the pass of the laser beam into the chamber through the window, its reflection from the dusty substrate with particles, and its exit. The flushing tube is positioned above and directed toward the center of the substrate.

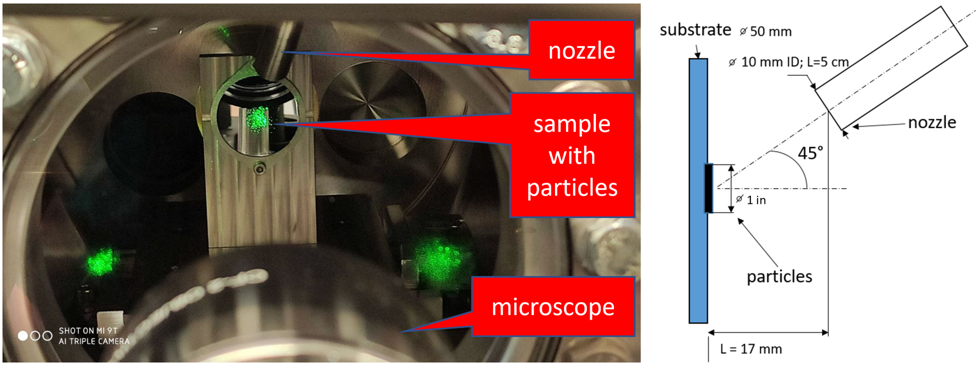

Figure 3.9: The left figure represents the picture of the inner part of the vacuum vessel. It is seen in the propagated laser beam, contaminated wafer, and flushing nozzle facing the substrate with particles. The right graph schematically depicts the orientation of the nozzle tube.

Flushing was used for two reasons: 1) to study the behavior of particles when a non-electric external force is applied and 2) to track changes in particle adhesion before and after plasma exposure. Flushing could be used to remove loosely bound particles from the substrate when the shear force exceeds the vdW force with which the particles are bound to the surface.

The shear stress force caused by the flushing was numerically calculated in a model mimicking the conditions in our chamber. In the model, pressure, flow, and direction were the varying parameters. Figure 3.10 shows a calculated curve. At the pressure of 100 Pa (1 mbar) and the flow of 1 nlm, the maximum shear force reached 4.5 N. At the pressure of 1000 Pa (10 mbar) and the flow of 1 nlm, the maximum force reached 10 N.

The effectiveness of flushing was experimentally tested on a group of samples containing particles of various sizes. The particles used in the tests are shown in Table 3.1. As part of the experiment, the particle sizes were varied, and the efficiency of flushing (percentage of flushed particles) was evaluated. Two types of flushing methods were employed: continuous flow and pulsed flushing.

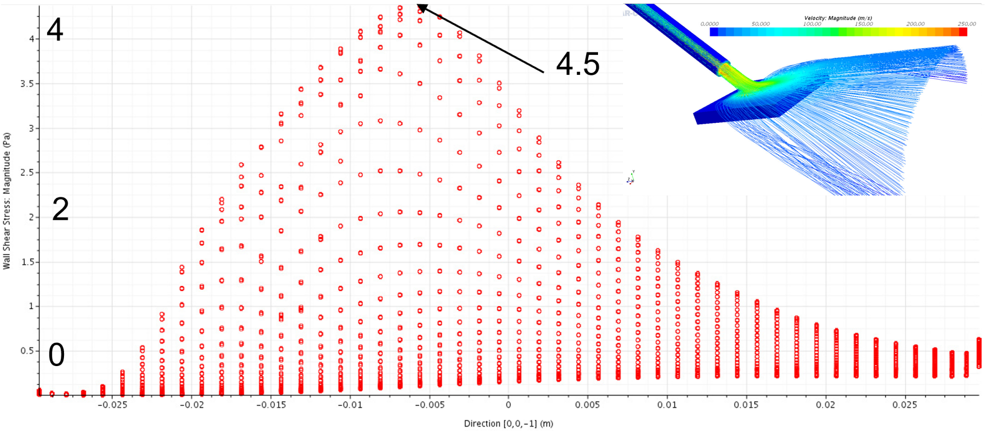

Figure 3.10: The modeling of the shear force applied to the particles during exposure to flushing. The X-axis represents the direction of the flow, and the Y-axis represents the applied shear force in N.

№	Material	Mean size (µm)	Manufacturer
1	glass spheres	10	Sigma-Aldrich
2	Si	5	Sigma-Aldrich
3	SiC	2	Sigma-Aldrich
4	Ni	2	Sigma-Aldrich

Table 3.1: List of particles used in the flushing tests.

In the continuous flow, the particles were subjected to a gas flow of 1 nlm, while the pressure in the main chamber was maintained at approximately 100 Pa. The pulsed flushing was realized through a quick valve (DVI 005 M Pfeiffer) with an opening time of 30 ms and a calibrated orifice (0.04 inches, Swagelok) that limited the flow. The pressure in the nitrogen line was measured by a Pfeiffer gauge (CPT 200 DN). In this configuration, gas accumulated in the reservoir behind the valve, and upon valve opening, it rapidly flowed into the chamber through the orifice. The main chamber had a bypass line to a volume extension vessel of 100 liters, separated from the main chamber by a VAT HV gate valve. During the flushing experiments, the turbo-pump was switched off, and the bypass line was open. During plasma experiments, however, the bypass line remained closed. The extended vessel had its own pre-pump (Leybold SCROLLVAC 10). The sum productivity of the two pre-pumps for flushing experiments resulted in about 5 l/s at 100 Pa. The pulse duration was set to 3 s, with approximately

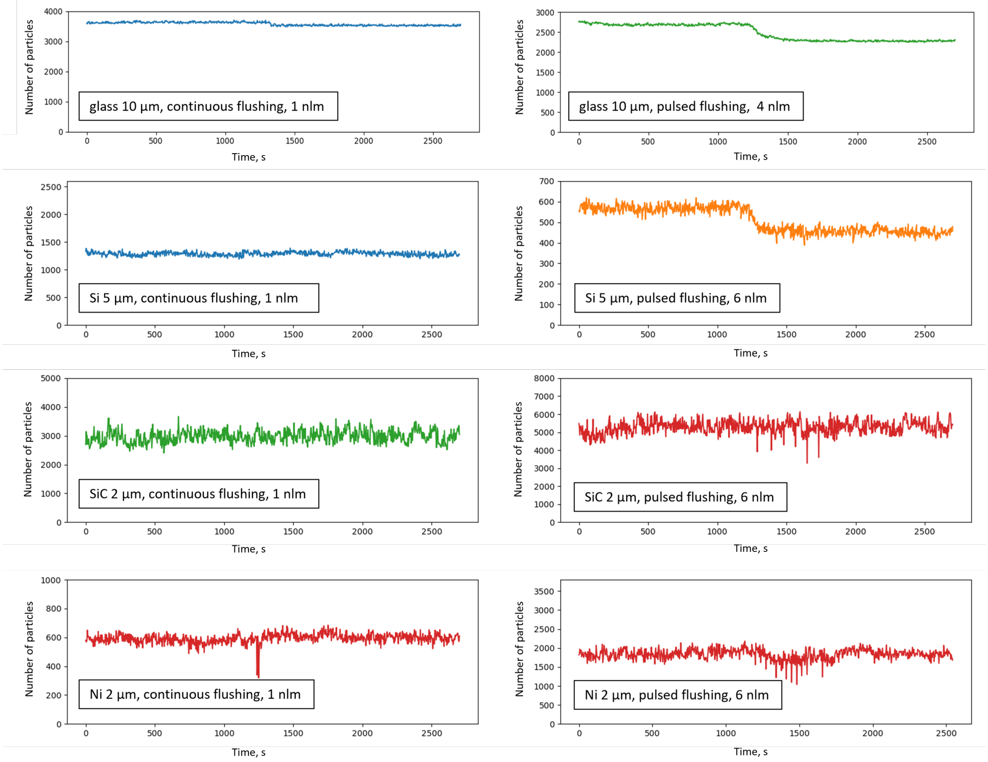

Figure 3.11: Flushing tests, the comparison of the pulsed flushing and continuous flushing based on the samples listed in Table 3.1.

100 s between pulses. The flushing line reached 0.75 × 10^5 Pa (0.75 bar), while the pressure in the main chamber with the samples at the moment of valve opening was 10 Pa (0.1 mbar). The flow through the orifice in a pulse was calculated based on the pressure difference in the flushing line and the chamber using an airflow calculator [19]. The pulsed flushing jet could reach up to 6 nlm at the peak of the pulse.

The results of the test are presented in Figure 3.11. During the experimental procedure, a baseline measurement was recorded for the initial 20 minutes, followed by a 5-minute flushing campaign, and afterward, a second baseline measurement was taken. The continuous flow method had a minimal observable impact across all experiments. The most significant effect was on the largest glass 10 µm particles. The continuous flow approach demonstrated limited effectiveness for smaller particles. In contrast, the pulsed flushing exhibited a decreasing trend in effectiveness with particle sizes. Notably, the impact was observed for 10 µm particles, even at a lower flow rate of 4 nlm. Exposure to the pulsed jet resulted in the removal of approximately 25% of Si 5 µm particles. However, the removal of smaller particles was found to be ineffective, as the signal was comparable to the noise level. In both types of flushings, the particles were effectively removed only for the first few seconds. The rest of the flushing exposure did not result in any additional particle detachments, which correlates with the literature data [20].

3.3.4 Particle recognition software

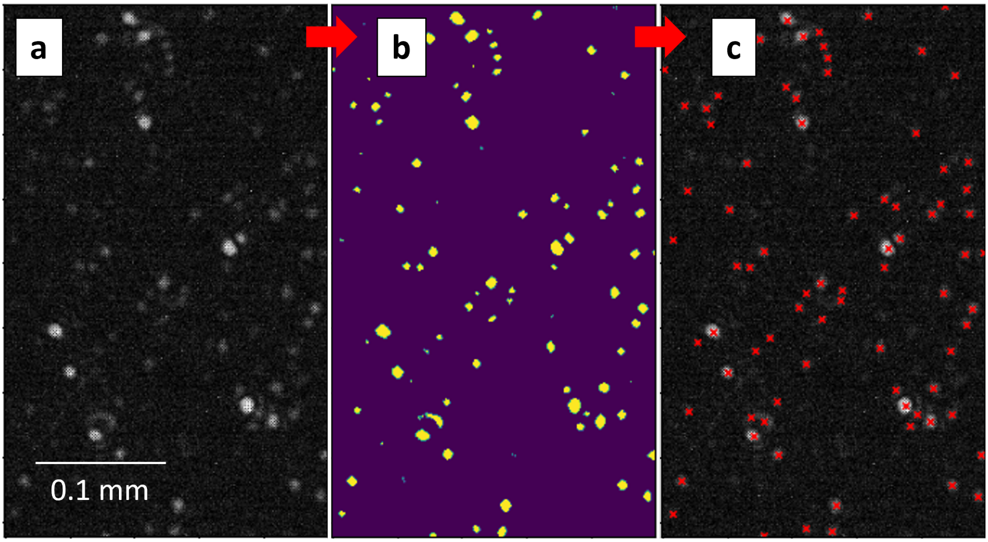

Figure 3.12: Particle recognition stages.

The recognition of particles in an image using Python libraries such as SciPy [21], OpenCV [22], and scikit-image [23] has emerged as a powerful method for particle analysis and characterization. These libraries offer a comprehensive toolset and functions that facilitate image processing, feature extraction, and particle recognition.

In our experiments, a script was developed that leveraged the advantages of the aforementioned libraries. In simplified terms, the algorithm of the script for evaluating the particles was as follows:

1. The average intensity of five images was calculated to account for laser profile fluctuations (Figure 3.12a).
2. A threshold was applied to the image to minimize camera noise (Figure 3.12b).
3. The remaining bright spots were detected, and their sizes in pixels were determined.
4. All particles with sizes smaller than 10 bright pixels were filtered out (Figure 3.12c). This is the reason why not all yellow particles in the middle figure are indicated with X-marks on the right graph. This step was necessary to eliminate the smallest particles that appeared and disappeared within the camera field of view, thus contributing significantly to the noise. Additionally, this filter helped remove most of the "dead" pixels.

5. The remaining particles were converted into data, including the number of particles, particle sizes in bright pixels, particle intensities in counts, image intensity in counts, etc., and were written into a file.

Subsequently, the obtained intensities per particle were analyzed taking into account the Mie theory described above in Section 3.2.

3.4 Setup calibration

The LLS technique enables change monitoring in the number of attached particles (Figure 3.7), as well as changes in the size distribution during exposure to plasma and flushing. The samples used in the calibration are described in Section 3.4.1. To demonstrate the stability of the optical system, a seven-hour measurement of fixed-size particles (melamine) is used to calibrate the counting of particle numbers (see Section 3.4.3). Furthermore, a calibration for obtaining particle size distributions is performed based on the Mie theory with a correction for the refractive index (see Sections 3.4.4 and 3.4.5). The calibration of the total substrate scattering is shown in Section 3.4.6. The demonstration of the LLS method on Si particles and its comparison to the literature is shown in Section 3.4.7. Finally, the summary of the LLS calibration is discussed in Section 3.4.8.

3.4.1 Samples

The methods of particle deposition used in the experiments were similar to those presented earlier in Chapter 2.3.2. The particles and their characteristics are listed in Table 3.2. Melamine resins were used for calibration with the narrow size distribution profile, while Si was used for method demonstration.

№	Material	Mean size (µm)	SD (µm)	Manufacturer
1	melamine resin	2.15	0.04	Sigma-Aldrich
2	melamine resin	2.94	0.05	Sigma-Aldrich
3	melamine resin	5.26	0.08	Sigma-Aldrich
4	silicon	5.00	-	SigmaAldrich

Table 3.2: Samples of particles used in the calibrations and experiments. Size is the diameter of the particle, and SD is short for standard deviation. Melamine particles were purchased from microParticles GmbH, silicon particles were purchased from US Research Nanomaterials, Inc.

3.4.2 Geometry of the scattering

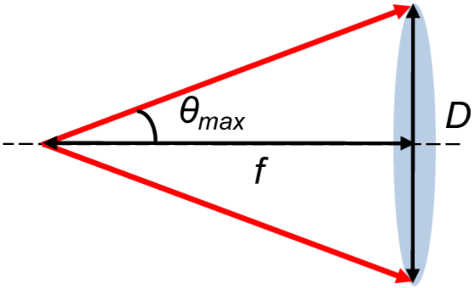

Figure 3.13: Numerical aperture.

To determine the captured fraction of scattered particles, it is first necessary to determine the values of the numerical aperture (NA). The numerical aperture is a fundamental parameter in optics that characterizes the light-gathering ability of an optical system. It is defined as the sine of the half-angle of the largest cone of light that can enter or exit the system. The numerical aperture is influenced by the refractive indices of the medium through which light propagates and the geometrical characteristics of the system, such as the size and shape of the lens or the objective. Figure 3.13 illustrates the geometric definition of NA, which is calculated as

$$NA = n \cdot sin\theta \tag{3.9}$$

The figure below shows the basic idea of the scattering geometry. An incoming monochromatic plane wave hits a sphere and produces in the far field two separate monochromatic waves - a slightly attenuated unscattered planar wave and an outgoing spherical wave. In our experiment, a flat wave of light is incident on a single particle and is scattered at various angles. Larger particles predominantly scatter forward and backward, while smaller particles, comparable in size to the wavelength and smaller, scatter in approximately all directions (in 4π). In the setup configuration depicted in Figure 3.5, not all the scattered light reaches the microscope's objective lens. In our model, the particle is assumed to be located coaxially with the microscope objective at a distance of $f = 18$ cm. The width of the microscope objective is $D = 5$ cm (see Figure 3.13). Thus, the NA of our system, according to Equation 3.9, is 0.137.

In Figure 3.14, the schematic diagram illustrates the geometry of particle scattering and the portion of radiation captured within the NA of the microscope. As the particle is situated on a reflective metallic substrate, the microscope captures both the backward-scattered radiation and the forward-scattered radiation from the particle that is reflected off the substrate. However, a physical difference from the model is that the Mie theory assumes an isolated sphere. Thus, near-field effects associated with the light reflected from the substrate were not taken into account.

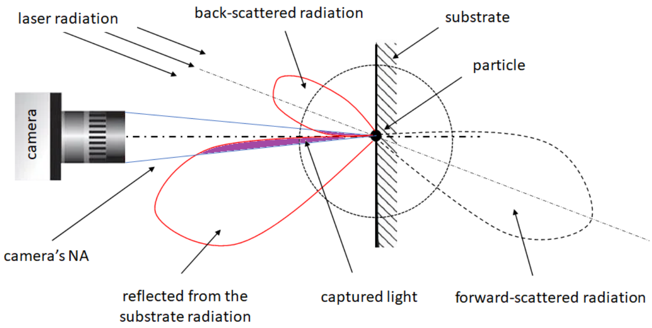

Figure 3.14: The schematic geometry of the light captured by the microscope in the used setup.

3.4.3 Particle number evaluation

Evaluating the number of particles on the surface is challenging. For example, the resolution of the long-distance microscope is limited by the Abbe diffraction limit determined by the closest distance at which two separate sources of light can be distinguished from one another. This limit is expressed by [24]

$$d \approx \frac{\lambda}{2NA} \tag{3.10}$$

where d is the minimum resolvable distance between the two sources of scattered light, λ is the wavelength of the laser light (532 nm), and NA is the numerical aperture (which in our configuration equals 0.137). Therefore, the resolution of our system is limited to approximately 1.9 µm.

The imaging of particles is limited not only by Abbe diffraction but also by the physical vibrations of the optical system and variations of the particle shape and composition. In our experiments, the influence of camera noise, intensity fluctuations of the laser beam, and laser multimodality were also noted. Due to the limited coverage of these effects in the literature, comparisons were not made. Experimental uncertainties can be evaluated from measurements of scattering light from a stationary sample without disturbances. To enable this evaluation, a 7-hour-long imaging experiment of highly monodisperse 5.26 µm melamine spheres (see Table 3.2 with samples) was conducted. Note that in this experiment, no flushing or plasma exposure was applied. The results (Figure 3.15) demonstrate high laser stability and low counting uncertainty. In this experiment, the laser illumination and camera settings were identical to the experiments with plasma and flushing. It was shown that the dispersion of the number of detected particles was about 3% (which is the lowest achievable noise level) with no long-term trends.

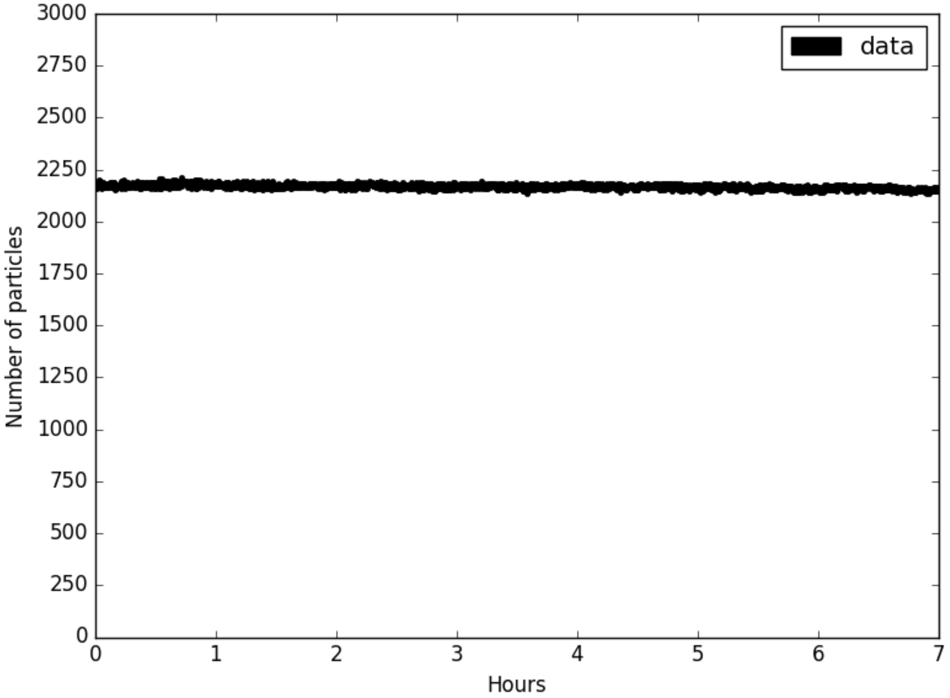

Figure 3.15: Calculated number of particles for a 7-hour-long camera baseline recorded for 5 µm melamine spheres (see Table 3.2).

3.4.4 Size distribution of particles in LLS

Knowing the size distribution of processed particles is important. For instance, if large particles are more subjective to external stress factors by lowering their adhesion, such as those induced by exposure to plasma or a gas jet, the size distribution could change. On the other hand, if exposure to plasma leads to a developed surface and, thus, to a higher reflection coefficient of the incident light, the growth of asperities will be associated with larger particle sizes.

The determination of the particle size distribution is even more complicated than the counting of particles. As generally known, CCD and CMOS cameras can be subjected to an effect called "blooming" [25]. This blooming means that oversaturated pixels leak excess charge to their neighboring pixels. This process propagates until it reaches the edge, visibly and virtually enlarging the particle (Figure 3.16).

Illumination of the entire particle requires sufficient illumination, and most of the particles under study scatter light in the flat Top-Hat regime, which means oversaturation of the pixel capacity. Hence, the detected particle size as a number of bright pixels above the threshold is not consistent with the true particle size. A 2 µm particle occupied around 50 bright pixels (about 7 pixels in diameter) on the camera

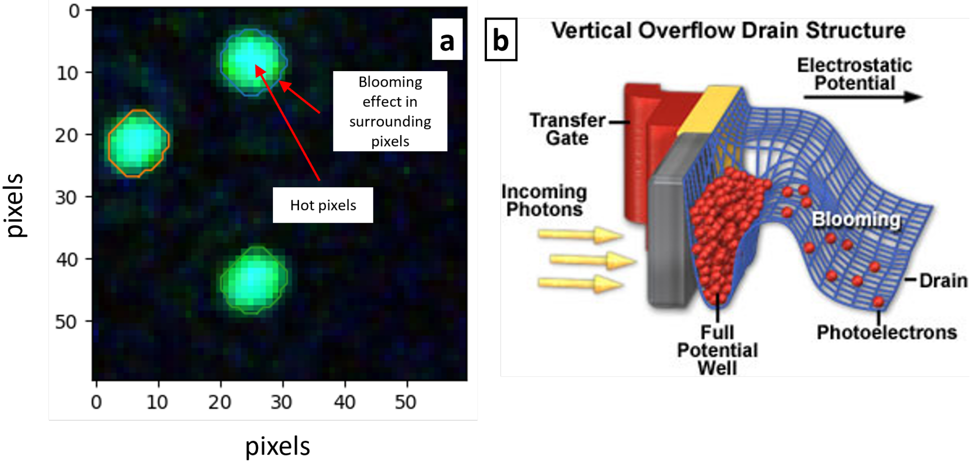

Figure 3.16: The demonstration of the blooming effect: a) Melamine 2.14 μm particles detected in LLS. The figure is the average image of 5 laser shots with the applied threshold. The electrons in hot pixels leak to the neighboring pixels. The surrounding curves denote the determined particle size in pixels. b) The blooming effect in a CCD matrix (image has been used with permission from Hamatsu [26]). The leakage of a pixel charge from a potential well is shown.

when in FoV. The only invariant in this problem is the integral of the photo-induced electrons in the camera matrix or, in other words, the scattering efficiency of individual particles.

Additional filtering must be applied before integrating the intensities of the pixels imaging the particles. After averaging the intensities of 5 images and applying the threshold value, the script filters tiny features (below 10 bright pixels in size). There are two reasons for this filtering. The first reason is that the high camera gain (max value, 48), used for high sensitivity, produces a few hot pixels that occur even without laser illumination and do not correspond to an actual signal. These hot pixels must be removed. The second reason relates to the presence of particles with sizes close to the detection limit. Due to the fluctuating laser intensity, these detections can appear and disappear from the detection region, significantly enhancing the noise level. Thus, by removing them, we focus on the residual population of particles that can always be identified with high confidence.

Without knowing the blooming effect, the size distribution histograms (normalized number of particles versus their size) would look like the ones demonstrated for particle sizes of 2.14, 2.94, and 5.26 μm in Figure 3.17. These histograms show the distribution of particles occupying a certain area in pixels. The laser intensity was gradually increased for smaller particles that scattered less light. From the figures, the inconsistency of this approach can clearly be seen. The particle areas are not linked with the sizes of the calibrated melamine particles listed in Table 3.2 at any conversion constant, indicating the need to take into account the above-mentioned

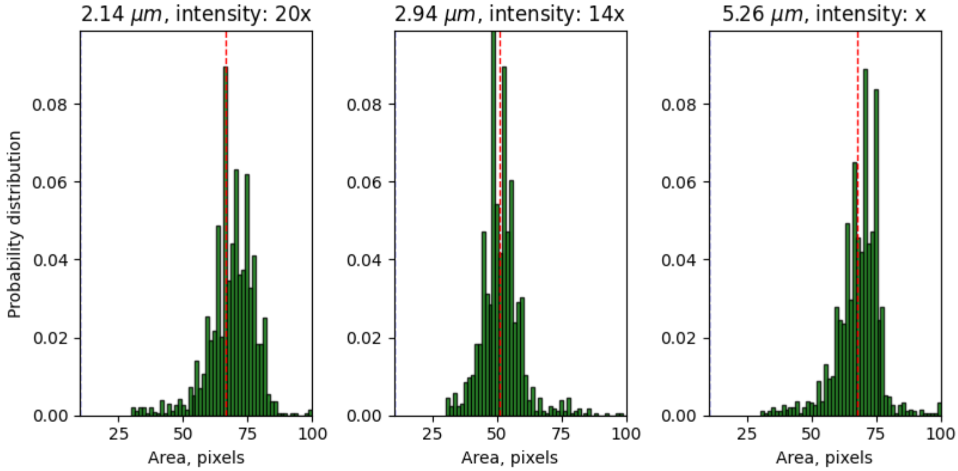

Figure 3.17: Observable size distribution of the melamine particles from Table 3.2 obtained in LLS without using Mie modeling. The red dashed line indicates the mean value of the histogram data. The histograms show the inconsistency of the approach when the size of the particles is obtained by just counting the bright pixels above the threshold. The smallest particles of 2.14 µm in size appear to be larger than 2.94 µm and about of the same size as 5.26 µm particles. The particle scattering efficiency must be considered instead.

blooming effect.

The correct approach would be to look at the scattering intensity of individual particles. As is generally known, particles of several micrometers in size obey the Mie scattering theory [27]. The algorithm processing the collected images worked as follows. First, the scripted averaged intensities of 5 captured frames. Second, after applying the threshold, the mage intensities of the particles with an area larger than 10 pixels were integrated. Third, the scattering cross-section of the particle was calculated by multiplying the total intensity by the particle size with a constant, which is a fitting parameter to this model (see Equation 3.4.5). Finally, an equivalent sphere with the same scattering cross-section and a refractive index was calculated using the Mie theory, from which the size of the sphere/particle was derived. Therefore, measured scattering cross-sections can be translated into actual particle sizes using the Mie model for the light scattering by an individual particle. For this, a Mie calculator [28] was used to evaluate the effective cross-sections of the particles for different particle sizes (from 0.1 to 7 µm). The absorption of light by the particles was not taken into account in the calculations due to the lack of available data. The results of the calculations for particles with a variety of refractive indices n from 1.87 to 4.15 and the light collected in the NA corresponding to the microscope are plotted in Figure 3.18.

The variation of k is demonstrated in Figure 3.19. As can be seen from the graph, the extinction coefficient k is more important for bigger particles (> 5 µm).

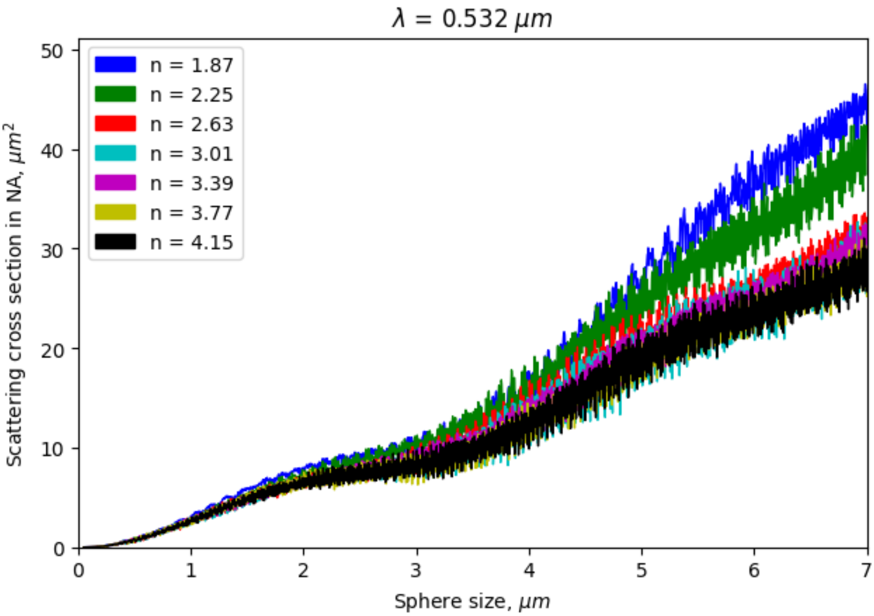

Figure 3.18: Plot of the results from the Mie scattering model as a function of different sizes and the real part of refractive indices (n) scattered in the microscope NA. The selected n varied from 1.87 (melamine) to 4.15 (silicon).

For melamine-based materials in the visible range, the extinction coefficient is approximately zero ($k = 0$) [29]). Furthermore, the coefficient k becomes more significant at large angles of incident light on the particle. In our configuration, where the incident light angle was approximately 10° (close to a normal incident), the difference was minimal when taking k into account.

In the Mie model, a spherical particle is situated in a vacuum and emits light in all directions. Particles whose sizes are several times larger than the wavelength of the incident radiation predominantly scatter light forward and backward. We considered a model in which particles are positioned on a reflecting substrate, thus collecting only a portion of the forward and backward scattering into the NA of the microscope (NA $= 0.137$ for an objective lens with a diameter of 5 cm and a distance of 18 cm from the particles). It is worth noting that near-field effects, due to reflection from the substrate, were not taken into account. All calculations were performed assuming an isolated particle in a vacuum with scattering confined to the chosen NA of the microscope.

This graph shows that the particle composition (i.e. the particle refractive index) is more important for bigger sizes. Smaller particles are more sensitive to shape alterations. Our approach is to measure the scattering efficiency for the particles of known size and composition (in our case, monodisperse melamine spheres) as calibration. After this, for any material (i.e. refractive index) of interest, the

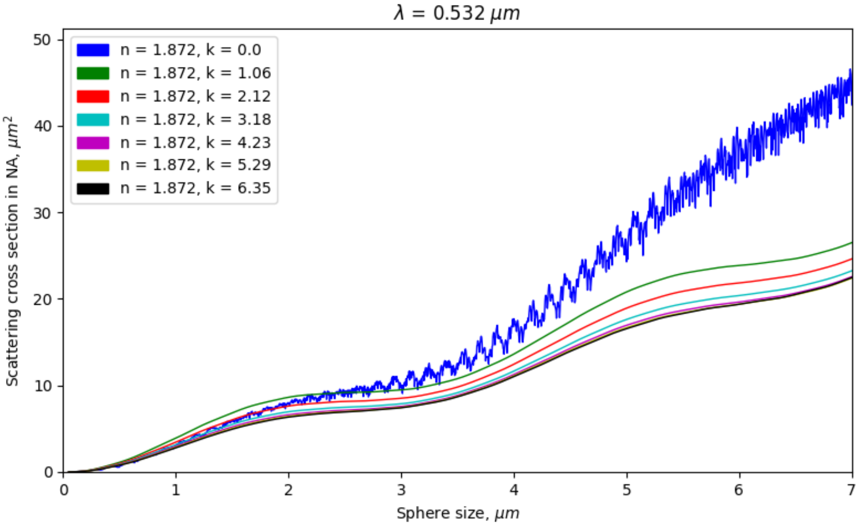

Figure 3.19: Plot of the results from the Mie scattering model as a function of different sizes and complex refractive indices (k) scattered in the microscope NA. The real part of the refractive index n was kept constant at 1.87 as for melamine. The selected k varied from 0 (melamine) to 6.35 (tin).

cross-section of each particle can be translated into the size using the corresponding calibration curve from Figure 3.18.

3.4.5 Effective scattering cross-section calibration

To use the curves from Figure 3.18, they have to be calibrated. The measured intensities were fitted with Mie curve. The results of this fit can be seen in Figure 3.20. The arrows indicate the measured cross-sections. The blue dashed line indicates the I_o value and can be considered as the detection limit of this method (it is attributed to the camera noise, which is the same size as the min detected particles). The sizes of the particles were declared rather monodisperse, according to the manufacturer, with only a small standard deviation (see Table 3.2), while the measured intensities had some uncertainty. The scattering cross-sections of the melamine particles were fitted using the formula

$$I_{ec} = (1/\alpha)AI_m + I_o \tag{3.11}$$

where I_{ec} is the effective scattering cross-section, and I_m is the LLS measured particle intensity. The constant A equals 700 and is related to the conversion of the laser intensity to the camera counts. The constant α is the intensity correction

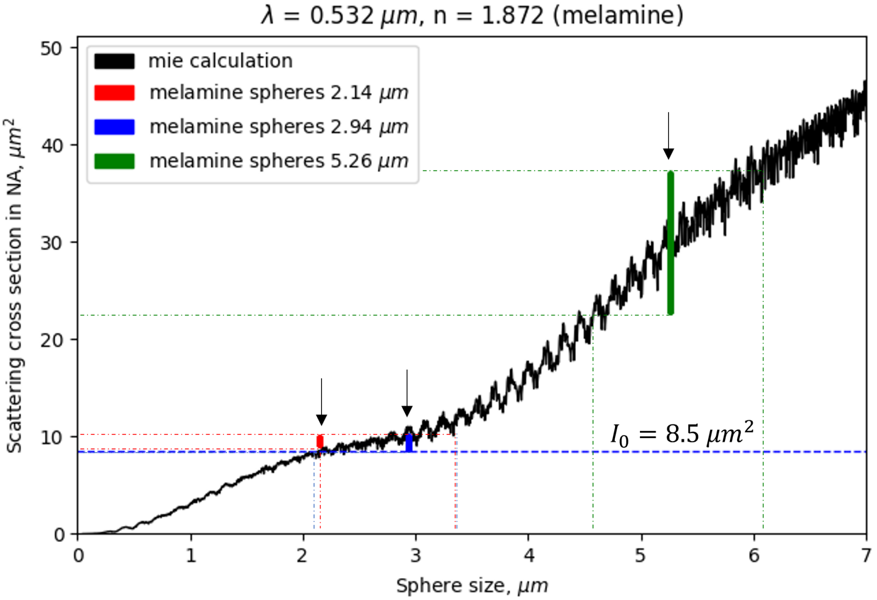

Figure 3.20: Calculated Mie scattering cross-section for a single melamine ($n = 1.872$) particle depending on its size (black line). The arrows indicate the fitted measurements of the calibrated melamine particles from Table 3.2 using Equation 3.4.5. The horizontal blue dashed line indicates the I_0 value, which is equal to 8.5 μm^2 and can be considered as the detection limit of this method.

factor. As was shown in the histograms (see Figure 3.17), the applied laser intensity changed from 1x to 14x, and 20x depending on the size of the particles, i.e. 2.14, 2.94, and 5.26 μm particles respectively. Therefore, for laser intensity normalization, the intensity factor α was taken equal to 1, 14, and 20 for measurements on 5.26, 2.94, and 2.15 μm particles respectively. The parameter I_o remained constant for all fits and was taken equal to 8.5 μm^2. Physically, it can be attributed to the losses of higher diffraction orders, reflections from substrate asperities, and camera noise.

The uncertainty of the cross-sections (and the size uncertainty related to it) can be considered error bars of the method. For example, the determination of the size of the 2.14 μm particles has an uncertainty of about ±1 μm, which is 50% of their size. It explains why 2.14 and 2.94 μm particles appear to have the same scattering cross-sections. At the same time, the determination of the size of the 5.26 μm particles has an uncertainty of about ±0.5 μm, which is only 10% of their size.

3.4.6 Calibration of the total substrate scattering

In addition to the measurements of the number of particles and the particle size (distribution), another possibility is to look at the TIS signal from the microscope field of view. Technically, the summed and averaged intensity of all pixels plays the role

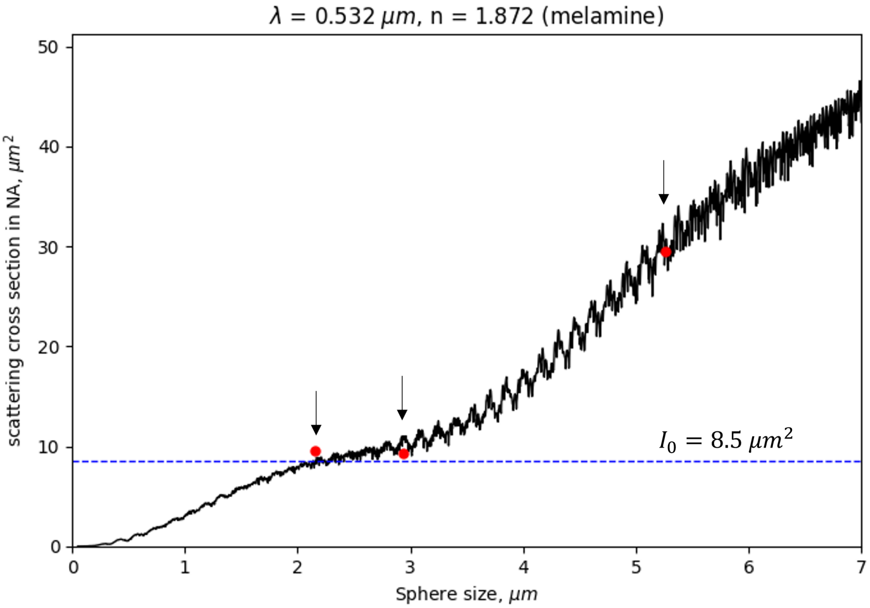

Figure 3.21: Calculated Mie scattering cross-sections (black line) for a single melamine ($n = 1.872$) particle, depending on the size. The red dots (pointed by black arrows) indicate the averaged TIS measurements divided by the number of detected 2.14, 2.94, and 5.26 μm melamine particles from Table 3.2. The Mie scattering cross-section was fitted using Equation 3.4.5 with the same constants. The blue dashed line indicates the fitted constant I_0, which is equal to 8.5 μm^2 and can be considered as the detection limit of this method.

of an analog signal and, therefore, is more reliable as it avoids any image processing other than thresholding for noise removal.

As mentioned, particles of several micrometers in size - as is the case here - obey the Mie scattering theory: the scattered intensity is proportional to the particle cross-section (or to r^2 of the particle, where r is the radius) and depends on multiple parameters such as n, k and D/λ, and the polarization of the incident and collected light [28]. For instance, melamine resins have $n = 1.872$, $k = 0$ (extinction coefficient is approximately zero for melamine-based materials in the visible range of wavelengths [29]), D/λ is equal to 4.0, 5.5, 9.9 (for 2.14, 2.94 and 5.26 μm particles respectively). The incident light in our experiments was polarised perpendicular to the plane made up of the incoming beam, the reflecting beam, and the camera. The reflected light was not measured but expected to remain unchanged for particles significantly exceeding the wavelength of the radiation. A change in one of these parameters can be diagnosed by the TIS signal approach.

The resolution limit of the TIS signal can be derived by matching it, again, with the Mie calculations for the given size, reflective index, and NA. The amount of scattering by a single particle was obtained by dividing the TIS sginal by the number of detected particles of fixed size (melamine samples in Table 3.2). The sizes of the particles were taken according to the values declared by the manufacturer. The results of this calibration (Figure 3.21) show a perfect match with the previously calibrated scattering cross-sections, which proves that imposed filtering, thresholding, and image processing used in the previous subsection do not contribute significantly to the uncertainty in size determination significantly. The true match is explained by testing monodisperse spheres with low standard deviation. When applying the TIS signal for polydisperse particles, the match will be worse. Therefore, it can be concluded that the resolution of the TIS measurements and the effective scattering cross-section of individual particles are the same.

3.4.7 Demonstration of the LLS setup on the predefined sample of silicon

Silicon particles were exposed to a series of external stress factors, such as flushing and plasma. The sequence of flushing-1 (10 min), plasma exposure (24 h), and flushing-2 (10 min) was applied to a wafer contaminated with Si particles. The flushing power was selected based on the median considerations. The flow must be strong enough to remove a noticeable amount of particles (exceeding the noise level of about 3% as obtained in the calibration section). Physically, this would imply that the flushing shear force and the average adhesion force are comparable. Flushing removes particles, while adhesion keeps them in place. If a particle remains on the substrate after flushing, the adhesion force is equal to or greater than the removal force. The flushing (using nitrogen gas) used in the sequence consisted of 3-second-long pulsed exhausts (6 nlm flow) at a frequency of 0.01 Hz (every 100 s). Each flushing campaign lasted 10 min. Between two flushing campaigns, the samples were exposed to the hydrogen ECR plasma with the parameters described before. The quantification of the results used the calibrations described in the previous section.

The top graph in Figure 3.22 shows the derived number of particles recorded over the experiment. The types of exposures (flushing or plasma) are mapped in different colors. Baselines (no exposures, only pressure changes) are shown in red, flushing campaigns are shown in green, and plasma exposure is shown in yellow. The plot shows that a significant amount of particles was flushed after the first few pulses. Further flushing appears to be ineffective, meaning that the remaining particles are attached with a force exceeding the applied shear force. The intermediate part of the experiment, during plasma exposure, clearly shows that the number of particles monotonically decays over the exposure, which indicates the effect of plasma exposure on the particles' adhesion. This effect is the quantification of the impact shown in the images captured with the camera (Figure 3.7). The bottom graph in Figure 3.22 shows the TIS signal, which mostly correlates with the top graph and confirms that the intensity drop correlates with the number of scattering centers. The more rapid decay of the TIS signal compared to that of the number of particles during the first hour of plasma exposure needs more investigation. However, hypothetically, this effect could be explained by the presence of a native oxide shell or an adsorbed water layer around the particles that have different n and k (i.e. lower scattering), where the oxide shell disappears after the first exposure to hydrogen plasma. After this phase, the scattering is proportional to the number of particles.

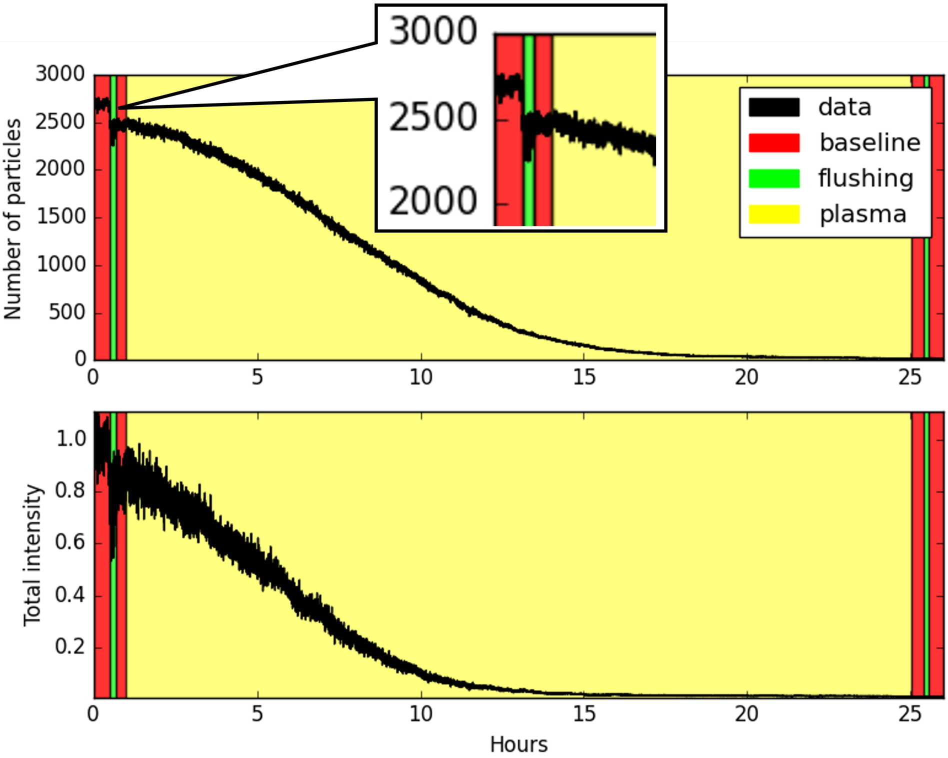

Figure 3.22: Calculated number of Si particles (on the top) and TIS signal (on the bottom) over time of exposure. Each dot is the average of 5 captured frames. particles are above the detection limit.

The interpretation of the gradual decrease of Si particles during plasma exposure can be the following. First, upon plasma impact, a particle may develop asperities across its surface, which reduces the effective vdW force, which, in turn, promotes the specific particles to be released [30]. An alternative could be the weakening of the interfacing (binding) atomic layers mechanism, e.g. removal by plasma of intermediate adsorbate layers or removal of water forming hydrogen bridges [12]. Another possible explanation could be the etching of the particles' material. The silane molecule SiH_4 is a formation product of sputtered Si atoms reacting with free hydrogen radicals, and it is volatile under our conditions. If the particles - due to this etching - shrink below the detection limit, they disappear from the sub-set of particles detected by the script, and the number of particles is reduced. The second flushing campaign was not necessary due to the lack of remaining particles. Overall, these measurements indicate that the particles with the adhesion force exceeding the shear force during the first flushing campaign became loose again due to plasma exposure.

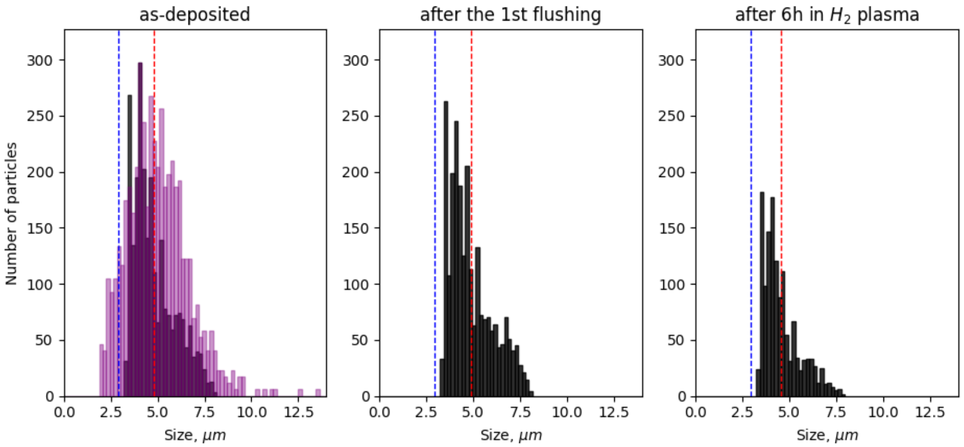

Figure 3.23: The black bins of the histograms indicate the number of Si particles measured by LLS after their deposition (on the left), after the first flushing campaign (in the middle), and after 6 h of exposure to hydrogen plasma (on the right). The purple bins indicate the size distribution of Si particles measured in SEM after their deposition. The red dashed line indicates the mean value of the black bins. The blue dashed line indicates the detection limit of LLS in our system.

The histograms in Figure 3.23 show the comparison of the size distributions of Si particles (black bins) after deposition (on the left), after the flushing (in the middle), and after 6 h of hydrogen plasma exposure (on the right). In addition, the size histogram obtained from SEM measurements on a similar (but not the same) sample with virgin Si particles (scanned over an area of 3 x 3 mm^2) is demonstrated on the left "as-deposited" in purple for comparison. The plotted particle size histograms obtained from the in-situ LLS measurements were obtained using the calibration method described above. The recorded intensities of Si particles were recalculated into sizes using the black curve from Figure 3.18 corresponding to silicon. The uncertainty of the method for these particles is the same as for melamine particles. The blue dashed line indicates the detection limit of the system, which depends on n. In fact, the detection limit is determined by the size at which the constant I_o intersects with the Mie calculation curve. For Si particles with $n = 4.15$, the detection limit is around 3 µm.

The histogram of as-deposited particles demonstrates the good matching of mean values in the calibrated LLS measurement results compared to size histograms obtained using SEM. The slight deviation in sizes is explained by the fact that SEM measurements were carried out for a similar sample with Si particles, but not the same (to prevent carbonization of particles in SEM and its influence on LLS measurements). It can also be seen from the plot that after the first flushing, a small fraction of the detected particles have been removed with no measurable difference in size distribution. Despite the fact that flushing scales as d^2 and adhesion should scale as d, we did not see the removal of bigger particles which can be addressed by the importance of other factors, such as size, shape, and roughness. As was mentioned before, this result indicates that the remaining particles have an adhesion force to the surface that exceeds the shear force exerted by the flushing. As is already shown in Figures 3.22 and 3.7, the number of particles decays over the duration of hydrogen plasma exposure, while the histograms in Figure 3.23 show that the particle size distribution has striven down and toward smaller sizes (together with the mean value shown as a red dotted line). As soon as a particle size reduces to the one indicated by the blue line (i.e. the detection limit), the particle disappears from the histogram, as it will not be detected anymore, and from the visibility of the script.

Therefore, the reliability of the recognition software has been tested based on 3 types of measurements:

1. The stability of the number of particle detections was demonstrated in Figure 3.15 for non-disturbed particles (without stressors like flushing or plasma) on a substrate.

2. The reliability of the obtained size distribution is shown in Figure 3.22, where the LLS measurements were compared to the SEM data (black bins versus purple bins).

3. The average scattering cross-section of a melamine particle using the TIS signal was compared to individually detected particles and demonstrated a good match in Figures 3.20 and 3.21. The TIS signal was treated as an analog signal for changing the scattering efficiency of particles.

The obtained size histograms indicate that the etching mechanism with shrinking particles beyond the detection limit is the dominant mechanism for Si particle interaction with hydrogen plasma. As can be seen from the middle and right histograms, the highest percentage reduction was for the largest particles, and the percentage gradually decreased toward the smallest particles. There are two reasons for that:

1. Bigger particles shrink and take the place of smaller particles (hence, a relatively constant amount of small particles remained unchanged).

2. Etching of Si by chemical sputtering of hydrogen radicals is only possible when accompanied by energetic electrons and ions from plasma breaking Si—Si bonds [31].

In that matter, the etching occurs at the place when particles interact with ions; hence, the particles are more likely to etch from the top rather than from the sides (it has also been demonstrated in AFM measurements [17]). It explains why the entire histogram does not strive toward the smaller side as a whole.

3.4.8 Summary of the calibration

The present study demonstrates the application of LLS, combined with long-distance microscopy, to in-situ characterize the response of micrometer-sized silicon particles on a smooth substrate to hydrogen plasma exposure or to a flushing gas jet. The number of particles, particle size distribution, and the TIS signal measured by LLS were calibrated with monodisperse melamine resin spheres. The results indicate that the counting accuracy was approximately 3% for 5.26 µm melamine spheres. Furthermore, the observed inconsistency in relating the counting of only the bright pixels to the particle size was attributed to the blooming effect. Therefore, the Mie theory was applied to convert the calibrated particle effective scatter cross-sections to the size equivalent. The accuracy of the LLS size measurement was found to be between 50% for 2.14 µm particles and 10% for 5.26 µm particles.

Surface-deposited Silicon particles were employed for LLS measurements in order to demonstrate the effectiveness of the method to serve as an in-situ diagnostic to visualize the effect of plasma exposure. The effect of plasma on Si particles is complex and may involve particle size and shape evolution due to chemical or physical sputtering. The in-situ measured counting and size evolution prove that the etching of Si is dominant when exposed to hydrogen plasma. The etching is mostly conducted by hydrogen ions. This is consistent with literature data obtained from SEM measurements. Additionally, SEM measurements conducted on virgin silicon particles demonstrated a high degree of concordance with the size distribution that was calculated using LLS and the Mie theory and subsequently plotted.

With this, we can conclude that LLS is a useful tool for in-situ measurement of plasma exposure or gas jet flushing, fragmenting, or etching of micrometer-sized particles with a statistical description of adhesion for multiple (100–1000s) particles exposed to the same stressor.

3.5 Morphology transformation of particles on a substrate exposed to plasma

3.5.1 Sample preparation and choice of materials

A substrate comprised a 500 µm-thick polished sapphire wafer with 100 nm chromium coating on one side. The particles acquired from SigmaAldrich™ and GoodFellow™ were dispersed over the chromium-coated side. A single type (size, material) of particles was used in every experiment. Clusters of particles were broken by contact actuation of the wafer edge with a sonic tip (Branson sonifier™, 10% intensity setting, 10 s total actuation time). The deposition method was described in Section 2.3.2. For this study, we selected a set of materials including stainless steel, Si, Sn, Pb, PbO, Ni, Zn, and CeO that are of interest for applications (f.i. relevant for EUV lithography). The properties of the selected materials are discussed below. All types of particles used in the experiments and their sizes are listed in Table 3.3.

The selected materials were chosen for several reasons. First, they may be utilized as materials within relevant plasma chambers or EUV scanners. Second, many of

Material	Size (µm)	Manufacturer	Gas
Sn	5	Aldrich	H_2
Si	5	USRN, Inc.	H_2
PbO	not defined	Aldrich	H_2
Pb	not defined	Aldrich	H_2
St. steel	5	USRN, Inc.	H_2
Zn	5	GoodFellow	H_2
Ni	2	Aldrich	H_2
CeO	5	USRN, Inc.	H_2
Sn	5	Aldrich	Ar
PbO	not defined	Aldrich	Ar

Table 3.3: The list of particles and their manufacturers used in the experiments. USRN is short for US Research Nanomaterials. The average sizes were taken according to the manufacturer.

these materials react with hydrogen: they have rather a high hydrogen permittivity or form hydrides. Some of these hydrides (like silane SiH_4) are relatively stable [32], while the others (like stannane SnH_4 and PbH_4) have a short lifetime [33, 34, 35] and may decompose on a surface before the detachment. One of the research lines was to follow the Si, Sn, and Pb sets of particles, which are in the same group in the periodic system with gradually changing bond properties from covalent to metallic.

The etching of Si in hydrogen and halogen-containing plasmas is widely known in semiconductor industry applications [31]. In another study, the authors used SEM and AFM mainly for bulk material showing that the polished silicon surface developed roughness after exposure to hydrogen plasma [17]. The results of Si etching in LLS were demonstrated in our previous work and were used as an illustration of the LLS method [36]. Here, we briefly repeat the results of those measurements.

Tin and zinc particles were chosen for the LLS study due to their relevance to EUV lithography. They can be emitted from the EUV source and settle on surfaces facing EUV-induced plasma. Prolonged exposure to EUV-induced plasma may result in adhesion loss, fragmentation, and ejection of particles [30]. In this study, Sn particles were exposed by ECR plasma to a flux of hydrogen radicals and ions more than 100x greater than typical EUV-induced plasma, which resulted in acceleration of relevant effects.

PbO particles contain Pb and O, both forming volatile hydrides (at different rates). Ni and stainless steel particles were chosen as a representative of a typical metal and as a construction material in an EUV scanner. Stainless steel particles were intended to be used as a reference due to the strong chromium oxide [37].

Finally, CeO represents ceramics, sometimes used in the polishing of components relevant to semiconductors.

3.5.2 Scheme of the experiment

In order to investigate the impact of plasma on particle adhesion to the surface, we implemented the following experimental scheme illustrated in Figure 3.24. The scheme was designed to demonstrate the effect of plasma on particles with an adhesion thresholded by shear flushing (removing weakly bound particles). The second flushing campaign after the plasma exposure was included to demonstrate the change in adhesion force by the plasma. The purpose of the second flushing was to determine whether plasma weakened the adhesion of the particles. If the adhesion was reduced by the plasma, the second flushing would remove extra particles.

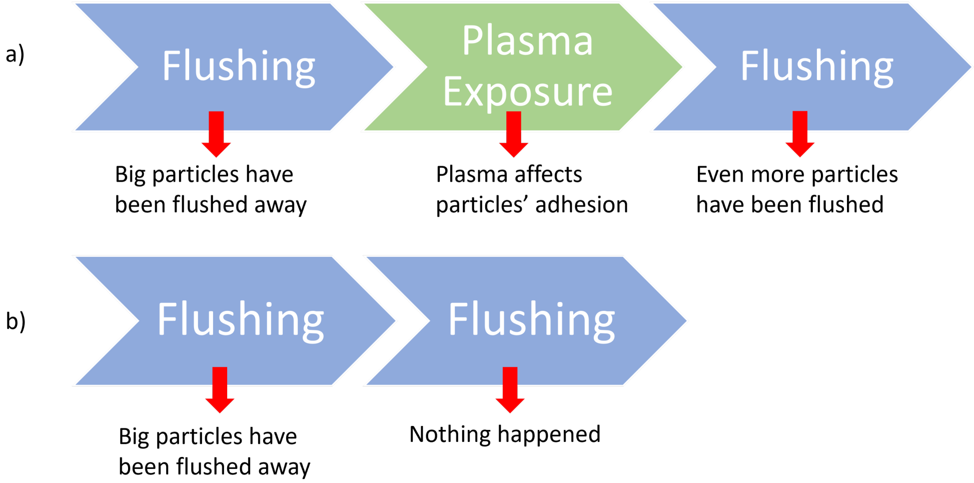

Figure 3.24: The following scheme was used in the experiments. The revealing of plasma effects by comparing acquired LLS data with (b) and without (a) applied plasma.

Before and after exposure to plasma. the samples with particles were inspected in SEM/FIB. We imaged the virgin particles on duplicate samples (particles after SEM were not used in LLS with plasma exposure or flushing, due to the possibility of enhanced adhesion by e-beam-induced carbon deposition). The pre- and post-exposure images allowed us to correlate the morphology and cross-section and their respective changes with the adhesion loss observed in LLS with plasma or flow shear. The SEM analysis helped to reveal a dominant mechanism of adhesion loss, primarily etching, formation of bubbles or cracking, and in extreme cases fragmentation of particles.

In addition, for comparison, some of the particles were exposed to argon plasma. By excluding the chemical influence of hydrogen radicals and ions, particles respond primarily to physical sputtering and surface charging. The results were demonstrated for Sn and PbO particles as representatives of rigid and soft materials respectively, at 50–200 W of input ECR RF power, maintaining all other conditions, including a flushing campaign similar to hydrogen exposures.

3.5.3 Results

Following sample preparation and placement, pumping to a high vacuum of the main chamber, establishing the flow, and laser preheating, a camera recording started. After a 30-minute baseline recording, the samples were subjected to the first flushing campaign. A few first pulses removed weakly attached and/or large particles since the removal force scales quadratic with size. The subsequent flushing pulses did not remove any more particles, indicating that the adhesion of the remaining particles exceeded the shear force of the flushing jet. Next, without interrupting the camera recording and after a 30-minute baseline, the samples were exposed to plasma for 24 h. Then, after a 30-minute baseline, the samples were exposed to the second flushing campaign, which had the same parameters as the first one. Finally, the exposure series concluded with a 30-minute baseline recording. The results were grouped into subsections by material type.

To visualize the impact of plasma on materials of the same group (Si, Sn, Pb), we extend the previously published SEM (Sn, Pb, and PbO) and LLS (Si) measurements and include them in this paper for convenience. In this study, we supplement the LLS data to demonstrate a comprehensive effect of the plasma on selected particles.

Stainless steel particles as baseline

Stainless steel, a widely utilized alloy in various industries, is known for its exceptional durability and resistance to corrosion [38, 39]. It is primarily composed of iron, along with significant amounts of chromium, nickel, and other alloying elements. The presence of chromium creates a passive oxide layer on the surface of stainless steel, which provides excellent protection against oxidation and prevents further corrosion. This oxide layer acts as a barrier, effectively shielding the underlying steel from detrimental environmental factors.

Moreover, the passive oxide layer on the stainless steel surface plays a crucial role in maintaining its integrity during hydrogen plasma exposure. This oxide layer acts as a diffusion barrier, limiting the permeation of hydrogen atoms into the metal matrix and minimizing the risk of hydrogen embrittlement. In our experiments, as seen from LLS measurements (Figure 3.25, top graph), particles from stainless steel were firmly held on the surface, and the number of remaining particles did not undergo visible changes. SEM measurements did not reveal surface changes as well (Figure 3.26). However, prolonged exposure to plasma significantly (and non-trivially) affects the reflectivity of stainless steel, leading to an increase in the TIS signal. The effect requires further investigation and can be associated with hydrogen-caused corrosion at long exposures [40].

The observed reaction of stainless steel to hydrogen plasma shows that it cannot be used as a baseline reference.

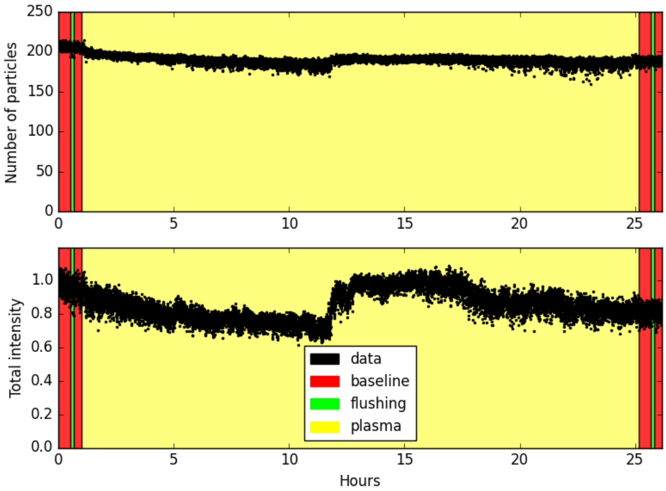

Figure 3.25: Counted number and TIS signal of stainless steel particles over time of exposure to hydrogen plasma and flushing jets obtained in LLS. Each dot is the average of 5 captured frames.

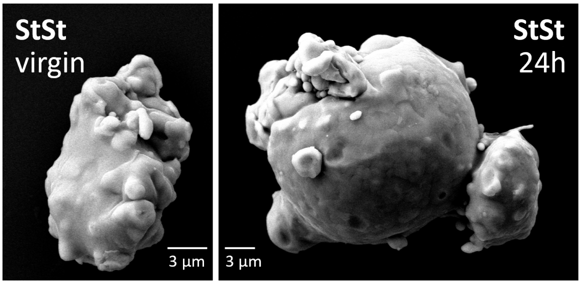

Figure 3.26: The comparison of SEM images taken for stainless steel particles after deposition (on the left) and after 24 h of exposure to hydrogen plasma (on the right).

Silicon particles

The graph (Figure 3.22, left graphs) shows that the number of Si particles and their total scattering from the substrate decrease simultaneously and monotonically as they are exposed to hydrogen plasma. Particle size diagrams before and after plasma exposure (Figure 3.23) indicate that the change in the number of particles is due to the etching of Si. The black bins indicate the size distributions measured by LLS after deposition (left), after the first flushing (middle), and after 24 h in hydrogen plasma (right). The purple bins indicate the size distribution measured in SEM on a similar (but not the same) sample with virgin particles.

Comparing the middle and right histograms in the previous section, we concluded that the distribution shifts down, so every particle shrinks. Particles below the detection limit of the setup do not contribute to the total particle number, reported by the script, which explains the downtrend in Figure 3.22. These results match the SEM observations shown in the literature [41, 42].

Tin particles

The SEM/FIB images illustrating changes in the surface and bulk of Sn and Pb micrometer-sized particles exposed to hydrogen plasma were reported earlier [30]. In the current work, the particles of the same material were used.

We demonstrated previously that Sn particles capture molecular hydrogen in bubbles beneath the surface (see Figure 3.28) in addition to etching. The effect saturates after a few hours of exposure and influences several factors related to adhesion: 1) the growth of bubbles near the substrate can reduce the contact spot and weaken the adhesion; 2) the etch/redeposition of Sn near the contact spot can increase the adhesion 3) the accumulation of multiple bubbles can lead to the formation of a crack and, in some cases, to explosive fragmentation. Consequently, the reduction in the number of Sn particles and the associated TIS signal in LLS are likely associated with the fragmentation (with resulting particles below the detection threshold) rather than with gradual etch, as observed in Si particles (Figure 3.27, right graphs). Note that the behavior of Sn particles is drastically different from Si particles. Reduction in Sn size becomes apparent when examining the last hours of exposure to hydrogen plasma. The signal becomes more scattered and noise increases, compared to the beginning of the exposure, indicating that more particles are approaching the detection limit.

The effect of Sn atom surface migration in hydrogen plasma was reported [30]. The effect manifested in the production of spikes and a change in the contact area to the substrate due to stannane generation and decomposition cycle.

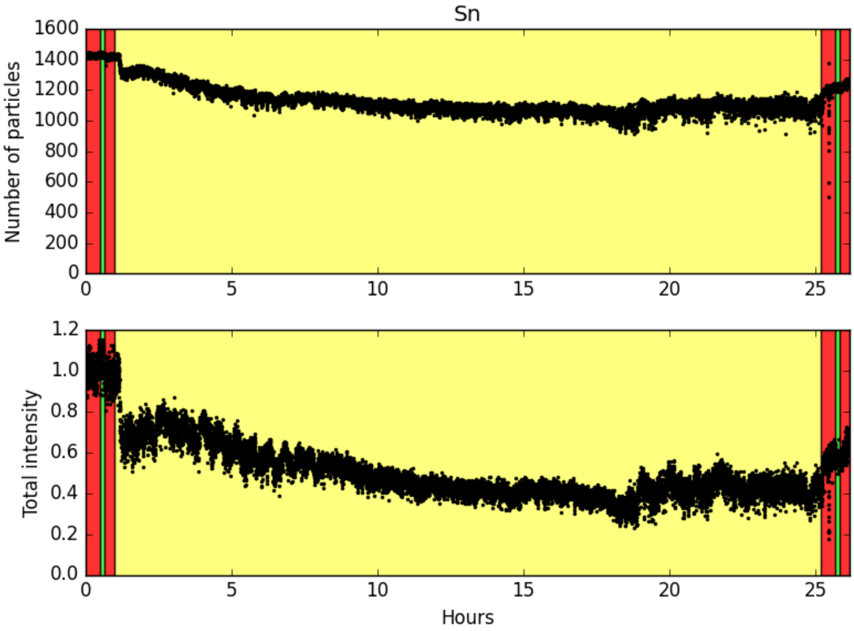

Figure 3.27: Counted number and TIS signal of Sn particles over time of exposure to hydrogen plasma and flushing jets obtained in LLS. Each dot is the average of 5 captured frames.

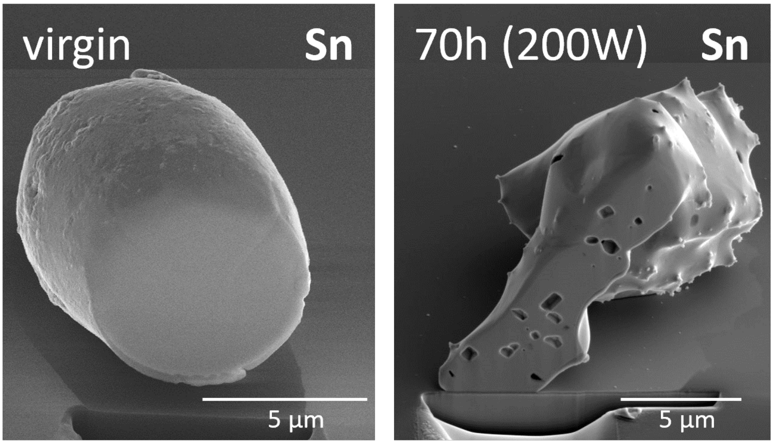

Figure 3.28: The comparison of SEM images taken for Sn particles after deposition (on the left) and after 24 h of exposure to hydrogen plasma (on the right).

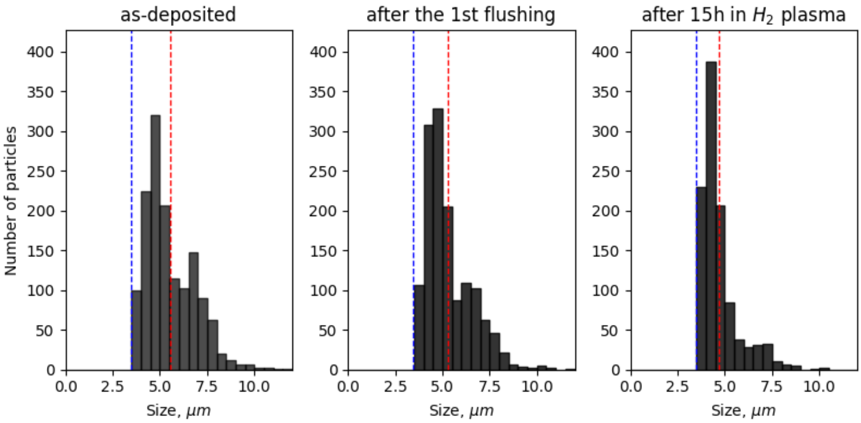

Figure 3.29: The black bins of the histograms indicate the number of Sn particles measured by LLS after their deposition (on the left), after the first flushing campaign (in the middle), and after 15 h of exposure to hydrogen plasma (on the right). The red dashed line indicates the mean value of the black bins. The blue dashed line indicates the detection limit of LLS in our system.

Figure 3.28 shows the result of both processes. The spikes can alter the scattering properties of the particles, which contribute to the downward trend for the total scattering observed in LLS: small features scatter light in large solid angles and thus reduce the photons collected within the NA of the long-distance microscope from the large particles. Additionally, surface migration of Sn atoms increased the adhesion for Sn after the long exposure. The plateau observed in the number of particles and the TIS signal after 15 h of exposure indicates that all remaining particles are securely attached to the surface, which is confirmed by the fact that the second flushing failed to remove any particles.

A size histogram of tin particles (Figure 3.29) was calculated for the deposited particles (left) after a flushing campaign (center) and after 15 h of exposure to a hydrogen plasma (right). Comparing the plots of as-deposited particles and after the first flushing campaign, the histograms indicate a loss of adhesion for large particles. After prolonged exposure to the plasma, the particles exhibited a reduction in size, as evidenced by the decrease in the tail of larger particles and a shift of the diagram toward the sensitivity threshold.

Lead and lead (II) oxide particles

Contrary to the Si or Sn particle behavior, Pb and PbO particles exhibited an opposite trend (Figure 3.30). The number of observable particles originally increased significantly at the start of the exposure, and this increase was directly proportional to the TIS signal. This can be attributed to fragmentation, where the fragment size exceeds the detection limit (Figure 3.31).

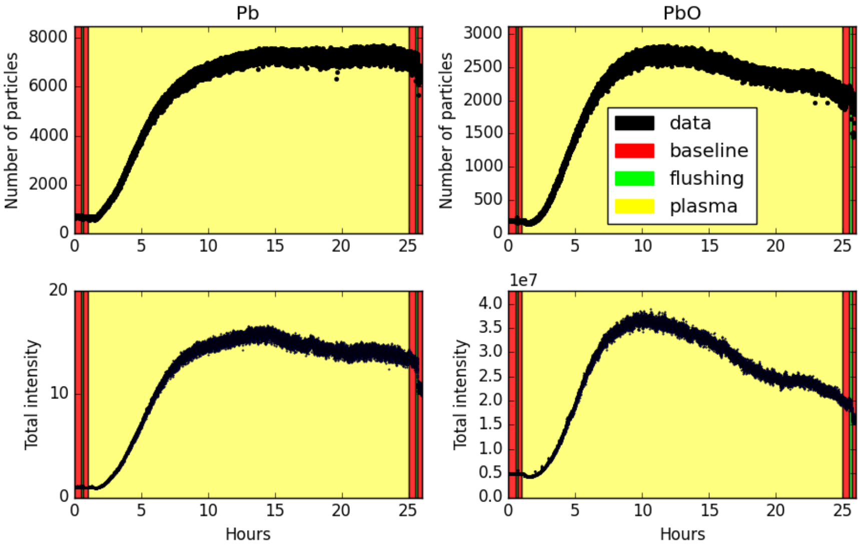

Figure 3.30: Detected number of particles and TIS signal of Pb particles (on the left) and PbO particles (on the right) over time of exposure to hydrogen plasma and flushing jets obtained in LLS. Each dot is the average of 5 captured frames.

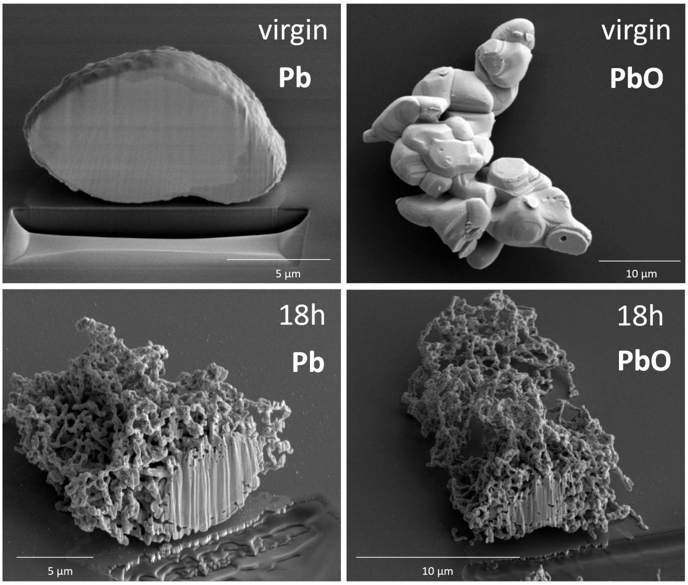

Figure 3.31: The comparison of SEM/FIB images taken for PbO (left) and Pb (right) particles after deposition and after 18 h of exposure to hydrogen plasma. Some images were copied from previous publications [43, 30].

We can compare reaction rates of Pb and PbO based on the trends in LLS, where reactions include fragmentation and etch. PbO particles respond more readily to hydrogen plasma, as evidenced by the LLS graphs comparison. The fragmentation occurred at a faster rate for PbO than for Pb, with fragments turning below the detection limit after about 10 h of exposure, which is reflected in the downward trend in the number of particles and the total intensity.

The stability of hydrides decreases in the sequence C–Si–Sn–Pb, as indicated by the increasingly negative values of the Gibbs energy. This signifies a decrease in the stability of the hydride molecules and a higher propensity for their decomposition. From left to right: 50.7, -46.2, -187.8, -485.0 respectively [30], which renders etching less important for Pb and PbO, compared to Si and possibly to Sn. The contact spot for exposed Pb and PbO particles post-etch is small, unlike exposed Sn, which may reflect the fast decomposition of plumbane that prevents the surface migration effects. The solubility of hydrogen increases in the row C–Si–Sn–Pb [44], and since Pb is mechanically weaker than Sn, the formation of bubbles and subsequent blistering is expected faster in Pb or PbO than in Sn. Lead has a higher number of dislocations or defects in the lattice (which is inversely proportional to the material's Ultimate Tensile Strength (UTS) [45]), which translates into more effective trapping of atomic hydrogen or greater concentration of nucleation centers, which means pressurized hydrogen bubbles are more prone in Pb or PbO to be trapped near the surface, compared to Sn and can be seen on FIB/SEM cross-sections.

All the effects combined may offer an explanation as to why Pb and PbO are so much more reactive with hydrogen plasma compared to other materials. Note the reduced adhesion for Pb and PbO particles remaining on the wafer after exposure, evident from the efficiency of the second flushing.

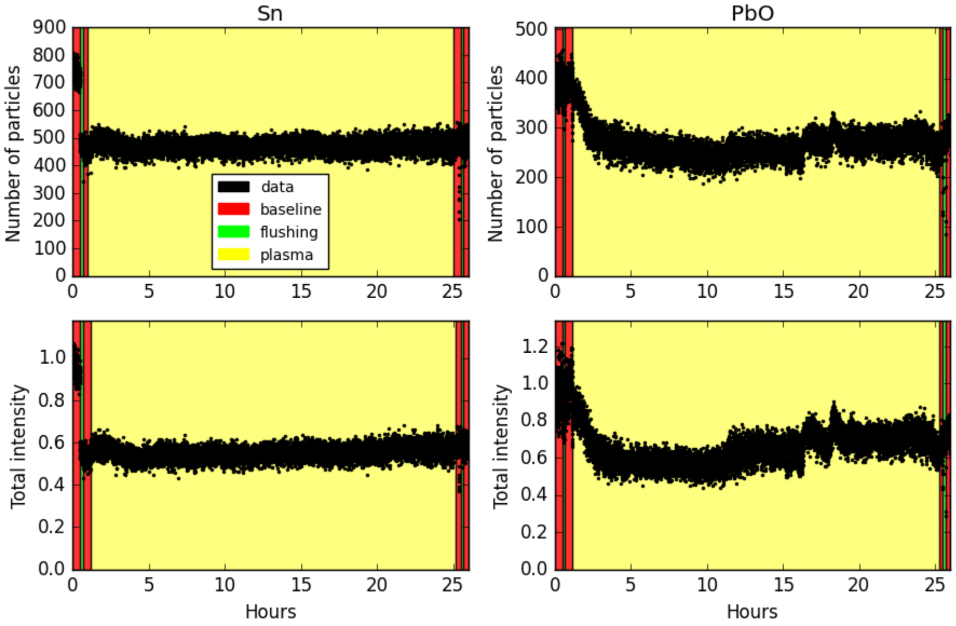

Figure 3.32: Counted number and TIS signal of Sn particles (on the left) and PbO particles (on the right) over time of exposure to argon plasma and flushing jets obtained in LLS. Each dot is the average of 5 captured frames.

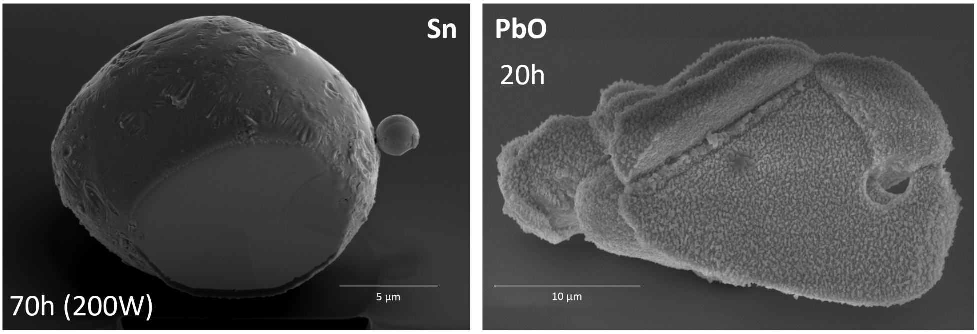

Figure 3.33: SEM images of Sn (left) and PbO (right) particles after 70 h (200 W) and 20 h (100 W) of exposure to argon plasma respectively.

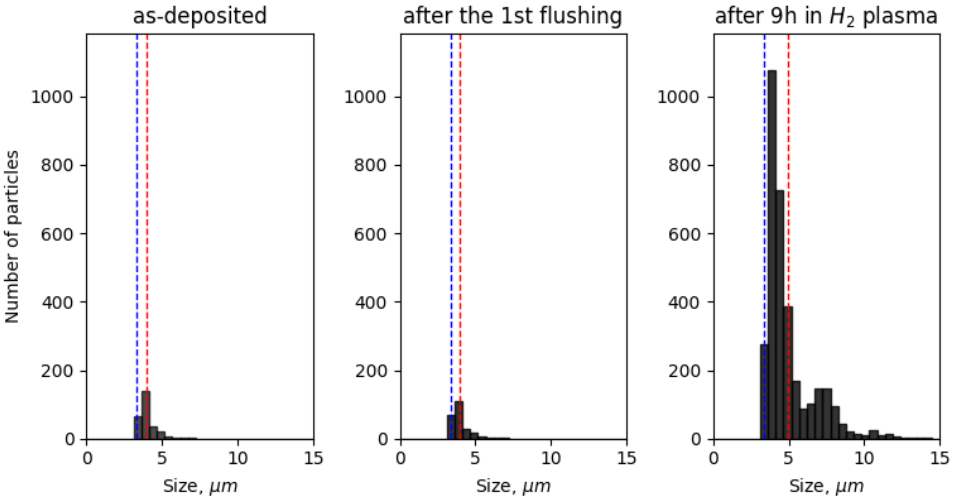

Figure 3.34: The histograms indicate the size distribution of Pb particles measured by LLS after their deposition (on the left), after the first flushing campaign (in the middle), and after 9 h of exposure to hydrogen plasma (on the right). The red dashed line indicates the mean value of the black bins. The blue dashed line indicates the detection limit of LLS in the experimental setup. The figure has been taken from our previous publication.

LLS signals for the exposures of Sn and PbO particles to argon plasma are presented in Figure 3.32. The SEM measurements of Sn and PbO particle exposures for 70 and 20 h, respectively, are shown in Figure 3.33. Visually, the observed changes in the morphology of Sn particles were limited to a modest roughening on the surface facing the plasma. This stands in contrast to hydrogen plasma exposures. The LLS measurements revealed that the introduction of surface roughness by Ar^+ sputtering or implantation far from the contact spot to the substrate did not impact the adhesion of Sn particles. The PbO particles exhibited significant adverse reactions. Blisters of approximately 50–100 nm in size covered the entire top surface of the particle. The particle became noticeably softer and melted when in the SEM electron beam. Consequently, it was not feasible to capture an image using FIB, as attempts to cut the particle with an ion beam resulted in severe damage. Argon ions from the plasma were able to penetrate the particle at a depth of a few tens of nanometers. Due to the concentration gradient of argon, with higher levels near the surface exposed to plasma and lower levels within the particle's bulk, argon atoms diffused slowly into the volume, causing mechanical stress within the crystal lattice and introducing disorder as seen in Figure 3.33 (on the right).

The LLS measurements of PbO particles exposed to argon plasma revealed downtrends in the number of particles and the total intensity during the initial 4 h of exposure. The increased roughness (evident in Figure 3.33, right graph) can alter the scattering properties (n, k, or a shape) of the particles to the extent that the

NA of the long-distance microscope captures less light and the number of particles detected drops.

The measured size distribution of Pb particles (Figure 3.34) reveals that fragmentation occurs through the flaking of the outer shell on the surface rather than through the division of big particles into chunks, which supports the observations in SEM (Figure 3.33). The clustering of these delaminated flakes leads to an average increase in detectable particle size, as seen by the camera. The observed fragmentation continues until the dimensions of the newly formed flakes are below the detection limit of the script.

Zinc particles

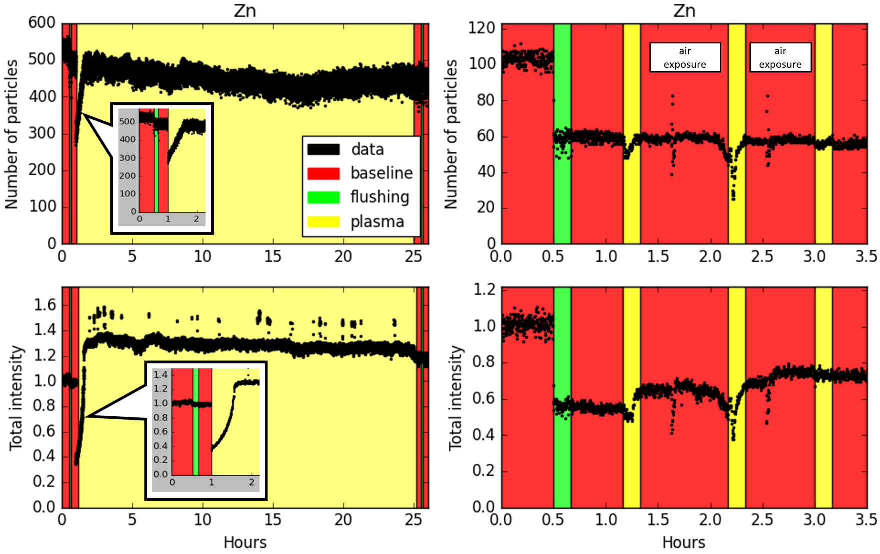

Figure 3.35: Counted number and TIS signal of Zn particles (on the left) and a sequence of 10-minute-long exposures to hydrogen plasma (on the right) and flushing jets obtained in LLS. Each dot is the average of 5 captured frames.

Zinc particles' response to hydrogen plasma is open for interpretation (Figure 3.35, left graphs). After flushing out weakly adhering particles and stabilizing the baseline upon plasma activation, the number of observed particles and the scattered radiation signal instantly dropped by more than 50%. In the next few minutes the number of particles recovered to the initial value (linearly with time), and the total scattering even exceeded the initial value (quadratic with time). The recovery of the signals tool was about 40 min and cannot be explained by optical constants changing. The effect of plasma exposure on the surface of Zn was further investigated using SEM. Figure 3.36 shows the same Zn particle before plasma exposure (left figure) and after a 100-minute-long exposure to hydrogen plasma (right figure). The polishing of the surface is clearly visible and may be detected by LLS.

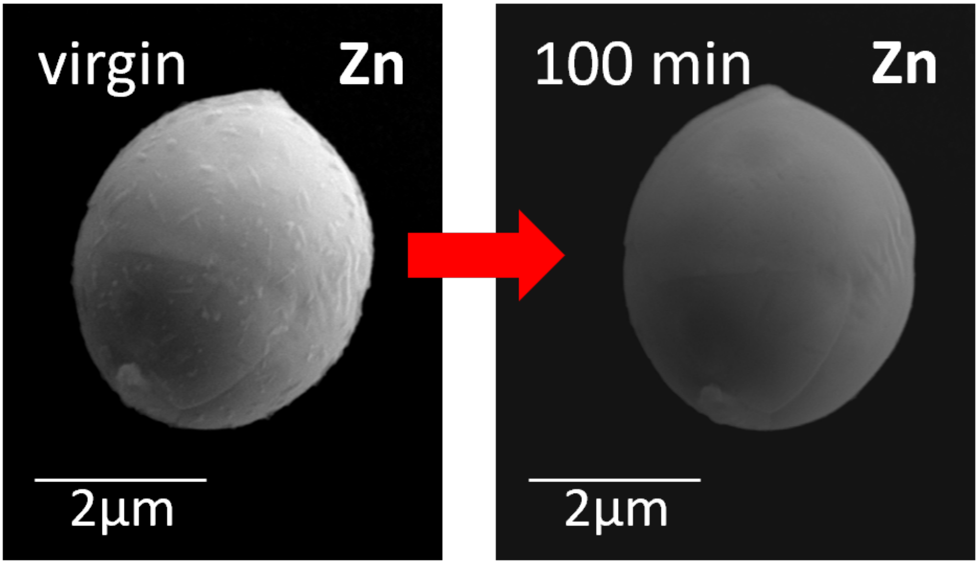

Figure 3.36: The comparison of SEM/FIB images taken for the same Zn particle after deposition (left) and after 100 min of exposure to hydrogen plasma (right).

In order to visualize the effect of plasma influence on optical constants and shape, a series of plasma exposures were conducted which were interrupted by periods at which particles were held in a forevacuum (Figure 3.35, right), and the oxide shell has recovered at least partially. Every exposure took 10 minutes and was selected to ensure the removal of the oxide shell, with the minimum effect on the particles' surface roughness. Polishing is an accumulative effect, as can be seen from the trending up TIS signal during exposures. After the third exposure, the polishing effect became insignificant, and the plasma exposure did not alter the number of detected particles or the TIS signal. The surges in the number of particles and the TIS signal after 1.5 and 2.5 h may be explained by a phase transformation of the growing oxide. ZnO exists in two crystalline forms: wurtzite and zincblende [46]. There may be a change in n, k if the growing oxide recrystallizes from one form to another (subject to changing stress). Note, the TIS signal spike is negative, while the detected number of particles spike is first positive, then negative, which indicates the particles on the edge of the detection range (with a small contribution to the TIS signal) drive this behavior.

Nickel particles

Nickel particle response to hydrogen plasma is not fully understood (Figure 3.37). Rises and falls in the number of detected particles and correlating the TIS signal suggest several competing processes, such as changes in the n and k values due to the reduction of oxide or formation of a hydride, similar to the case of Zn. The overall trend is a reduction in the number of detected particles with exposure, but since it correlates well with the TIS signal it may be seen as the gradual reduction of average particle size as well. Furthermore, Ni particles are the smallest in the studied set of materials, with a significant portion near the detection limit (∼ 2 µm) of the LLS system. The large dispersion in particle number or TIS signal around the average shot-to-shot may reflect the fact that small variations in laser power translate into large variations in the number of particles detected. A moderate/small effect of the first flushing on the number of particles is primarily due to the small size, the lack of efficiency of the second flushing implies the adhesion of particles remained unperturbed by the plasma exposure.

SEM images taken before and after the exposure (Figure 3.38) revealed that Ni particles consisted of multiple weakly bonded grains, so we can relate gradual particle size reduction with fragmentation at the boundary between grains with produced fragments below the detection limit of the building block. As we do not expect chemical or physical sputtering in hydrogen plasma or sublimation, as observed with Zn particles.

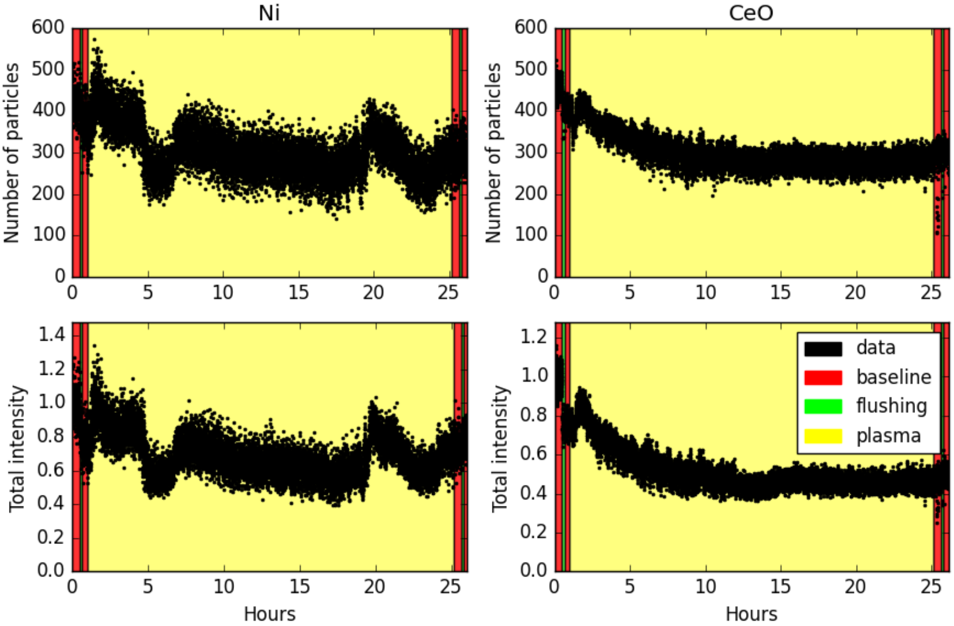

Figure 3.37: Counted number and TIS signal of Ni particle (on the left) and CeO particles (on the right) over time of exposure to hydrogen plasma and flushing jets obtained in LLS. Each dot is the average of 5 captured frames.

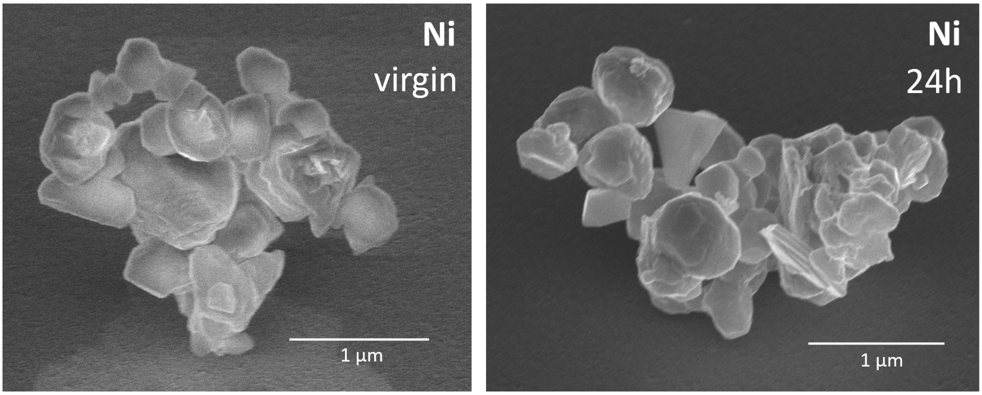

Figure 3.38: The comparison of SEM images taken for Ni particles after deposition (on the left) and after 24 h of exposure to hydrogen plasma (on the right).

Cerium (II) oxide particles

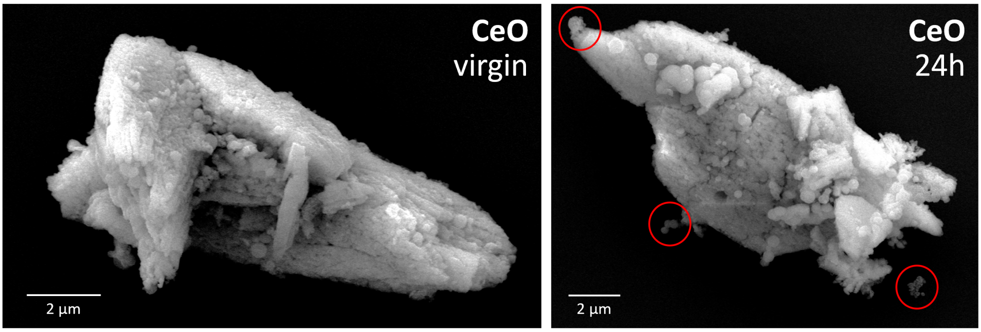

Figure 3.39: The comparison of SEM images taken for CeO particles after deposition (on the left) and after 24 h of exposure to hydrogen plasma (on the right). Red circles indicate the appeared fragments.

A moderate effect of the first flushing on the number of particles and total intensity is observed (Figure 3.37, right). The initial increase in the number of particles and intensity during exposure is likely associated with changes in the n, k upon partial reduction (CeO $\rightarrow$ Ce), similar to the cases of Ni and Zn. The subsequent drop in particle number and total intensity and plateauing after 9 h indicates saturation in this effect or production of hydrides (CeH_2 or CeH_3) affecting the n, k or partial fragmentation of CeO clustered particles, similar to Ni, with fragment size below the detection limit. The lack of efficiency of the second flush implies the stability of particles near the contact spot with the substrate. This is in line with expectation since the Ce—O bond is comparable to the Cr—O bond in the passivation layer of the stainless steel [47].

SEM images of CeO particles did not reveal any significant difference in the morphology of the particle before and after the exposure. However, the particles after exposure exhibited the fracture of small edge fragments of the particle and their deposition nearby on the substrate, indicated by red circles (Figure 3.39). The most likely explanation is associated with material embrittlement during oxygen extraction and Ce reduction.

3.6 Discussion

The effects of hydrogen and argon plasmas as well as the effect of a directed gas jet on particles of several micrometers deposited on a reflective substrate were investigated using LLS accompanied by long-distance microscopy and SEM/FIB pre- and post-inspection. LLS enabled simultaneous in-situ monitoring of hundreds of particles during plasma exposures or jet shear and allowed to study the sensitivity of different materials to these stressors statistically. The obtained LLS graphs reflected a wide range of behaviors of particles in argon and hydrogen plasmas, including etching, fragmentation, and detachments of particles, as well as a change in the optical constants n and k for the particle's outer shell. The correlated SEM/FIB measurements confirmed the shape transformation: appearing asperities and/or the increased smoothness, surface diffusion, and precipitation of pressurized bubbles in the bulk.

First of all, as expected, hydrogen plasma did not affect the adhesion change of stainless steel particles. However, stainless steel particles undergo a minor change in reflectivity over time. The effect could be related to partial oxide removal but requires further investigation.

The impact of physical sputtering on Sn (rigid) and PbO (soft) particles exposed to noble (argon) plasma was investigated using LLS and SEM/FIB. In this case, any changes in morphology may occur only through the physical displacement of atoms. The findings revealed that the top surface of Sn particles suffered minor damage, which did not significantly affect the observed trends in adhesion loss or change in optical properties. In contrast, PbO particles experienced severe damage due to the bombardment of Ar^+ ions. These impinging ions induced surface blistering and caused the particles to soften. Although the Pb—O bond (378 kJ/mol) [47] is slightly stronger than the Pb—Pb bond (339 kJ/mol) [47], the extraction of O is more likely due to the favorable momentum transfer in a collision between O and Ar atoms. The maximum momentum transfer from the ECR hydrogen plasma used in this study to Sn atoms is approximately 10% (mostly for the hydrogen ion H_3^+) [12], while the momentum transfer to the lighter O atoms in PbO is already 53%, indicating a relatively low activation barrier. This suggests that during exposure, the surface oxide layer of Sn particles may convert into a partial oxide. Based on these observations, it can be concluded that subjecting soft materials like PbO to argon plasma has the potential to lead to the formation of a nano/micro gel-like structure, which might be interesting for catalyst applications.

The rest of the experiments were devoted to demonstrating the evident effects of the interaction of hydrogen plasma with particles. We were able to relate the trends in etching rate and the adhesion of the remaining particles within the group (Si $>$ Sn $>$ Pb, PbO) and fragmentation (Si $<$ Sn $<$ Pb, PbO) in hydrogen plasma. The bubbling mechanism is still possible in silicon [48, 49] or aluminum [50] but requires hydrogen implantation with much higher energies $\sim$ 1000 eV. The etching rate of polycrystalline Si in hydrogen plasma was reported around 70 nm/min [51], while the etching of Sn is only about 10 nm/min [52], which correlates with our LLS measurements. The difference in reactivity between Pb and PbO can, in part, be attributed to the relative ease of water formation compared to plumbane, with respective free Gibbs energy values of -229 kJ/mol [53] and -321 kJ/mol [30]. The tendency toward a plateau in the LLS graphs, when Sn particles were exposed to hydrogen plasma, is more likely associated with the surface diffusion of Sn hydride molecules and their dissociation and deposition near the area of contact of the particle with the surface, which consequently increases the vdW force. In view of (that mechanism), the firmly attached Sn particles can be dragged only by the cracking mechanism (through the set of bubbles) or by gradual etching.

We observed the smoothening of Zn particles in hydrogen plasma. The instant drop in both signals is likely related to the change of optical constants n and k for the system Zn and ZnO shell, which is 20-60 nm thick [54]. Bulk Zn has $n = 0.88$ and $k = 4.8$, and ZnO has $n = 2.03$ (measured at the wavelength of 532 nm).[55, 7] The significant difference in optical constants explains the drop after the ignition of plasma which illuminates 60 nm oxide within minutes. Furthermore, the vapor pressure of Zn is significantly higher ($\sim 10^{-6}$ Pa) compared to other selected metals, such as Pb with a value of $\sim 10^{-11}$ Pa and Ni with a value of $\sim 10^{-14}$ Pa at 400 K, as determined by linear approximation of the curves obtained from Honig's research [56]. When exposed to plasma, Zn exhibits a tendency to evaporate in a vacuum [57]. The surface asperities of Zn appear to evaporate at a faster rate, resulting in a smoother surface, which is detectable by LLS. Indeed, once the oxide layer is reduced, the sharp features sublimate first. According to the Mie theory, as discussed earlier, particles larger than a few micrometers scatter light predominantly forward (toward the microscope NA), while sub-micrometer particles scatter light at a solid angle of 4π. In the case of a rough particle, surface irregularities can act as individual sources of scattering at 4π. Therefore, a smooth particle scatters more light forward than a rough particle of similar size. The LLS total intensity signal recovery during plasma and post-plasma exposure stability may be explained by particles becoming and staying smoother. Additionally, the common hydride of Zn (ZnH_2) is spatial polar. Due to the induced electric field, these hydrides have a weak mutual attractive force, which contributes to surface diffusion. This phenomenon is further supported by the observed tipping point in adhesion, as depicted in the LLS graphs. Furthermore, we saw a similar trend in n, k, and cross-section for forward-light scattering for metallic particles with native oxide (like Zn) and ceramic particles with bulk oxide (like CeO) that are partially reduced in hydrogen plasma. It has been concluded that the change in n, k optical properties is accumulative and shape-dependent, based on the periodic exposures of Zn to hydrogen plasma.

Clustered particles with moderate response to hydrogen plasma (Ni, CeO) are open for interpretation; breaking fragments smaller than the detection limit is a possible explanation of LLS signals.

3.7 Chapter conclusion

In this chapter, we demonstrated the use of LLS (laser light scattering) in combination with long-distance microscopy as an in-situ tool for observing micro-particles subjected to various stressors such as flushing and plasma. The detected number of particles, the TIS signal, and evaluation of their size distribution in LLS were calibrated using melamine particles of known sizes. It was demonstrated that the use of the Mie theory is necessary for particle size determination.

Using the calibrated setup, Si, Sn, Pb, PbO, Ni, Zn, CeO, and stainless steel particles were investigated under hydrogen and argon plasma conditions as well as under a gas jet. It was shown that changes in the scattering properties of particles and the decrease/increase in the observed number of particles are associated with alterations in their morphology, as confirmed by SEM/FIB measurements or with the adhesion loss of particles.

The observed effects in the plasma can be grouped as follows:

1. Etching of particles, with a gradual disappearance as they approach the sensitivity threshold of the optics. This effect is characterized by a monotonic decrease in the visible number of particles and the TIS signal. This effect was observed for Si, Sn, CeO, and Zn.

2. Particle fragmentation. In this case, exemplified by Pb and PbO, the number of particles appeared to increase due to the generation of flakes and particle chunks. Furthermore, significant surface damage and structural loss lead to the loss of adhesion, which was demonstrated by subsequent flushing.

3. Changes in the optical constants n and k of particles can occur, either due to the removal of the oxide film from the particles as demonstrated in the cyclic experiment with Zn particles, with Sn, Ni, and CeO particles, or due to potential surface layer hydrogenation. These changes are often manifested by abrupt variations in the scattering signals upon plasma ignition.

4. Physical sputtering of particles. This was observed when particles were exposed to argon plasma. While particle detachment is not excluded, the most likely explanation for the observed particle count is due to changes in the scattering properties of the surface layer of particles perpendicular to the trajectory of argon ions. Sn, due to its resilience, did not show significant changes in SEM, while argon ion implantation into soft PbO led to its swelling and transformation into a gel-like structure.

5. Some effects require further investigation and cannot be easily interpreted. F.i., stainless steel or Ni particles.

3.8 Bibliography

[1] T.A. Germer. Polarized light scattering techniques for surface wafer inspection. In *2000 Digest of the LEOS Summer Topical Meetings. Electronic-Enhanced Optics. Optical Sensing in Semiconductor Manufacturing. Electro-Optics in Space. Broadband Optical Networks*. IEEE, 2000.

[2] Haruyuki Inoue et al. Inspection of ultra fine particles on the si wafer surface using a laser light scattering method. *Journal of the Japan Society for Precision Engineering*, 68(2):264–268, 2002.

[3] Juan de Dios Ortiz-Alvarado. Analysis of masking effect on laser light scattering from unidirectional and isotropic machined surfaces. *Superficies y Vacío*, 23:6, 06 2010.

[4] Suk-Ho Hong and Jorg Winter. Size dependence of optical properties and internal structure of plasma grown carbonaceous nanoparticles studied by in situ rayleigh-mie scattering ellipsometry. *Journal of Applied Physics*, 100(6):064303, September 2006.

[5] W. J. Wiscombe. Improved mie scattering algorithms. *Appl. Opt.*, 19(9):1505–1509, May 1980.

[6] Max Born, Emil Wolf, A B Bhatia, P C Clemmow, D Gabor, A R Stokes, A M Taylor, P A Wayman, and W L Wilcock. The calculus of variations. In *Principles of Optics*, pages 853–872. Cambridge University Press, Cambridge, 2013.

[7] Wolfgang S. M. Werner, Kathrin Glantschnig, and Claudia Ambrosch-Draxl. Optical constants and inelastic electron-scattering data for 17 elemental metals. *Journal of Physical and Chemical Reference Data*, 38(4):1013–1092, December 2009.

[8] Golovashkin A. I. and Motulevich G. P. Optical and electrical properties of tin. *Soviet Physics JETP*, 19(2):460, August 1964.

[9] M van de Kerkhof et al. Understanding EUV-induced plasma and application to particle contamination control in EUV scanners. In Nelson M. Felix and Anna Lio, editors, *Extreme Ultraviolet (EUV) Lithography XI*. SPIE, March 2020.

[10] T. H. M. van de Ven, P. Reefman, C. A. de Meijere, R. M. van der Horst, M. van Kampen, V. Y. Banine, and J. Beckers. Ion energy distributions in highly transient EUV induced plasma in hydrogen. *Journal of Applied Physics*, 123(6), February 2018.

[11] R. Kirchheim and A. Pundt. Hydrogen in metals. In *Physical Metallurgy*. Elsevier, 2014.

[12] Mark A. van de Kerkhof, Ernst Galutschek, Andrei Yakunin, Selwyn Cats, and Christian Cloin. Particulate and molecular contamination control in EUV-induced

h2-plasma in EUV lithographic scanner. In Carlos E. Soares, Eve M. Wooldridge, and Bruce A. Matheson, editors, *Systems Contamination: Prediction, Control, and Performance 2020*. SPIE, August 2020.

[13] Kouun Shirai, Takashi Iizuka, and Shun ichi Gonda. Electric probe measurements in an ECR plasma CVD apparatus. *Japanese Journal of Applied Physics*, 28:897–902, May 1989.

[14] Miran Mozetič, Matija Drobnič, and Anton Zalar. Recombination of neutral hydrogen atoms on AISI 304 stainless steel surface. *Applied Surface Science*, 144-145:399–403, April 1999.

[15] Isaac Mendez, F Gordillo-Vazquez, V Herrero, and I. Tanarro. Atom and ion chemistry in low pressure hydrogen dc plasmas. *The journal of physical chemistry. A*, 110, May 2006.

[16] P. Dutta, S. Paul, D. Galipeau, and V. Bommisetty. Effect of hydrogen plasma treatment on the surface morphology, microstructure and electronic transport properties of nc-sih. *Thin Solid Films*, 518(23):6811–6817, September 2010.

[17] Stephan Altmannshofer, Ignaz Eisele, and Alexander Gschwandtner. Hydrogen microwave plasma treatment of si and SiO2. *Surface and Coatings Technology*, 304:359–363, October 2016.

[18] EverGreen pulser 532 nm laser datasheet. `https://www.quantel-laser.com/tl_files/client/docs_produits/EverGreen2_Specs_062021REVB.pdf`. Accessed: 2023-06-07.

[19] Air flow rate calculator through an orifice. `https://www.tlv.com/global/TI/calculator/air-flow-rate-through-orifice.html`. Accessed: 2023-06-07.

[20] K L Mittal and Ravi Jaiswal. *Particle adhesion and removal*. Adhesion and Adhesives: Fundamental and Applied Aspects. John Wiley & Sons, Nashville, TN, January 2015.

[21] P. Virtanen et al. Scipy 1.0: fundamental algorithms for scientific computing in python. *Nature Methods*, 17(3):261–272, February 2020.

[22] Yingchao Meng, Zhongping Zhang, Huaqiang Yin, and Tao Ma. Automatic detection of particle size distribution by image analysis based on local adaptive canny edge detection and modified circular hough transform. *Micron*, 106:34–41, March 2018.

[23] Adam S Hughes. pyparty: Intuitive particle processing in python. *Journal of Open Research Software*, 2(1):26, September 2014.

[24] Stephen G Lipson, Henry Lipson, and David Stefan Tannhauser. Preface to the third edition. In *Optical Physics*, pages xiii–xiv. Cambridge University Press, Cambridge, July 1995.

[25] Jean-Marc Belloir, Jean-Baptiste Lincelles, Alice Pelamatti, Clementine Durnez, Vincent Goiffon, Cedric Virmontois, Philippe Paillet, Pierre Magnan, and Olivier Gilardx. Dark current blooming in pinned photodiode CMOS image sensors. *IEEE Transactions on Electron Devices*, 64(3):1161–1166, March 2017.

[26] Hamatsu blooming effect. `http://hamamatsu.magnet.fsu.edu/articles/ccdsatandblooming.html`. Accessed: 2023-07-19.

[27] Helmuth Horvath. Gustav mie and the scattering and absorption of light by particles: Historic developments and basics. *Journal of Quantitative Spectroscopy and Radiative Transfer*, 110(11):787–799, July 2009.

[28] Warren Wiscombe. Mie scattering calculations: Advances in technique and fast, vector-speed computer codes. Technical report, 1979.

[29] S. Kalyanaraman, S. Vijayalakshmi, M. Kanagavalli, M. Kalaselvi, S. Maheswari, and P. Kirthika. Optical properties of melamine based materials. *Optik*, 125(22):6634–6636, November 2014.

[30] D Shefer, Andrey Nikipelov, Mark Kerkhof, Zahra Marvi, Vadim Y Banine, and J Beckers. The impact of hydrogen plasma on the structure and morphology of tin and lead micrometer sized particles. *Journal of Physics D: Applied Physics*, January 2023.

[31] A. Aßmuth, T. Stimpel-Lindner, O. Senftleben, A. Bayerstadler, T. Sulima, H. Baumgärtner, and I. Eisele. The role of atomic hydrogen in pre-epitaxial silicon substrate cleaning. *Applied Surface Science*, 253(20):8389–8393, August 2007.

[32] Seiichiro Koda. Kinetic aspects of oxidation and combustion of silane and related compounds. *Progress in Energy and Combustion Science*, 18(6):513–528, 1992.

[33] Thomas A. Hein, Walter Thiel, and Timothy J. Lee. Ab initio study of the stability and vibrational spectra of plumbane, methylplumbane, and homologous compounds. *The Journal of Physical Chemistry*, 97(17):4381–4385, Apr 1993.

[34] Xuefeng Wang and Lester Andrews. Infrared spectra of group 14 hydrides in solid hydrogen: Experimental observation of pbh4, pb2h2, and pb2h4. *Journal of the American Chemical Society*, 125(21):6581–6587, May 2003.

[35] Patryk Zaleski-Ejgierd, Roald Hoffmann, and N. W. Ashcroft. High pressure stabilization and emergent forms of pbh4. *Physical Review Letters*, 107(3), July 2011.

[36] D Shefer, A Nikipelov, M van de Kerkhof, V Banine, and J Beckers. Laser light scattering (LLS) to observe plasma impact on the adhesion of micrometer-sized particles to a surface. *Journal of Physics D: Applied Physics*, 56(45):455201, August 2023.

[37] V. Nemanič, J. Kovač, M. Žumer, and J. Zavašnik. Impact of surface oxide on hydrogen permeability of chromium membranes. *International Journal of Hydrogen Energy*, 48(26):9723–9733, March 2023.

[38] Hiroshi Uemasu, Masashi Takenaka, Tetsuya Shimizu, Masami Abe, Toshifumi Hirasaki, and Hidenori Hamada. Corrosion resistance of stainless steels under marine environments. *DENKI-SEIKO*, 75(2):133–138, 2004.

[39] A.J. Sedriks and O.S. Zaroog. Corrosion of stainless steels. In *Reference Module in Materials Science and Materials Engineering*. Elsevier, 2017.

[40] Gunnar Hultquist, C. Anghel, and P. Szakalos. Effects of hydrogen on the corrosion resistance of metallic materials and semiconductors. *Materials Science Forum*, 522-523:139–146, August 2006.

[41] R. P. H. Chang, C. C. Chang, and S. Darack. Hydrogen plasma etching of semiconductors and their oxides. *Journal of Vacuum Science and Technology*, 20(1):45–50, 1982.

[42] Sergej Alexandrovich Filonovich, Hugo Aguas, Tito Busani, Antonio Vicente, Andreia Araujo, Diana Gaspar, Marcia Vilarigues, Joaquim Leitao, Elvira Fortunato, and Rodrigo Martins. Hydrogen plasma treatment of very thin p-type nanocrystalline si films grown by rf-pecvd in the presence of $b(ch_3)_3$. *Science and Technology of Advanced Materials*, 13(4):045004, August 2012.

[43] Dmitry Shefer, Andrey Nikipelov, Mark van de Kerkhof, Vadim Banine, and Job Beckers. Morphology change and release of tin and lead micro-particles from substrates in hydrogen plasma. In Nelson M. Felix and Anna Lio, editors, *Extreme Ultraviolet (EUV) Lithography XII*, volume 11609, pages 116 – 123. International Society for Optics and Photonics, SPIE, 2021.

[44] Robert Hull. Properties of crystalline silicon. 1999.

[45] Brian Lawn. *Fracture of Brittle Solids*. Cambridge University Press, June 1993.

[46] J.L.G. Fierro, editor. *Metal Oxides*. CRC Press, August 2005.

[47] E. Lippert. The strengths of chemical bonds, von t. l. cottrell. butterworths publications ltd., london 1958. 2. aufl., x, 317 s., geb.t—/32/—. *Angewandte Chemie*, 72(16):602–602, August 1960.

[48] Paul K. Chu and Xuchu Zeng. Hydrogen-induced surface blistering of sample chuck materials in hydrogen plasma immersion ion implantation. *Journal of Vacuum Science & Technology A: Vacuum, Surfaces, and Films*, 19(5):2301–2306, September 2001.

[49] C. Coupeau, E. Dion, M.-L. David, J. Colin, and J. Grilhé. Effect of pressure and stress on blistering induced by hydrogen implantation in silicon. *EPL (Europhysics Letters)*, 92(1):16001, October 2010.

[50] De-Gang Xie et al. In situ study of the initiation of hydrogen bubbles at the aluminium metal/oxide interface. *Nature Materials*, 14:899–903, 9 2015.

[51] Aomar Hadjadj, Fadila Larbi, Mickaël Gilliot, and Pere Cabarrocas. Etching of a-si:h thin films by hydrogen plasma: A view from in situ spectroscopic ellipsometry. *The Journal of chemical physics*, 141:084708, 08 2014.

[52] Daniel Elg, Gianluca Panici, Jason Peck, Shailendra Srivastava, and David Ruzic. Modeling and measurement of hydrogen radical densities of in situ plasma-based sn cleaning source. *Journal of Micro/Nanolithography, MEMS, and MOEMS*, 16:023–501, 04 2017.

[53] John Rumble, editor. *CRC handbook of chemistry and physics.* CRC Handbook of Chemistry and Physics. CRC Press, London, England, 101 edition, July 2020.

[54] Divine Khan Ngwashi, Thomas Attia Mih, and Richard B M Cross. The influence of ZnO layer thickness on the performance and electrical bias stress instability in ZnO thin film transistors. *Materials Research Express*, 7(2):026302, February 2020.

[55] Walter L. Bond. Measurement of the refractive indices of several crystals. *Journal of Applied Physics*, 36:1674–1677, 1965.

[56] R.E. Honig and Radio Corporation of America. RCA Labratories Division. *Vapor Pressure Data for the More Common Elements.* David Sarnoff Research Center, 1957.

[57] Jafar Safarian and Thorvald A. Engh. Vacuum evaporation of pure metals. *Metallurgical and Materials Transactions A*, 44(2):747–753, October 2012.

Chapter 4

Hydrogen plasma-assisted allotrope transformation of tin

Preface.

Tin (Sn) is allotropic, and two of its phases (α and β) exist at pressures and temperatures similar to the conditions in EUV scanners. Exposure of Sn to hydrogen plasma leads to the formation of bubbles in the bulk, the pressure within which exceeds the ultimate tensile strength (UTS) of the material. The tension around such bubbles is capable of transforming metallic β-Sn to semiconductor α-Sn at elevated temperatures, significantly exceeding 13.2 °C (transition point at normal pressure), based on extrapolation of tin PT-phase diagram up to the UTS value. Crystalline, spherical β-Sn particles with sizes varied in a range of 1–100 µm were exposed to Electron Cyclotron Resonance (ECR) hydrogen plasma at different ion doses and substrate temperatures. SEM measurements confirmed Sn sensitivity to substrate temperature. In the range of temperatures between 13.2 and 50 °C Sn particles fragmented via a cracking mechanism, which may correspond to the presence of brittle α-Sn. However, the direct measurements using XRD, TEM, and electron diffraction did not confirm another phase in the exposed samples, stored in the air for days after the exposure, which may indicate the importance of outgassing. At temperatures above 80 °C, the inflated bubbles deformed the particles plastically, which corresponds to the remaining metallicity of white Sn and is normally expected. We also anticipate the impact of tension on solid/liquid phase transition. Though the behavior of solid Sn in a hydrogen plasma environment near the melting temperature was not covered in this work, this future research topic might be of interest for industrial applications.

4.1 Introduction

Tin (Sn) is a prevalent material extensively utilized in electronic devices and systems. For example, in an EUV source, laser-produced plasmas (LPP) are generated by focusing a laser beam on tin droplets that pass in a stream directly in front of a large light-collecting mirror (collector). LPP generation is accompanied by the impact of Sn debris on the collector mirror and adjacent surfaces, resulting in the accumulation of Sn contamination [1]. Additionally, during the emission of EUV radiation, small liquid Sn droplets may travel through the scanner toward EUV multilayer optics and the reticle [2]. Existing strategies for mitigating debris, which rely on the flow of hydrogen gas in the LPP source, are only partially effective due to the low-pressure environment required for EUV transmission [3]. When EUV radiation is absorbed in this low-pressure environment and an EUV-induced plasma is created due to photoionization events, hydrogen radicals are generated, which can chemically transform the thin Sn deposits on the mirror into volatile SnH_4 molecules [4]. These volatile molecules are then pumped away, resulting in a self-cleaning effect, as long as the rate of Sn deposition on the optical surface is not excessively high. Moreover, in-situ cleaning methods that utilize a hydrogen radical source have been proposed for removing Sn layers with thicknesses up to a few micrometers [5].

Upon impact with a surface, liquid Sn droplets instantly solidify. Such particles exhibit a larger contact area with the surface due to spreading. Therefore, the deposited Sn debris is subjected to long-term exposure to EUV-induced hydrogen plasma. Ion flux toward the particles and the governing ion energy distribution function both strongly depend on the distance from the beam. The flux of ions may range between 0.1 and 20 A/m^2 (between EUV afterglow and concentrated plasma near intermediate focuses of the beam [6]) and mostly at a temperature of a few eV. It has been demonstrated in Section 2 that long exposure of Sn particles to hydrogen plasma significantly alters their morphology. Ejection of Sn fragments under stress due to hydrogen uptake is of serious concern.

Tin is allotropic, which means that it has different crystal structures depending on the temperature and pressure conditions. Tin has four known allotrope phases [7]. Two of these phases (referred to as α-Sn and β-Sn) are stable at temperatures and pressures typical for exposures in a scanner and in our experiments with ECR hydrogen plasma (P = 5 Pa, T $\cong$ 50 °C): 1) the β-phase, a metal, known as white Sn, with a tetragonal lattice and a density of 7.31 g/cm^3, and 2) the α-phase, a semiconductor, known as gray Sn, with a cubic lattice and a density of 5.77 g/cm^3 [8]. The transition temperature between these two phases at normal conditions is 13.2 °C. When cooled down and held below the equilibrium temperature of the transition point, β-Sn can spontaneously transform into the semiconductor phase α-Sn. The transformation involves volume expansion due to a change of crystal structure (around 27%) [9, 10]. The α-Sn product, referred to as "tin pest" [8], is structurally weak, readily crumbles, and converts shiny Sn objects into black powder.

Tin pest was utilized in an attempt to clean EUV mirrors from contaminated Sn debris [12]. The thick β-Sn debris was intentionally converted to brittle α-Sn for a short time in order to increase the effectiveness of other removal techniques (e.g.

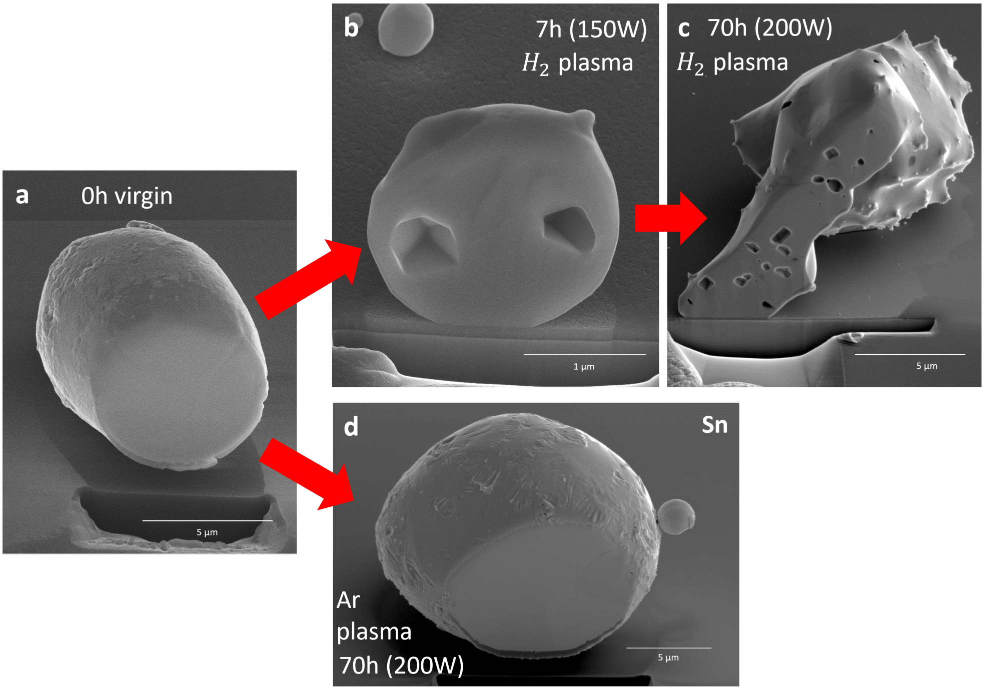

Figure 4.1: Tin particles prior to plasma exposure (a), after 7 h, 70 h of exposure to hydrogen plasma (b and c, respectively), and after 70 h of exposure to argon plasma (d). The aspherical shape of bubbles in Sn is indicative of the tensor nature of yield strength or at least the anisotropy of yield strength in the crystalline material [11].

gaseous flushing or frozen-particle flows) [13]. Conversion to the gray phase lowers the adhesion of the embrittled droplet to the surface and causes easier detachment. The development of the gray phase will lead to fragmentation of the entire particle. The benefit of phase conversion for cleaning has a flip side: phase conversion over time may result in cracks in the Sn particles and disintegration, thereby increasing surface area and promoting contamination.

In Chapters 2 and 3 the effect of hydrogen plasma on the composition and morphology of Sn particles (among other materials) was studied utilizing SEM and LLS. As suggested, morphology changes included not only roughness changes due to the effects due to effects of etching (SnH_4 generation) and redeposition (SnH_4 dissociation), but also the incorporation of bubbles. Hydrogen molecule H_2 diffusion is slower in the bulk than radical H^* diffusion because of the bigger occupied volume (the vdW radius of H_2 is 119 pm [14], and the size of a hydrogen atom is 53 pm). The dissolved atomic hydrogen becomes trapped within the bulk due to recombination into molecular hydrogen at the boundaries of existing inner bubbles or crystal defects. The process is similar to the origin of rising bubbles during the boiling of water.

The pressure in the formed bubbles apparently exceeds the ultimate tensile strength (UTS) of the given material (220 MPa for bulk Sn [15]) since the bubbles emerge and then grow with increasing dose of hydrogen ions or radicals (Figure 4.1b and 4.1c). It was reported that pressure inside such bubbles can be very high even at small hydrogen concentrations [16]. The tension comparable to the UTS may affect the allotrope transformation as the same effect was reported to be introduced by the change in pressure and is clearly seen in the PT-phase diagram of Sn [17]. Thus a bubble generates significant stress in a crystal, predominantly as a result of tangential stretching.. It is important to pay particular attention to the shape of these bubbles. During plastic deformation, macroscopic metal pieces deform symmetrically, averaging over multiple grain domains and orientations. For microscopic particles exposed to hydrogen plasma, FIB/SEM images show bubbles with distinct edges and facets exhibiting a crystalline orientation. This effect depicts the tensor nature of tin's yield strength, which, apparently, preserves despite the high concentration of dissolved atomic and molecular hydrogen in plasma. There was no such effect for Sn particles exposed to plasma from the noble gas argon (Figure 4.1d), or for the materials after hydrogen physical implantation, such as tungsten (W) in ITER fusion (Figure 4.2). Such bubbles are generally round and do not have a preference in direction. High energy ion implantation generates disorder in the lattice and averages the properties of crystals in different directions [11]. Also note that during hydrogen/deuterium implantation, bubbles lie close to the surface, while under the diffusion mechanism of inflation, bubbles may appear deep in the bulk.

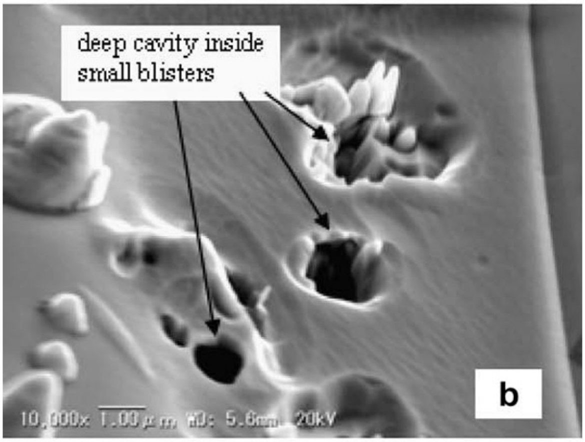

Figure 4.2: The indication of the bubble shape in blistered tungsten when exposed to deuterium plasma at 10^{22} D^+/m^2 and energy of 38 eV [18].

In summary, Sn is allotropic, and two of its phases exist at pressures and temperatures similar to the conditions in EUV scanners. Exposure of Sn to hydrogen plasma leads to the formation of bubbles, the pressure within which exceeds the ultimate tensile strength (UTS) of the material. The conversion of white Sn to gray Sn in the region around the bubbles depends on the temperature and tension, which, in turn, depends on atomic hydrogen influx and relaxation of material, or interaction with the stress from neighboring bubbles. The effect of liquid Sn droplet emission, when exposed to hydrogen plasma or hydrogen radical flux, is known from EUV lithography [2] and from ITER fusion [19]. However, the hypothetical effect of solid Sn particulate emission requires investigation. The objective of this chapter is to experimentally demonstrate the influence of hydrogen plasma on the fragmentation of tin particles at different temperatures, as well as to suggest a phase transformation mechanism that explains the observations.

4.2 Experiment

The exposure of tin particles in the reticle region of the scanner is a relatively weak and slow process. The power of the incident EUV radiation on the EUV reticle is approximately 50 W (for a 250 W EUV source) [20]. The ion flux is on the order of 5 mA/m^2 (as hydrogen with pressure about 10 Pa near a reticle absorbs in order of 1% of EUV light per meter with about 3 ions H_3^+ produced per absorbed photon) [21]. In shaded areas without direct EUV irradiation, the plasma concentration is even lower. Under such conditions, accumulating sufficient stress in the particles requires a prolonged period of time (in terms of critical ion dose). Additionally, outgassing further slows down the process. Consequently, based on the literature's contribution to contamination [20], such events are rare and challenging to study. In our experimental conditions, the ion concentration exceeds that in the scanner by 100–1000 times, which allows for a proportional reduction of experimental time by a factor of 1000. We assume that the inter-exchange of time and ion concentration is correct.

The flux of ions in EUV-induced plasma near the EUV source at the exit of the intermediate focus (IF) is approximately 20 A/m^2, which closely matches the parameters of our experiments. Therefore, our results can directly translate to the effects occurring with Sn in that particular environment.

We anticipate the fragmentation of solid Sn to be dependent on temperature and radical/ion flux based on the following indicators:

1. Sn demonstrates high hydrogen solubility, leading to active bubble formation within the material.
2. Sensitivity of hydrogen solubility to temperature, in an endothermic reaction.
3. Sensitivity of atomic hydrogen diffusion, including diffusion through lattice defects and imperfections due to temperature.
4. Tin allotrope phases depend on temperature.

Such sensitivity can be practically utilized to optimize the performance of an EUV source or EUV scanner, particularly when operating within a suitable temperature range (not cryogenic or exceeding 100 °C, thus compatible with water cooling).

The next experimental parts consist of the following subsections:

1. Section 4.2.1: Sample Preparation. In this subsection, the preparation of samples for the experiments is discussed, including the specific techniques and procedures employed.
2. Section 4.2.2: Experimental Setup. In this subsection, the upgraded setup used for the experiments is elaborated on. It includes a detailed description of the apparatus, instruments, and parameters employed to conduct the experiments.
3. Section 4.2.3: Experimental sequence. The plan of exposures and evaluation methods are discussed.
4. Section 4.3: Results. This subsection presents a comprehensive description and analysis of the experimental results obtained. It includes data, figures, and any relevant observations or findings resulting from the conducted experiments.

In conclusion, in order to study the potential conversion of white Sn to gray Sn under hydrogen plasma conditions, an experiment with control over transition temperature (below and above 13 °C) and high ion flux is required.

4.2.1 Sample preparation

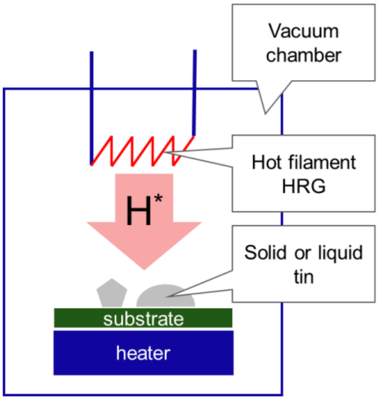

Figure 4.3: Schematic drawing of Sn deposition setup. A substrate, containing solid Sn particles, was exposed to a radical flux (10^{13} cm^{-2}), generated by a hydrogen radical generator (HRG). The temperature of the substrate was maintained at a temperature above > 600 °C. The emitted Sn droplets were collected on another wafer.

We used the same substrates as described in Sections 2 and 3 but with differently prepared particles. In order to replicate conditions inside the scanner more accurately, Sn particles were deposited onto the substrate not in the form of powder but as liquid droplets. The deposition setup was based on the known effect of liquid Sn emission when exposed to hydrogen radicals [22]. The hydrogen radical generator

(HRG) provided a flux of radicals to a heated substrate with liquid tin. The generator is schematically depicted in Figure 4.3. The emitted particles were collected on another wafer that faced the substrate. The deposited particles took the shape of semi-spherical droplets with a large flat contact area with the surface, resulting in high adhesion. Upon contact with the wafer surface, the particles rapidly solidified and formed a single crystal.

The deposited particles were spherical, 1–100 µm in diameter, and comprised only white Sn. One important consequence of this method is that Sn particles remained in the hydrogen radical atmosphere for an extended period of time. As was discussed above, dissolved hydrogen accumulates in the form of bubbles. Therefore, even without plasma exposure, the deposited particles contained bubbles. These bubbles do not contain pressurized hydrogen for long after the particle deposition due to relatively high outgassing after turning off the plasma (diffusion of hydrogen atoms in Sn is high, see Chapter 2).

Upon exposure to open air, Sn undergoes oxidation, leading to the formation of tin oxide (SnO) and tin dioxide (SnO_2). These natural oxide layers act as self-limiting barriers, inhibiting further oxidation of the tin surface. The thickness of the native oxide layer is typically limited to approximately 10 nm [23].

4.2.2 Experimental setup

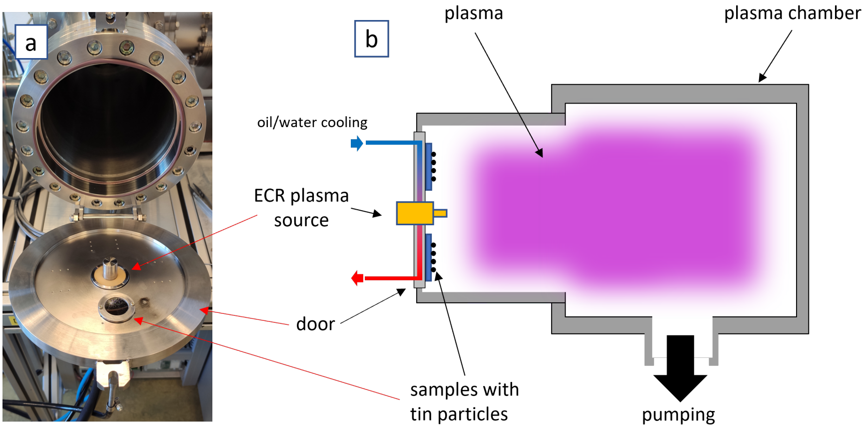

Figure 4.4: The setup, used in the experiments for the expositions of Sn to hydrogen plasma with temperature control. a) Photo of the setup b) Schematic drawing.

For the experiments, the setup that was described in Chapter 2 (Figure 2.3) was modified. The flange with the plasma source was extended and replaced with the O-ring-sealed stainless steel door. The ECR source with wafers was mounted in the center of the door. Schematically, the setup is depicted in Figure 4.4. The distance of the wafer from the ECR antenna was about 3 cm. A graphite gasket of about 100 µm-thick was used between the substrates and the metal surface of the door and ensured the uniform heating of the particles. Samples were temperature conditioned by the holder/vacuum flange, with integrated water cooling/heating channels. Water temperature was controlled within a range of ±1 °C during exposures by a ThermoFisher bath circulator AC200.

The temperature of the samples was tested by running both plasma and the chiller using deposited gallium (Ga) grains. Gallium is a low-melting metal with a melting point of 29.9 °C [24]. If gallium granules had melted, they would have indicated that the melting temperature had been exceeded. The offset between water temperature and sample temperature was found to be 10 °C. The difference can be addressed by the thermal losses at the stainless steel-carbon gasket-sapphire wafer interfaces at a power density of 1 W/cm^2.

The RF generator supplied 200 W of power. The ECR plasma source provided hydrogen with an ion flux of 20 A/m^2 to the sample location, which was estimated using the absolute amorphous carbon etch rate. During that etch the thickness of the carbon films was measured before and after the exposure to plasma. Knowing the average carbon removal yield of 0.2 per incident ion [25], the ion flux was assessed. All other parameters remained equal to the previous experiments.

4.2.3 Experimental sequence

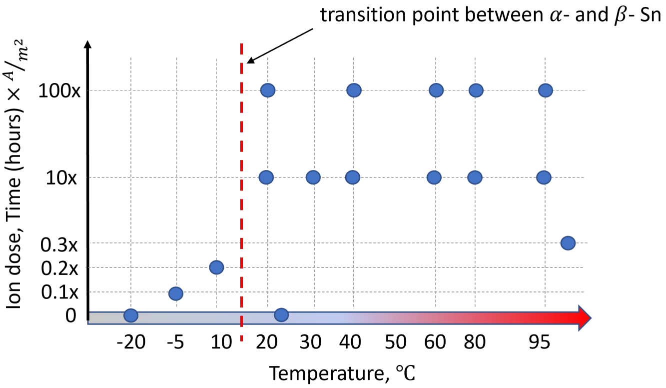

Figure 4.5: The exposure scheme of Sn particles to hydrogen plasma depending on the ion dose and temperature including 2 virgin samples at -20 °C (after the freezer) and -20 °C (not exposed) as baselines. The symbol x along the y-axis is the proportion coefficient, which is equal to 20 A/m^2. Gray and white Sn are in equilibrium at 13 °C and normal pressure.

To study the effect of hydrogen plasma on allotrope phase transformation and Sn fragmentation, the following experimental sequence was conducted. The samples, prepared as described above were exposed to plasma at various temperatures. As previously demonstrated, the closer the temperature is to the phase transition point, the lower the accumulated stress in the bubbles is required for phase conversion to be initiated. The samples exposed to a high ion flux of 20 A/m^2 were split into 2 groups in terms of the time of exposure (which could be treated as exposure dose): short (10 h), and long (100 h) exposures at temperatures varying from 20 to 95 °C. In addition, one virgin sample kept at room temperature served as a baseline for white Sn. Another sample kept in a freezer at -20 °C for 1 week served as a baseline for gray Sn. Finally, two samples were exposed to plasma below the transition point at a temperature of -5 and 10 °C for 12 and 35 h, respectively, with a low ion flux of 1 A/m^2 (the plasma conditions were similar to those described in Section 2. The exposure doses and temperatures are depicted in Figure 4.5. The parameter x determines the proportion coefficient between exposure time and the ion flux and equals 20 A/m^2.

For all samples, the SEM/FIB measurements were conducted using the same parameters as described in the previous chapters. In total, there were 16 samples analyzed (including 2 baseline samples).

4.3 Results

Allotrope transformation of Sn particles

The results of SEM/FIB measurements are presented in Figure 4.6 and 4.7. First and foremost, attention should be drawn to the appearance of the baseline samples. For white Sn, the baseline samples already exhibit dissolved bubbles, as indicated in Section 4.2.1, which is attributed to the particle deposition method. The bubbles have irregular shapes, indicating the anisotropic nature of their growth. Tin particles without plasma show flat facets on the surface, indicating their single-crystalline nature.

Notably, particles with prominent fractures or cracks should be highlighted (Figure 4.6 c, d, e, f, and Figure 4.7 a, b). Fracturing in the form of cracks is not characteristic of ductile metallic Sn. Fractures likely occur along brittle planes of gray Sn, which form around the bubbles. Since originally Sn is a single crystal, the growth of gray Sn is expected to be single-crystalline as well. Although there may be multiple nucleation centers for gray Sn (around multiple bubbles), their orientations should be parallel. Hence, cracks propagate in the most brittle directions.

Such a crack can act as a stress initiator. Initially, it develops within the confinement of a single bubble. The crack tip adds tensile stress, prompting the white Sn at its end to convert to gray Sn, resulting in crack growth. When the crack connects multiple bubbles, the particle may delaminate and fragmentation may occur, leading to a brittle fracture. For instance, in Figure 4.7b, the rightmost image demonstrates the detachment of a Sn layer, likely following the same mechanism.

№	Ion dose	Temperature, °C	RF power, W	Exposure time, hours	SEM figure
1	virgin	23	-	-	Figure 4.6a
2	virgin	-20	-	-	Figure 4.6b
3	0.1x	-5	100	12	Figure 4.8a
4	0.2x	10	100	35	Figure 4.8b
5	0.3x	100	100	60	Figure 4.9
6	10x	20	200	10	Figure 4.6c
7	10x	30	200	10	Figure 4.6d
8	10x	40	200	10	Figure 4.6e
9	10x	60	200	10	Figure 4.6f
10	10x	80	200	10	Figure 4.6g
11	10x	95	200	10	Figure 4.6h
12	100x	20	200	100	Figure 4.7a
13	100x	40	200	100	Figure 4.7b
14	100x	60	200	100	Figure 4.7c
15	100x	80	200	100	Figure 4.7d
16	100x	95	200	100	Figure 4.7e

Table 4.1: The list of particles and exposure parameters.

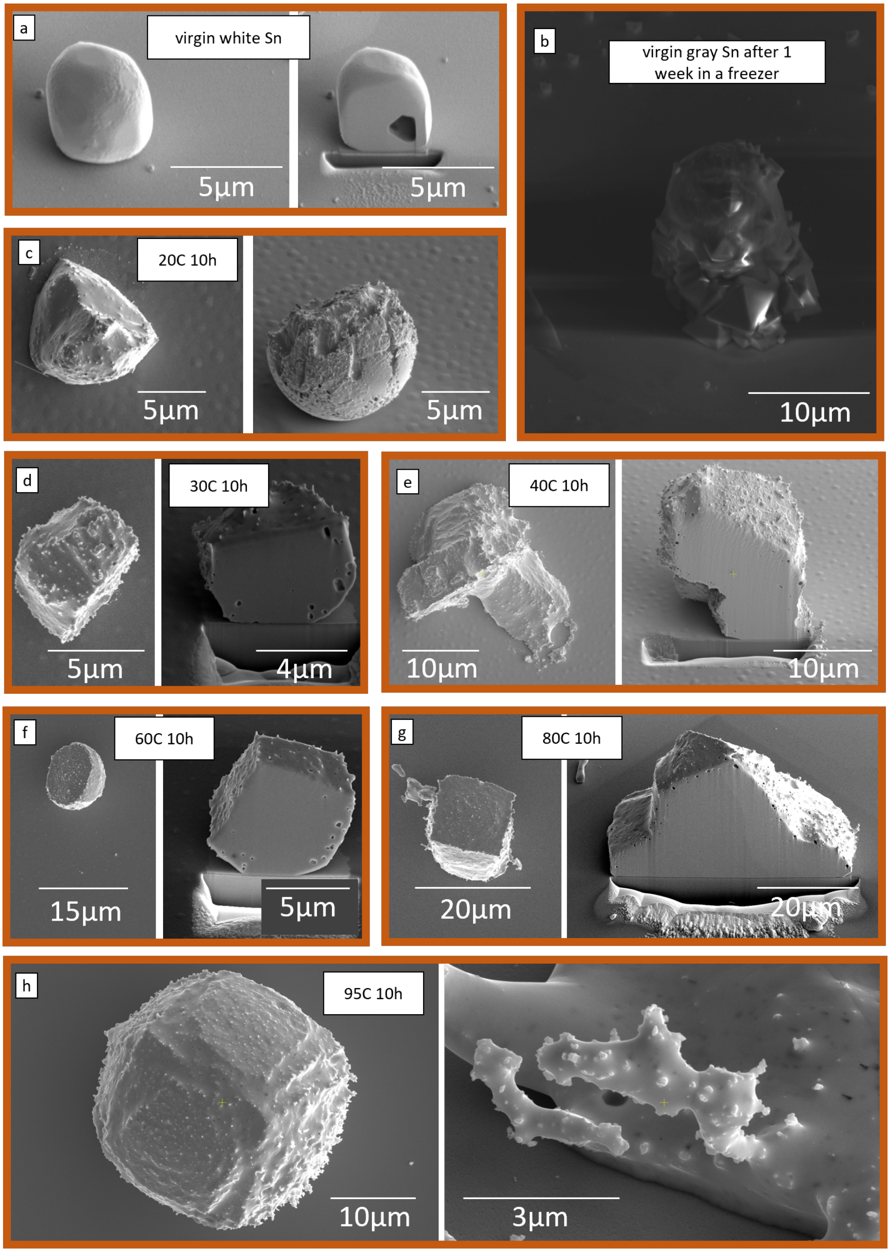

Figure 4.6: SEM/FIB images of virgin and exposed Sn particles (samples 1, 2 and from 6 to 11 from Table 4.1) to hydrogen plasma for 10 h at different temperatures and high ion flux of 20 A/m^2.

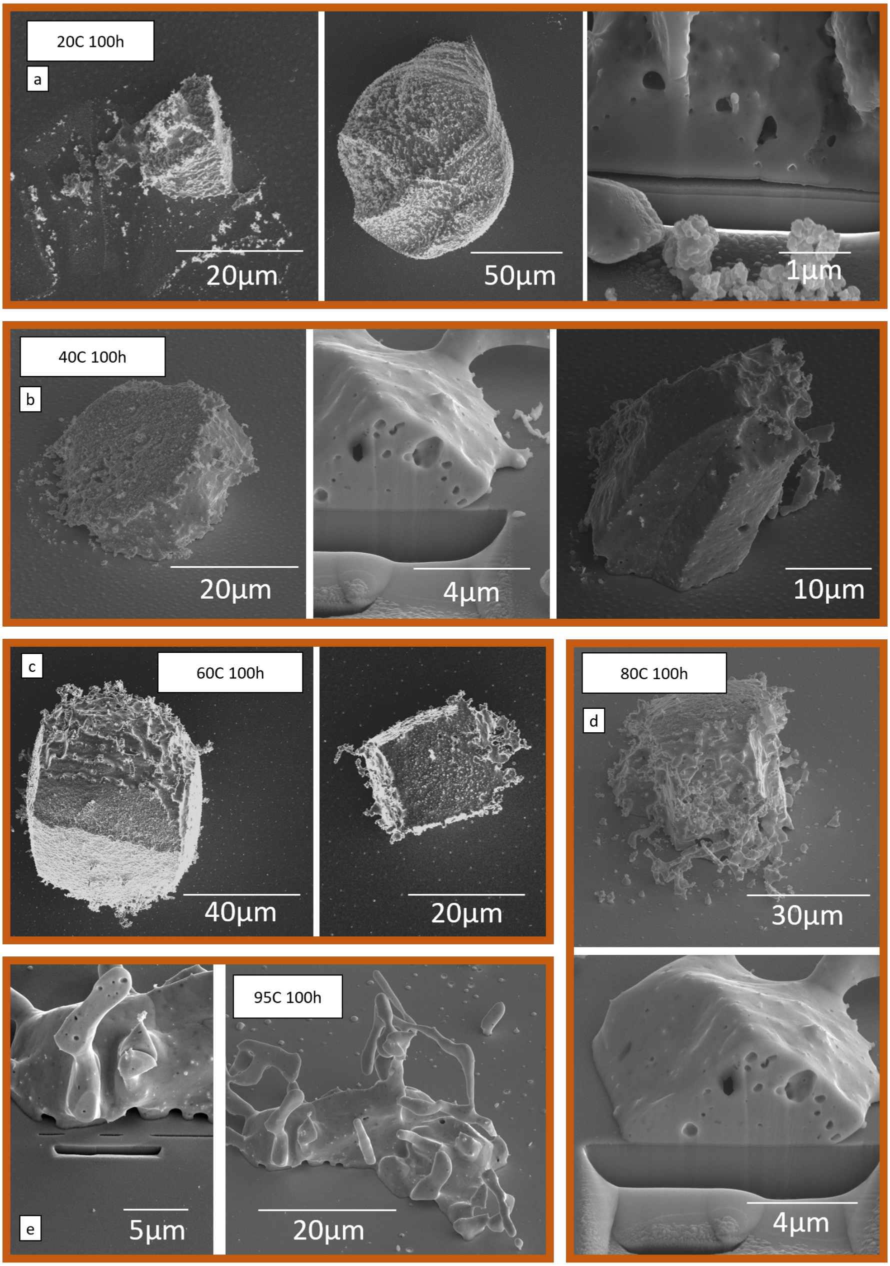

Figure 4.7: SEM/FIB images of exposed Sn particles (samples from 12 to 16 from Table 4.1) to hydrogen plasma for 100 h at different temperatures and high ion flux of 20 A/m^2.

Low temperature effects

For Sn, exposed at low temperature to hydrogen plasma, we found stacked or isolated rhombus structures, that correspond to the cubic lattice of gray Sn (Figure 4.8).

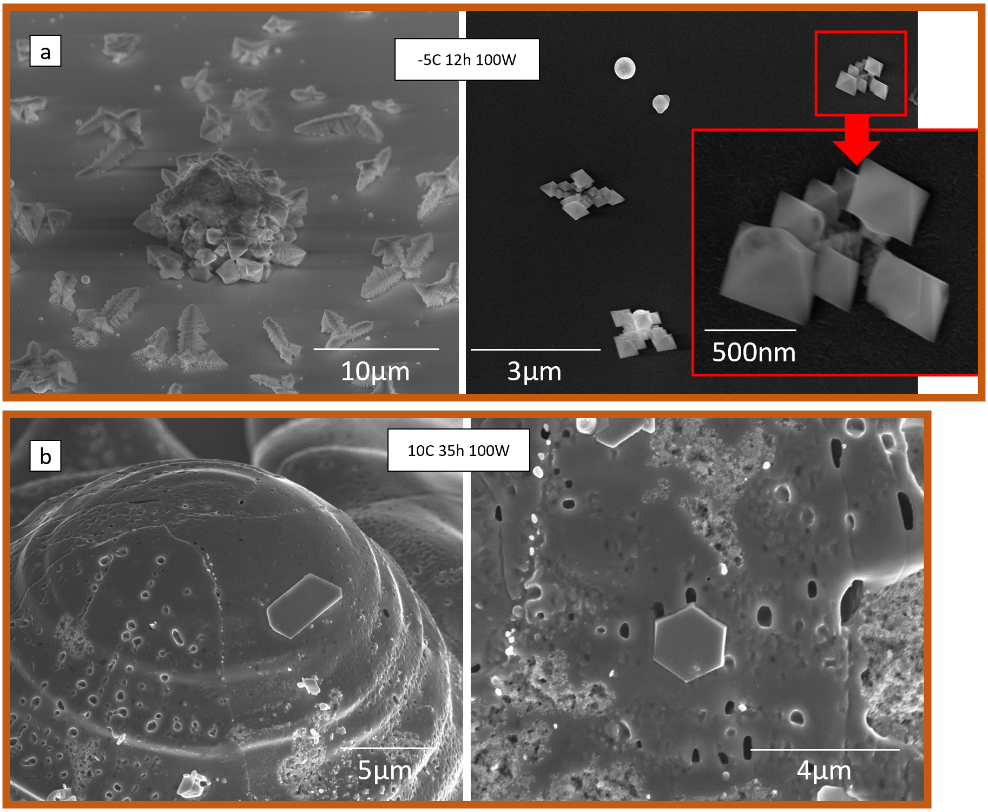

Figure 4.8: SEM/FIB images of exposed Sn particles (samples 3 (a) and 4 (b) from Table 4.1 to hydrogen plasma at an ion flux of 1 A/m^2.

High temperature effects

Firstly, as the temperature increases, the effects of allotropy diminish. Bubbles become spherical, and the metal becomes more plastic. A clear example of this is shown in Figure 4.9, with the Sn particle (Sample 5 from Table 4.1) exposed to 100 °C for 60 h with an ion flux of 1 A/m^2.

Secondly, we observed the transformation of initially spherical tin particles into a cubic shape at temperatures above 50 °C and with an ion flux of 20 A/m^2 (Figure 4.6: f, g, h, and Figure 4.7: c, d). This effect was regular and highly reproducible. Clearly defined facets with pronounced spatial orientation were visible. The explanation for this effect may be related to anisotropic etching. Further investigation is required to

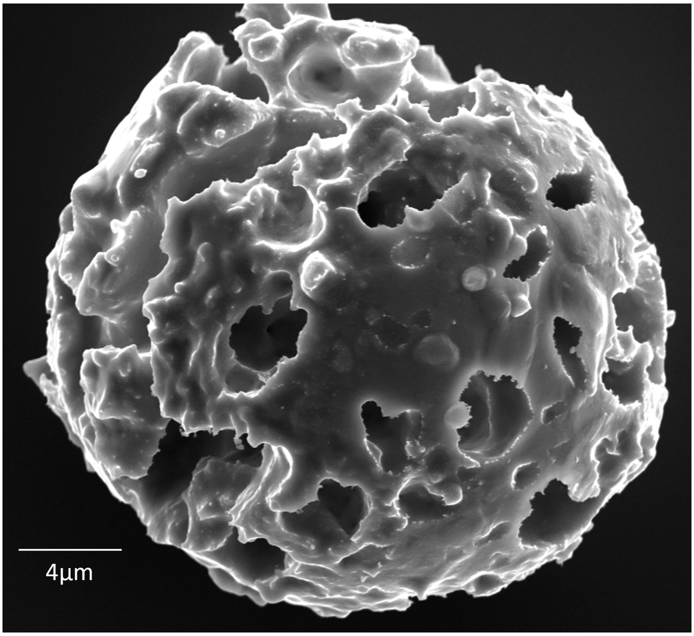

Figure 4.9: Tin particles (sample 5, Table 4.1) exposed to hydrogen plasma at 100 W, 1 A/m^2 and 60 h. The allotropy effects have disappeared. The round bubbles indicate the metallic plastic deformation.

fully understand this phenomenon.

Thirdly, we observed several effects associated with high ion doses. Firstly, we observed blistering of the Cr coating on the substrate, which was not observed in our previous work with exposure to currents of around 1 A/m^2. Upon exposing Sn particles for 100 h at 20 A/m^2, the substrate was covered with ruptured blisters measuring approximately 0.5–1 µm in diameter. Some fragments from the ruptured blisters were ejected and flew away, while others redeposited on the surface (Figure 4.10).

In our observations, we have identified a correlation between the size of detached particle fragments and temperature. At temperatures below 40 °C, a brittle fracture occurs via a crack mechanism, resulting in the formation of large shards comparable in size to the particle itself. At temperatures above 40 °C, the blistering mechanism dominates at the particle's surface, leading to the explosive generation of dozens of nanoparticles (often, 10–100 nm).

4.4 Discussion

For a thermodynamic comparative analysis of transition points between allotropes of tin, gallium, germanium, and silicon a set of PT-phase diagrams is shown in Figure 4.11 [17]. The orange dotted line in the left graph shows the empirical linear

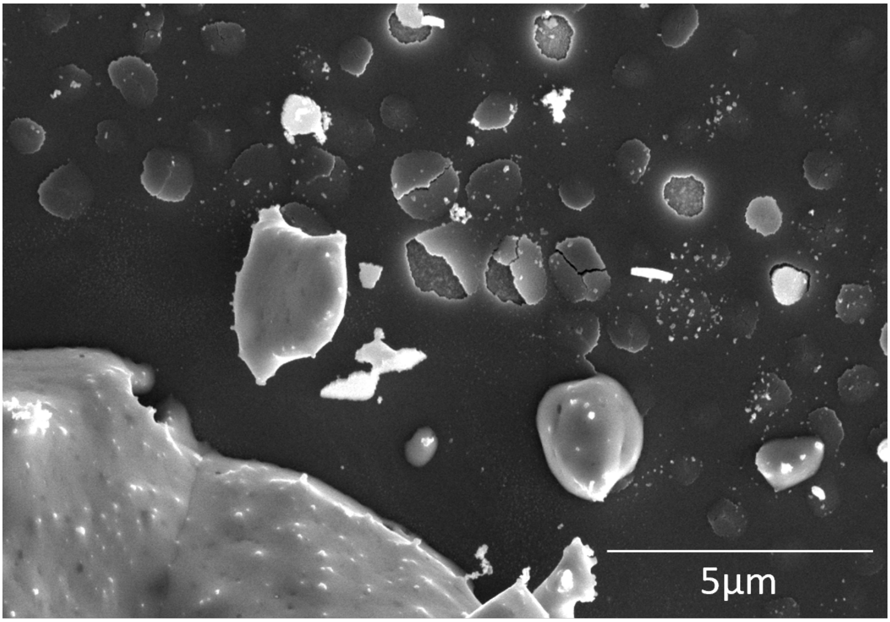

Figure 4.10: Blistering of Cr surface at high ion flux (20 A/m^2) in ECR hydrogen plasma.

approximation of the calculated curves to the intersection point. In the considered analogy, the phase transition points between the two solid phases in the mentioned semiconductors are located in the compression zone at temperatures up to 700 °C and pressures starting at 15 kbar (indicated by yellow squares in the graphs). The allotropy of Sn occurs in the negative pressure (tension) zone. The phase transition point (around -10 kbar) can be obtained through linear extrapolation of curves known from the literature. It should be noted that the theoretical phase transition point at -10 kbar is not achievable, as the ultimate tensile strength (UTS) of the material is only 220 MPa (2 kbar). Based on negative pressure, a shift of the phase transition point toward higher temperatures can be expected. However, the estimation of exact temperature is challenging since the lowest pressure in the diagram must be a flat line P = -200 MPa (-2 kbar) in the temperature range between 250 and 480 K (red line in Figure 4.11).

The extrapolation summary of the Sn phase diagram is listed as follows.

1. First, the extension of the white Sn phase diagram may reach the material's UTS (220 MPa). Microscopic and/or single-crystal Sn particles may have even higher UTS.

2. Second, the liquid Sn phase diagram cannot be extrapolated to tension, since liquids do not have tensile strength.

3. Finally, the extension of the gray Sn phase diagram remains unknown at present, but it is explicitly less stable than white Sn.

One more expectation from the phase diagram extrapolation is the melting of Sn around the bubbles trapped at a temperature significantly lower than 232 °C [26]. This has not been explored in the current work but may be an interesting continuation for future studies, and it may have an impact on the practical applications.

For example, aspherical, faceted bubbles found in Sn, exposed to hydrogen plasma at moderate temperature will possibly turn spherical, due to the effective melting of Sn around a bubble subject to high tension at temperatures about 200–220 °C.

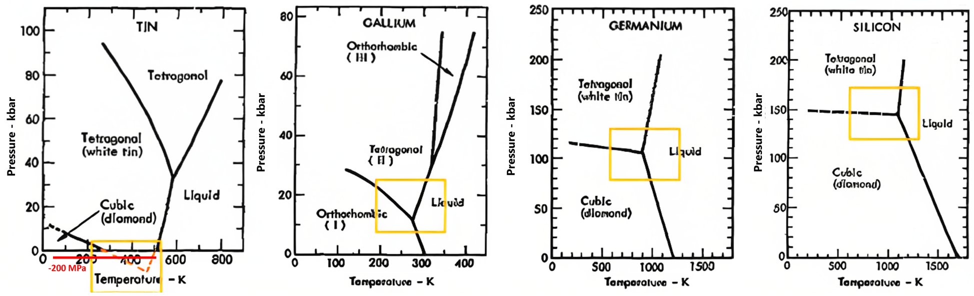

Figure 4.11: Phase PT-phase diagrams of tin, gallium, germanium, and silicon [17]. Note the monotonous behavior of phases near the triple point, where two solid phases and one liquid phase cross. We extrapolated the Sn phase diagram up to Sn's UTS to assess the equilibrium temperature between phases.

4.4.1 Allotrope forms of tin

Kinetics of gray Sn growth

The β-Sn and α-Sn phases are stable and can exist indefinitely long at a maintained temperature. Figure 4.12 illustrates the transformation of a macroscopic β-Sn ingot (approximately 3 cm in length) when kept in a freezer at -40 °C for 11 h. The process of transitioning from the β-Sn to the α-Sn begins with the formation of nucleation sites (seeds). In the depicted experiment, the transformation of the Sn ingot occurred by placing a seed of α-Sn on the edge of the ingot. In the absence of a seed, the initiation of the process may take a considerable amount of time and requires lower temperatures. Once the Sn has transformed into powder form, the process becomes irreversible until the metal is remelted back into the beta phase (microscopic objects disintegrate into powder). When a macroscopic Sn ingot undergoes an allotropic phase transition in air, the conversion of individual flakes is complete, and they are immediately passivated with a native oxide layer. Without a white Sn lattice template, the inverse transition at room temperature for a gray Sn grain is impossible (especially since the surface atoms are locked by the native oxide). However, for small Sn objects such as the micro-particles we have investigated, this may not hold for two reasons:

1. During plasma exposure, the gray Sn seed nuclei may form within white Sn domains (near the maximal tension stress), which promotes its development. If the tension is subsequently relieved (as the trapped bubble deflates after plasma removal), the white phase, which is in close contact with the gray phase and lacks an oxide layer, may consume the gray Sn grains.
2. The experiments are designed to prevent or delay the formation of native oxides, which could potentially contribute to the stabilization of either allotrope phases by immobilizing surface atoms, which are typically more mobile.

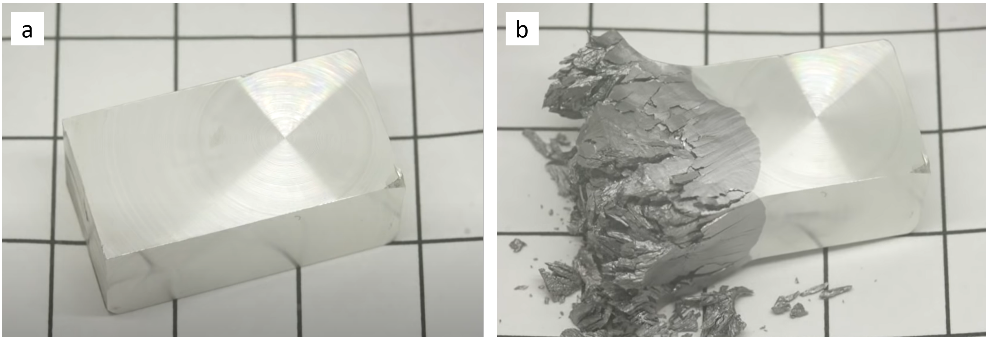

Figure 4.12: $\beta \rightarrow \alpha$-Sn transformation. Figure (a) corresponds to virgin β-Sn, the figure (b) corresponds to the sample maintained at -40 °C for 11 h. Grid size - 1 cm.

The relationship of transformation kinetics was described by JMAK [27] (Johnson–Mehl–Avrami–Kolmogorov). According to JMAK, the formation rate of gray Sn follows from

$$X(t) = 1 - e^{-Kt^n} \tag{4.1}$$

If the kinetics can be accurately represented by the JMAK relationship when the transformation data is plotted according to

$$ln\ ln(1/(1-X)) = n\ ln(t) + ln(K) \tag{4.2}$$

a linear graph is obtained with a slope of n and a y-intercept of $ln\ K$, where X(t) represents the fraction transformed and K and n are constants. Figure 4.13b displays JMAK plots given by Equation 4.2 and represents the isothermal $\beta \rightarrow \alpha$ transformation data shown in Figure 4.13a. The JMAK plots show a close approximation to linear curves within the range of $0.05 < X < 0.95$, with R^2 values of at least 0.993 for the fitting parameters n (2.96, 2.89, 3.17) and K (2.14x, 2.36x, $0.0046{\cdot}10^{-10}$) at the temperatures (-45, -60 and -85 °C) respectively. The deviations from a good fit observed outside the range of $0.05 < X < 0.95$ are likely due to incomplete transformation at the beginning and end of the process.

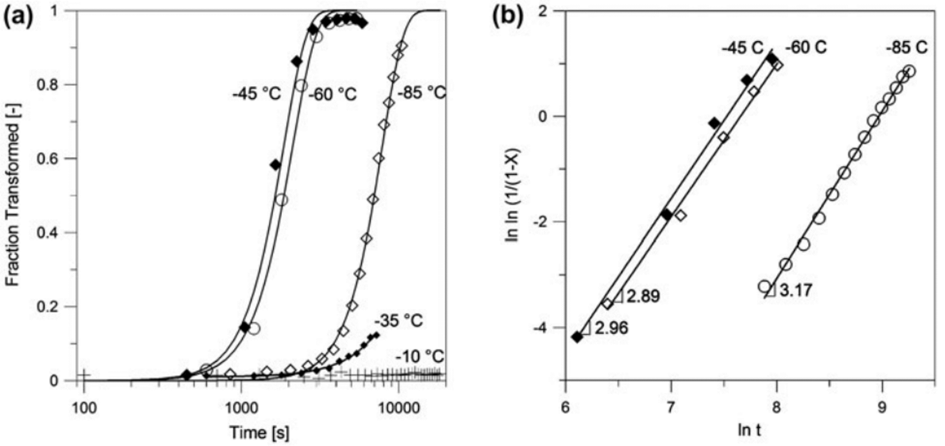

Figure 4.13: Isothermal $\beta \rightarrow \alpha$-Sn transformation curves based on XRD data and (b) JMAK plot of the Equation 4.2. Image source: [10].

The phase transformation process is significantly accelerated when seed nuclei of another phase are present. The transformation process of Sn from the β-phase to the α-phase involves two distinct stages: nucleation and growth. Nucleation occurs when a seed of the diamond cubic unit cell is formed, leading to the generation of α-Sn particles through atomic rearrangement of the β-matrix. The appearance of the first nucleation sites takes up a significant portion of the time. It explains the delay of about 1000 seconds in Figure 4.13 (left graph). Nucleation is more likely to occur at temperatures below 13 °C at atmospheric pressure, as the thermodynamic driving force increases with decreasing temperature. Nucleation generally starts from defects including surface and stressed crystals [8]. Once nucleation emerges, growth proceeds through the $\beta \rightarrow \alpha$ transformation, accompanied by migration of the $\beta \rightarrow \alpha$ interface into the unaffected region of β-Sn. The migration of the $\beta \rightarrow \alpha$ interface represents a delicate balance between the accumulation of lattice stresses and their subsequent relaxation through recovery processes. Stresses arise due to the structural and volume discrepancies between the α- and β-phases, causing atomic bonds to distort and hindering the rearrangement of the crystal structure. The build-up of stress in the lattice impedes the $\beta \rightarrow \alpha$ transformation by inhibiting atomic rearrangement. The transformation $\beta \rightarrow \alpha$-Sn occurs through stress relaxation in zones of plastic deformation within the β-matrix ahead of the migrating interface. Recovery processes play a vital role in stress relaxation by creating, moving, or eliminating dislocations within the β-Sn lattice. These recovery processes aid in the relaxation of stresses, as lattice defects, such as dislocations, undergo dynamic changes. The nucleation of tin pest and the rate at which it grows is determined by the mechanical characteristics of the β-matrix and the rate of stress relaxation. Factors that strengthen the lattice and decrease the mobility of lattice defects act as inhibitors of tin pest formation such as an oxide layer. The oxide layer hardens hydrogen diffusion and slows the nucleation process. Factors that weaken the lattice and increase defect mobility might be attributed to hydrogen and tensile stress.

As the temperature approaches the equilibrium point, more time is required to fully convert the crystal into an alternative phase. The presented graph (Figure 4.13) illustrates the dependence of the conversion time from the β-phase to the α-phase on temperature. It should be noted that the measured curves are valid for macroscopic objects and may differ for microparticles because of their surface tension. Böwering experimentally demonstrated that complete conversion of macroscopic Sn at -24 $°C$ may require over 1000 h [12]. Nogita's findings suggest that the curved shape observed in the plots is a result of the existence of a minor fraction of another phase that becomes incorporated into the main phase. This implies that the α-phase, for instance, may consistently contain inclusions of the β-phase, which could serve as initiation points for the reverse conversion. A similar picture is observed for the process in the opposite direction $\alpha \to \beta$ with similar conclusions [28].

The mechanism of hydrogen diffusion in metals has been extensively studied in situations involving molecular and atomic hydrogen exposure. Most of the studies focused on ITER and related materials such as tungsten. Atomic hydrogen readily diffuses in most metals, with some exceptions. For instance, as previously demonstrated, hydrogen diffusion in PbO crystals is limited due to a high density of dislocations. Hydrogen badly diffuses in silicon or aluminum due to the dense structure of the elementary cell with few interstitial sites. Hydrogen plasma works in three ways to accelerate diffusion into metals: 1) formation of radicals and ions; 2) elevated kinetic energy of ions, but also of radicals that cross the surface barrier; 3) reduction of surface, lowering the surface barrier.

The observed mechanisms can possibly be explained as follows. Radicals and molecular hydrogen are adsorbed onto the particle's surface from all sides, while ions are implanted only on the upper side facing the plasma, penetrating a few nanometers beneath the surface. As ions enter the particle, they become neutral and, together with the radicals, diffuse into the particle's bulk. Consequently, a concentration gradient is formed within the particle, with the maximum concentration of atomic hydrogen at the surface and decreasing toward the center over a diffusion length scale. The typical diffusion coefficient length of atomic hydrogen in metals at room temperature is about 3.3 µm per 1 second [16]. During diffusion in the crystals, atomic hydrogen accumulates at dislocations and other lattice imperfections. At high concentrations of dissolved hydrogen within the crystal, hydrogen atoms energetically prefer to recombine into molecules, forming pressurized gaseous bubbles and deforming the crystal. There is an equilibrium in radical fluxes toward and away from the bubble. The newly appearing H_2 molecules cannot readily escape the particle as the diffusion length of H_2 molecule is lower than H^*. The pressure in the bubbles remains high until the gradient in radical concentration is maintained by plasma inside and on the surface of the particle or until a bubble can be deflated through a developed crack.

Gray Sn growth with and without hydrogen plasma

Based on our experiments, the transition of gray Sn into white Sn occurs differently in the presence and absence of plasma. Under normal atmospheric conditions, when a

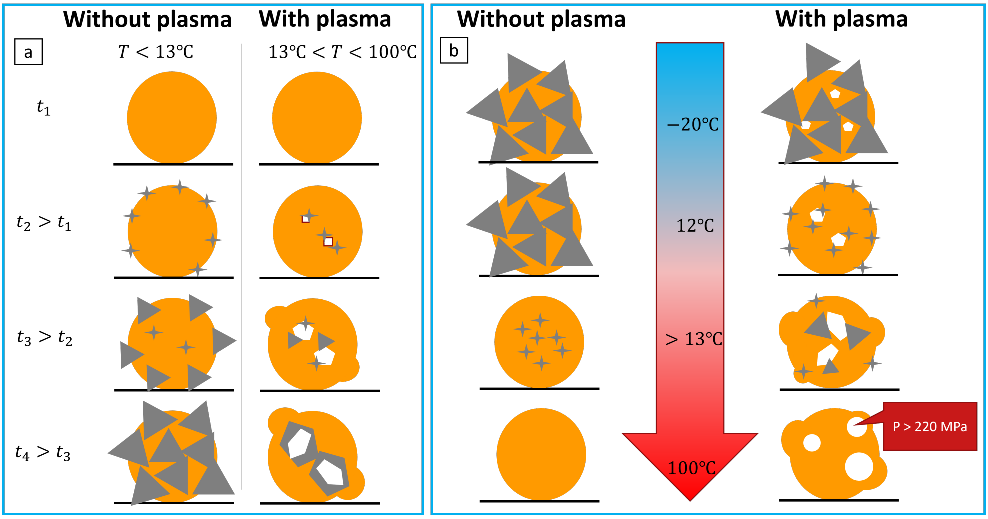

Figure 4.14: Schematic illustration of the gray Sn growth with and without plasma under variation of time (a) and temperature (b). The orange parts indicate white Sn, the dark parts indicted gray Sn, and the white parts indicate cavities or bubbles.

particle of white Sn is subjected to a constant temperature below the critical transition point at 13.2 °C, a grain of gray Sn forms on the surface where atom mobility is highest, and where there are numerous unpaired bonds. Over time, the growing crystal extends from the surface into the particle, restructuring the lattice (Figure 4.14a). However, the situation is different in the presence of hydrogen plasma. The inflated bubble creates enough stress to initiate the growth of the gray phase. In this case, gray Sn grows around the most stressed areas near the bubble. The propagation of gray Sn beyond its stressed region is possible through the mechanisms of cracks, where the propagating crack itself becomes a source of stress (Figure 4.15).

In the case of experiments at various temperatures, as shown, the presence or absence of plasma also leads to differences.(Figure 4.14b) In the absence of plasma, when approaching the critical point (e.g., from negative temperatures toward heating), the appearance of white Sn also occurs from the surface. The higher the mobility the faster the process of conversion and thus further away from the critical point. In the presence of plasma, we observed the presence of cracks and chips, which indicate cohesive (non-plastic) particle failure, supporting the hypothesis of the alpha phase's existence up to approximately 50–60 °C. Thus, the internal pressure created by the bubbles shifted the transition point by about 40 °C. With further temperature increase, the allotropy effects disappear, and all bubbles deform spherically again, i.e., plastically.

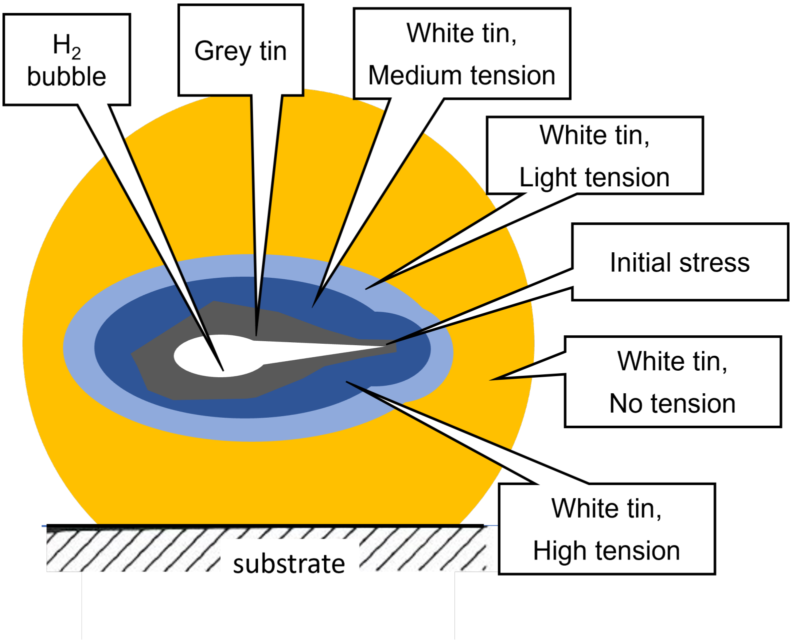

Figure 4.15: Schematic illustration of the crack formation mechanism.

Confirmation of gray Sn existence

To confirm the presence of gray Sn in the particles, attempts were made to diagnose them using additional methods. Specifically, TEM/EDX analysis (Figure 4.16), as well as XRD and diffraction measurements (Figure 4.17) were performed on samples on samples exposed to -5 °C (sample 3, Table 4.1) which visually contains all the signs of gray Sn (we have discussed above that rhombic structures are indicators of a cubic lattice). XRD peaks and diffraction pattern are associated with a tetragonal structure which belongs to white Sn. Thus, all methods confirmed the presence of white Sn only. TEM/EDX measurements on a 100 nm thick lamella revealed only three unoxidized grains (labeled from 1 to 3) of white Sn. The grains were single crystallines, that had not only the same phase but also the same orientation, suggesting that they might have been connected. It suggests that the crystal does not have defects (f.e. stacking faults) and the particle was most likely grown/converted at once.

Small particles have a strong surface tension that makes them different from microscopic objects. The explanation for this might be as follows. After turning off the plasma, the fully converted particle strongly oxidizes due to the hollow structure of gray Sn. What we see is no longer gray Sn, but the oxide that replaced it. The surviving Sn grains in the bulk convert to white Sn. As was shown in Figure 4.14 for the grown β-phase stages, in plasma the gray phase starts nucleation in the bulk. At higher temperatures, gray Sn exists only in the regions of high tension (around bubbles) and quickly converts to white Sn as soon as the hydrogen load has been

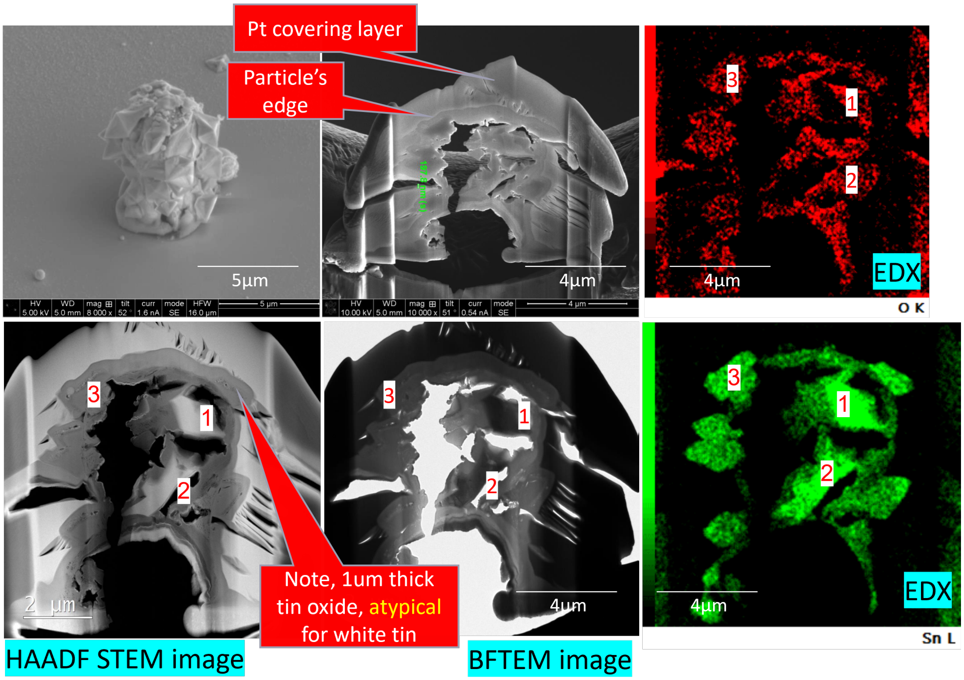

Figure 4.16: TEM measurements taken on the sample 3 from Table 4.1 did not confirm any gray Sn presence. Most of the Sn-containing parts were oxidized and there seem to be only 3 larger Sn crystals grains left, numbered from 1 to 3. The grains were single crystallines, and had the same orientation.

removed. It can be concluded therefore that that XRD and TEM cannot observe gray Sn in micrometer-sized particles.

One can hint at the presence of gray Sn. The exposed particles exhibited thick oxide layers of approximately 1 µm, which is atypical for the native oxide of Sn, which typically has a thickness of around 10 nm [23]. This may indirectly confirm that the particle was at some point in the β-phase state. The β-phase is looser and oxidizes more easily.

4.4.2 Plasma-assisted blistering in tin

Blistering is a prominent degradation phenomenon observed in materials exposed to plasmas. When materials are subjected to hydrogen flux and elevated temperatures, gas-filled cavities or blisters can form beneath the material's surface. Blistering can lead to structural damage, reduced mechanical integrity, and compromised performance of materials in hydrogen plasma applications. The mechanisms behind blister formation in hydrogen plasma environments are complex and multifaceted [29, 30]. One of the primary contributors is hydrogen embrittlement, where hydrogen atoms diffuse into the

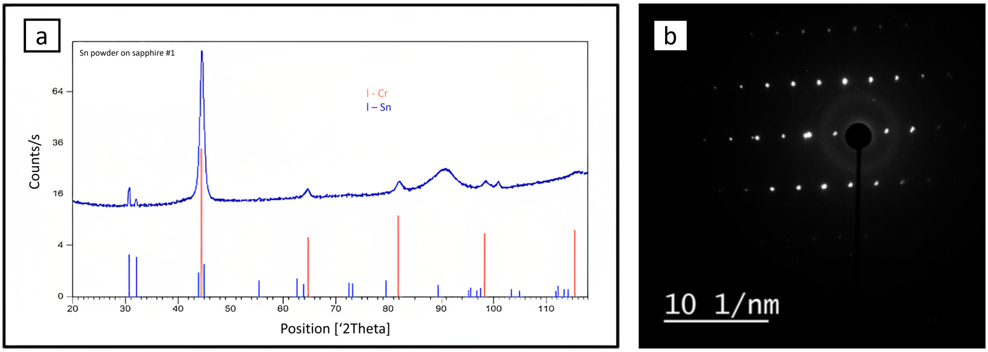

Figure 4.17: XRD (a) and diffraction (b) analyses taken on the sample 3 from Table 4.1 did not confirm any gray Sn presence, the electron diffraction pattern can be indexed with gray Sn only as well. XRD peaks and diffraction pattern are associated with a tetragonal structure which belongs to white.

material's lattice and accumulate at interfaces, weakening the material's cohesion [31]. As the concentration of hydrogen increases, localized pressure builds up, leading to the formation of blisters. The diffusion of hydrogen within the material depends on factors such as temperature, hydrogen concentration, material microstructure, and chemical composition.

One of the primary contributors to blistering is hydrogen embrittlement. Hydrogen atoms diffuse into the material's lattice and interact with the material's microstructure, causing local weakening and embrittlement. This embrittlement can occur through various mechanisms, such as hydrogen trapping at lattice defects, including vacancies, dislocations, and grain boundaries. The presence of these defects provides preferential pathways for hydrogen diffusion, facilitating its accumulation and the subsequent formation of blisters. Hydrogen embrittlement can induce stress concentration within the material due to localized hydrogen accumulation. As hydrogen atoms occupy interstitial positions in the lattice, they create internal pressure within the material. This pressure builds up as more hydrogen atoms accumulate, leading to the growth and expansion of blisters. The increased pressure within the blisters can exceed the material's strength, causing a rupture and the release of gas from the blisters.

In numerous studies, it has been demonstrated that materials with high permeability and solubility of hydrogen tend to form bubbles or blisters. Additionally, materials with low hydrogen permeability can still be susceptible to this effect under sufficient energy if implanted ions (as observed in the case of tungsten walls in ITER) or high doses [32]. Jeong-Ha You described the mechanics of tungsten blistering, showing that tungsten, when irradiated with deuterium ions at an energy of 38 eV/D$^+$, undergoes blistering [33]. In another example, hydrogen diffusion is hindered in densely packed crystals like silicon. The blistering was observed on silicon oxide in near-surface layers [34] and after plasma-assisted ion implantation [29] at high (600 °C) temperatures. The final example of hydrogen plasma-induced blistering formation in aluminum is represented by Quiros [35]. The depth of implantation was shown by the authors using a FIB cross-section. Under the aforementioned conditions, the smallest gas-filled cavities (around 6 µm) reached a depth of a few hundred micrometers.

In addition to hydrogen embrittlement, the formation of hydrides can also contribute to blistering. Certain materials have a propensity to react with hydrogen, forming compounds known as hydrides. Hydride formation can alter the material's properties and introduce stresses and strains. These changes can promote blister initiation and growth, as the formation of hydrides can disrupt the material's cohesive structure and generate internal stresses. The severity of blistering depends on various factors, including the concentration of hydrogen in the plasma, the duration of exposure, the material's strength, ductility, and surface conditions. Higher concentrations of hydrogen in the plasma and longer exposure times increase the likelihood and severity of blister formation. Materials with higher ductility and lower strength are generally more susceptible to blistering. Surface defects, roughness, and contamination can act as nucleation sites for blister formation, facilitating the initiation and growth of blisters.

Furthermore, the growing blister, as it expands, creates a zone of significant stress surrounding the pressurized cavity. Specifically, the normal direction of the growing blister undergoes compression, while the tangential direction experiences tension. Thus, zones with isothermal crystal expansion are formed. The internal pressure inside the blisters, along with continuous pumping by free radical plasma, may facilitate the transition of tin into another allotropic form (at elevated temperatures). Visibly it can be tracked as the appearance of non-spherical bubbles instead of spherical bubbles which are typical for plastic metal expansion.

The phenomenon of the detachment of liquid tin droplets (heated above 800 °C) under irradiation with deuterium ions was demonstrated by Ou *et al.* in an ITER-like hydrogen plasma with a flux $\sim 10^{23}$–10^{26} m^{-2} [19]. In the study, liquid tin was considered a potential material for an inner wall of a fusion reactor due to its lower reactivity compared to lithium, water, and oxygen. Sn also lacks stable hydride formation at and above room temperatures. The experiments revealed significant droplet formation above the melting point due to the bursting of bubbles. The deposited droplets on the target walls were found to contain cavities, suggesting a significant reservoir for Deuterium (D) at this interface, which explains the aforementioned observations. In the case of solid Sn, retention behavior is similar to other solids like molybdenum and tungsten, characterized by a diffusion-dominated depth profile. Furthermore, nanostructuring of the solid Sn surface was observed, attributed to chemical etching by D, resulting in the formation of volatile Sn hydrides. This phenomenon could potentially account for the observed discrepancy between solid and liquid emissions.

4.5 Conclusion

Tin particles deposited from liquid droplet emission using HRG were exposed to hydrogen plasma at different radical doses and temperatures. The aim of this study was to investigate the influence of hydrogen plasma on the embrittlement of tin due to its transition into another allotrope phase.

The following conclusions derived from experiments were obtained during this investigation:

1. Hydrogen plasma is capable of shifting the temperature transition point between the two Sn allotrope phases, white and gray, from 13 to ≅ 60 °C. This is due to the accumulation of molecular hydrogen bubbles within the particle. The pressure within these bubbles creates tensile stress within the crystal, resulting in a shift to higher temperatures on the Sn's PT-phase diagram. The observed effect scales with the flux of incident ions and radicals.

2. The main characteristic indicating the presence of gray Sn in the particles is cohesive fracturing. Cracks and chipping along the edges were observed in particles exposed up to 60 °C. With further temperature increase, gray phase of Sn disappears, and brittle fragmentation is replaced by classical plastic deformation within the metal.

3. Other analysis methods such as XRD, TEM, and diffraction did not confirm the presence of gray Sn in the particles. This may be due to the high surface energy of the particles and their rapid conversion into a more favorable form of white Sn upon hydrogen plasma outgassing and exposure to the atmosphere causes oxidation-induced compression.

4.6 Bibliography

[1] Toshihisa Tomie. Tin laser-produced plasma as the light source for extreme ultraviolet lithography high-volume manufacturing: history, ideal plasma, present status, and prospects. *J. Micro. Nanolithogr. MEMS MOEMS*, 11(2), May 2012.

[2] M Kerkhof et al. Understanding EUV-induced plasma and application to particle contamination control in euv scanners. In Nelson M. Felix and Anna Lio, editors, *Extreme Ultraviolet (EUV) Lithography XI*. SPIE, March 2020.

[3] I Fomenkov et al. Light sources for high-volume manufacturing EUV lithography: technology, performance, and power scaling. *Advanced Optical Technologies*, 6(3-4):173–186, June 2017.

[4] I Fomenkov et al. Laser produced plasma EUV light source for EUVL patterning at 20nm node and beyond. In Patrick P. Naulleau, editor, *Extreme Ultraviolet (EUV) Lithography IV*. SPIE, April 2013.

[5] Dren Qerimi et al. Study of a linear surface wave plasma source for tin removal in an extreme ultraviolet source. *Journal of Vacuum Science & Technology B*, 38(5):052601, September 2020.

[6] Marcus Adrianus van de Kerkhof. *EUV-induced Plasma, Electrostatics and Particle Contamination Control*. PhD thesis, Applied Physics and Science Education, August 2021.

[7] B. Mathiasch. Allotropy of tin. In *Inorganic Reactions and Methods*, pages 76–77. John Wiley & Sons, Inc., May 2007.

[8] Ben Cornelius, Shay Treivish, Yair Rosenthal, and Michael Pecht. The phenomenon of tin pest: A review. *Microelectronics Reliability*, 79:175–192, December 2017.

[9] M. J. Starink. On the meaning of the impingement parameter in kinetic equations for nucleation and growth reactions. *Journal of Materials Science*, 36(18):4433–4441, 2001.

[10] K. Nogita, C.M. Gourlay, S.D. McDonald, S. Suenaga, J. Read, G. Zeng, and Q.F. Gu. XRD study of the kinetics of $\beta \rightarrow \alpha$ transformations in tin. *Philosophical Magazine*, 93(27):3627–3647, September 2013.

[11] Roney L. Thompson, Luiz U.R. Sica, and Paulo R. de Souza Mendes. The yield stress tensor. *Journal of Non-Newtonian Fluid Mechanics*, 261:211–219, November 2018.

[12] Norbert Bowering. Induction of tin pest for cleaning tin-drop contaminated optics. *Materials Chemistry and Physics*, 198:236–242, September 2017.

[13] Norbert Bowering and Christian Meier. Cryogenic cleaning of tin-drop contamination on surfaces relevant for extreme ultraviolet light collection. *Journal of Vacuum Science & Technology B*, 38(6), November 2020.

[14] R. Scott Rowland and Robin Taylor. Intermolecular nonbonded contact distances in organic crystal structures: Comparison with distances expected from van der waals radii. *The Journal of Physical Chemistry*, 100(18):7384–7391, January 1996.

[15] G. W. C. Kaye. *Tables of physical and chemical constants and some mathematical functions*. Longman, London New York, 1986.

[16] H. Wipf. Solubility and diffusion of hydrogen in pure metals and alloys. *Physica Scripta*, T94(1):43, 2001.

[17] David A. Young. Phase diagrams of the elements. Technical report, September 1975.

[18] W.M. Shu, M. Nakamichi, V.Kh. Alimov, G.-N. Luo, K. Isobe, and T. Yamanishi. Deuterium retention, blistering and local melting at tungsten exposed to high-fluence deuterium plasma. *Journal of Nuclear Materials*, 390-391:1017–1021, June 2009.

[19] W. Ou, R.S. Al, J.W.M. Vernimmen, S. Brons, P. Rindt, and T.W. Morgan. Deuterium retention in sn-filled samples exposed to fusion-relevant flux plasmas. *Nuclear Fusion*, 60(2), jan 2020.

[20] Mark van de Kerkhof, Andrei M. Yakunin, Vladimir Kvon, Andrey Nikipelov, Dmitry Astakhov, Pavel Krainov, and Vadim Banine. EUV-induced hydrogen plasma and particle release. *Radiation Effects and Defects in Solids*, 177(5-6):486–512, March 2022.

[21] Dmitry Astakhov. *Numerical study of extreme-ultra-violet generated plasmas in hydrogen.* PhD thesis, April 2016.

[22] W. Ou, F. Brochard, and T.W. Morgan. Bubble formation in liquid sn under different plasma loading conditions leading to droplet ejection. *Nuclear Fusion*, 61(6), May 2021.

[23] F. W. Salt and J. G. N. Thomas. Determination of the oxide film thickness on tin. *Nature*, 178(4530):434–435, August 1956.

[24] Haiyang Niu, Luigi Bonati, Pablo M. Piaggi, and Michele Parrinello. Ab initio phase diagram and nucleation of gallium. *Nature Communications*, 11(1), May 2020.

[25] D. I. Astakhov, W. J. Goedheer, C. J. Lee, V. V. Ivanov, V. M. Krivtsun, O. Yakushev, K. N. Koshelev, D. V. Lopaev, and F. Bijkerk. Numerical and experimental studies of the carbon etching in euv-induced plasma, 2015.

[26] Tin – Melting Point. `https://www.nuclear-power.com/tin-melting-point-boiling-point/`. Accessed: 2023-07-19.

[27] J.W. CHRISTIAN. *The Theory of Transformations in Metals and Alloys*. Elsevier, 2002.

[28] Guang Zeng, Stuart D. McDonald, Qinfen Gu, Syo Matsumura, and Kazuhiro Nogita. Kinetics of the $\beta \to \alpha$ transformation of tin: Role of α-tin nucleation. *Crystal Growth & Design*, 15(12):5767–5773, November 2015.

[29] Paul K. Chu and Xuchu Zeng. Hydrogen-induced surface blistering of sample chuck materials in hydrogen plasma immersion ion implantation. *Journal of Vacuum Science & Technology A: Vacuum, Surfaces, and Films*, 19(5):2301–2306, September 2001.

[30] R A J M van den Bos, C J Lee, J P H Benschop, and F Bijkerk. Blister formation in mo/si multilayered structures induced by hydrogen ions. *Journal of Physics D: Applied Physics*, 50(26):265–302, June 2017.

[31] E. Louis, A.E. Yakshin, T. Tsarfati, and F. Bijkerk. Nanometer interface and materials control for multilayer EUV-optical applications. *Progress in Surface Science*, 86(11-12):255–294, December 2011.

[32] K. Ouaras, K. Hassouni, L. Colina Delacqua, G. Lombardi, D. Vrel, and X. Bonnin. Tungsten dust nanoparticles generation from blistering bursts under hydrogen environment in microwave ECR discharge. *Journal of Nuclear Materials*, 466:65–68, November 2015.

[33] Jeong-Ha You. Mechanics of tungsten blistering: A finite element study. *Journal of Nuclear Materials*, 437(1-3):24–28, June 2013.

[34] Sungjin Choi, Ohmin Kwon, Kwan Hong Min, Myeong Sang Jeong, Kyung Taek Jeong, Min Gu Kang, Sungeun Park, Kuen Kee Hong, Hee eun Song, and Ka-Hyun Kim. Formation and suppression of hydrogen blisters in tunnelling oxide passivating contact for crystalline silicon solar cells. *Scientific Reports*, 10(1), June 2020.

[35] C. Quiros, J. Mougenot, G. Lombardi, M. Redolfi, O. Brinza, Y. Charles, A. Michau, and K. Hassouni. Blister formation and hydrogen retention in aluminium and beryllium: A modeling and experimental approach. *Nuclear Materials and Energy*, 12:1178–1183, August 2017.

Conclusions

This dissertation primarily focused on investigating the behavior of micrometer-sized particles on a substrate under the influence of low-temperature hydrogen plasma. The results of this study are divided into three experimental chapters in this thesis, organized based on the particle analysis methods or experimental conditions. The aim of this dissertation was to complement existing research on the study of the morphology of micrometer-sized particles and propose a new analysis method.

The answers to the research questions announced at the beginning of the thesis are listed below:

Research question I

Research question I: What is the effect of hydrogen plasma on the structure and morphology of micrometer-sized particles?

In this study (see Chapter 2), the influence of ECR-induced plasma on the structure and morphology of micro-particles was experimentally simulated using an ECR plasma, which is 100 times more aggressive in terms of ion flux compared to EUV and energetically comparable to a typical EUV-induced plasma inside an EUV scanner. All the obtained effects using ECR plasma can be considered as accelerated 100 times with respect to an EUV-induced plasma.

Two mechanisms leading to changes in morphology of Sn, Pb and PbO micrometer-sized particles were identified. The first mechanism involves the formation of volatile hydrides on the surface of the particles. Stable hydrides are likely able to desorb from the surface and contribute to etching. Volatile metal-hydrides require breaking of multiple metal-metal atomic bonds and replacing those with metal-hydrogen passivation (e.g. Sn requires 3 or 4 hydrogen atoms to become volatile as SnH_3 or SnH_4). If the intermediate hydride formation steps are sufficiently stable to break all metal-metal and/or metal-oxide bonds, the metal-hydride will be able to desorb from the surface and the particle will etch in hydrogen plasma. As the stability of the intermediate hydrides decreases, a larger portion of them will dissociate on the surface before desorbtion, resulting in increased surface migration of atoms and morphology changes rather than etching. The second mechanism is the inflation and rupture of pressurized bubbles beneath the particle's surface, which is associated with the increased absorption and subsequent diffusion of ions and hydrogen radicals within the particle bulk and their accumulation into bubbles of molecular hydrogen. We studied a set of materials including Si, Sn, Pb, PbO, stainless steel, Zn, Ni, CeO, and melamine, and classified them according to the aforementioned mechanisms.

Both mechanisms of formation of volatile hydrides and accumulation of bubbles in EUV-induced can affect micro-particle adhesion and contribute to contamination.

Visually, these described mechanisms can manifest differently, such as a reduction in particle size, fragmentation, blistering, or promoting allotropic transformation.

Research question II

Research question II: Can Laser Light Scattering (LLS) be used as an in-situ diagnostic method to monitor the adhesion and morphology of particles exposed to plasma?

Laser Light Scattering (LLS) accompanied by long-distance microscopy was proposed as a diagnostic method for in-situ monitoring of the morphology of micrometer-sized particles. LLS offers an advantage over traditional SEM post-characterization due to its non-invasive in-situ manner. LLS is sensitive to adhesion of particles, their sizes, shapes, and composition (optical properties), and thus can be utilized as a diagnostic method which has been demonstrated in the governing Chapter 3.

LLS was used to demonstrate the influence of different stressors, such as a plasma or a directed gas jet on the morphology of micrometer-sized particles. LLS enabled simultaneous in-situ monitoring of hundreds of particles and allowed to study the sensitivity of different materials to these stressors statistically. Particles of a few micrometers in size obey the Mie scattering theory: the scattered intensity is proportional to the particle cross-section (r^2 of the particle, where r is the radius) and depends on multiple parameters such as n, k, and D/λ, as well as the polarization of the incident and collected light. LLS was calibrated on pre-defined melamine resin spheres with narrow size distribution using Mie theory. The effectiveness of the method was demonstrated based on an example of Si particles, the etching behavior of which is known from the literature.

A set of materials studied in LLS including Si, Sn, Pb, PbO, stainless steel, Zn, Ni, and CeO in LLS. The measurements demonstrated that the influence of hydrogen plasma affected the adhesion of the particles to the surface, their sizes, and their reflective properties as was predicted. We observed the shrinkage of Si and Sn particles, fragmentation of Pb, PbO, and CeO particles, and evaporation of Zn particles. Hydrogen plasma did not affect the adhesion of stainless steel particles but displayed a change in reflectivity over time. The response of Ni particles was non-trivial and is open for interpretation.

In addition, for comparison, Sn and PbO particles were exposed to noble plasma (argon plasma) to exclude a chemical component. Due to the heavy mass of argon ions, the exposed particles were subjected to possible physical sputtering, atom displacements, and argon implantation. Soft PbO particles with lower yield strength were severely damaged while rigid Sn particles did not undergo visible changes. The lack of damage for Sn particles by heavier argon ions proves that plasma chemistry (radical or ion-assisted chemistry) is the dominant mechanism in interaction with hydrogen plasma.

Research question III

Research question III: Can hydrogen plasma cause allotrope transformations of tin micrometer-sized particles?

The influence of hydrogen plasma on the behavior of Sn particles has been studied, revealing several important findings. Hydrogen plasma has the capability to shift the temperature transition point between the white and gray allotrope phases of Sn from 13.2 °C (at normal pressure) to elevated temperatures (between 40 and 60 °C. This shift is attributed to the formation of molecular hydrogen bubbles within the particles, which creates internal tensile stress and causes the transition to occur at higher temperatures. The effect scales with the ion flux.

One key characteristic indicating the presence of gray Sn in the particles is cohesive fracturing, observed through the occurrence of cracks and chipping along the particle edges. Cohesive fracturing results in acceleration of Sn etching/removal, but may also result in delamination of larger pieces and their emission from Sn particles. As the temperature further increases, the effects of allotropy (and subsequent cohesive fracturing) diminish, and the brittle fracturing is replaced by classical plastic deformation and blistering of smaller particles.

Interestingly, conventional analysis methods such as XRD, TEM, and diffraction techniques did not confirm the presence of gray Sn in the particles. This discrepancy may be attributed to the high surface energy of the particles, leading to their rapid conversion back to the more favorable white Sn form when the hydrogen plasma exposure ceases and they are exposed to the ambient atmosphere.

General conclusion

Overall this work contributed to the understanding of hydrogen plasma's impact on the morphology of micrometer-sized particles and their adhesion to surfaces exposed to plasma. Applications, such as those in EUV lithography, may benefit from the gained knowledge.

List of publications

Journal publications with peer-review

- D. Shefer, A. Nikipelov, M. van de Kerkhof, Z. Marvi, V. Banine, and J. Beckers, *The impact of hydrogen plasma on the structure and morphology of tin and lead micrometer-sized particles*, Journal of Physics D: Applied Physics, vol. 56, no. 8, Feb. 2023. DOI: 10.1088/1361-6463/acb3d9.

- D. Shefer, A. Nikipelov, M. van de Kerkhof, V. Banine, and J. Beckers, *Laser light scattering (LLS) to observe plasma impact on the adhesion of micrometer-sized particles to a surface*, Journal of Physics D: Applied Physics, vol. 56, no. 45, Feb. 2023. DOI: 10.1088/1361-6463/aceb02.

In revision

- D. Shefer, A. Nikipelov, M. van de Kerkhof, V. Banine, and J. Beckers, *Morphology change and release of tin and lead micro-particles from substrates in hydrogen plasma*, Physica Scripta (AOP Science).

Conference materials

- D. Shefer, A. Nikipelov, M. van de Kerkhof, V. Banine, and J. Beckers, *Morphology change and release of tin and lead micro-particles from substrates in hydrogen plasma*, Proceedings SPIE Extreme Ultraviolet (EUV) Lithography XII, online conference, Feb. 2021 10.1117/12.2581666.

Conference contributions

Poster presentations

- D. Shefer, A. Nikipelov, V. Banine, and J. Beckers, *The effect of hydrogen plasma on the adhesion of tin and lead micro-particles to a substrate*, Physics at Veldhoven, online conference, Jan. 2021.
- D. Shefer, A. Nikipelov, M. van de Kerkhof, V. Banine, and J. Beckers, *Adhesion and removal of tin and lead micro-particles on substrates in hydrogen plasma*, SPIE Extreme Ultraviolet (EUV) Lithography XII, online conference, Feb. 2021
- D. Shefer and J. Beckers, *Observation of morphological transformation of lead and tin microparticles in hydrogen plasma*, Physics at Veldhoven, Jan. 2022

Acknowledgments

Looking back after four years of dedicated work on my Ph.D. project, I have come to realize how many people contributed to its realization. Without their involvement, this project would have been incomplete or may not have materialized at all. This dissertation owes its success primarily to **Andrey**, a person who, from our very first meeting, provided unwavering support and became a close friend. **Andrey**, thank you for infusing purpose into my endeavors, consistently taking the time to review my drafts, and engaging in stimulating conversations. I also want to extend my heartfelt gratitude to my supervisors: **dr.ir. Job Beckers** and **prof.dr. Vadim Banine**. **Job**, I cannot imagine anymore pursuing my Ph.D. under anyone else's guidance. Thank you for your patience, constant involvement, unwavering assistance with any questions, and your unyielding spirit, which inspired us during the most challenging times. **Vadim**, without your sensitive guidance, sparkling sense of humor, and continuous involvement, this project would have been impossible. I am endlessly grateful for your motivation and selfless participation in addressing any concerns. I owe this degree to another person as well. **Mark**, I am delighted that fate brought us together, and that you became a crucial participant in this project. You consistently brought a fresh and unconventional perspective to scientific challenges, and I found great pleasure in our collaborative discussions. I would also like to express my deep gratitude to **Ab**, **Pieter**, and **Jürgen** for their technical and organizational support in the laboratory. I also deeply appreciate help with the setup development from **Peter** from EPC group. Without your contribution, this project would not have been completed, probably. Thanks to **Beatriz** for her assistance with SEM/FIB/EDX measurements and to **Marcel** for his help with TEM measurements. And a special thank you to **Zara** for our collaborative work on my first paper.

I would like to extend my gratitude to my office colleagues, both past and present: **Siebe**, **Shahriar**, **Federico**, **Parwez**, **Rick**, **Marlous**, **Patrick**, **Boy**, **Saman**, **Tim Steps**, **Tim Donders**, **Guido**, **Sim**, **Judith**, and **Jovana**, for your participation and willingness to respond at any moment. Our conversations during breaks have been invaluable. Many thanks to **Ludo**, my former Bachelor student. We made together

the very first runs of the setup and had a lot of fun. Big thanks to our group secretary **Anita**. Your attitude and energy have always fascinated me. Thank you for your sincere support and help in the organizational moments.

I want to express special thanks to my group leader at ASML, **Seth Brussaard**. Thank you for reading my papers and organizing the workflow. Thanks to you, I had the opportunity to work in the company's state-of-the-art laboratories and get acquainted with its cutting-edge activities.

Special appreciation must be conveyed to someone who has been supporting me practically every day for many years, even before my arrival in the Netherlands. Thanks to him I learned how to program, which eventually became a significant part of my Ph.D. This man with a big heart also generously designed the cover of this dissertation. **Evgeny Vicktorovich**, these words of gratitude are for you.

I also thank my EPG group and the head of our department, **prof.dr.ir. G.M.W. Kroesen**, for holding shared events and keeping the group together as a team.

I want to express my gratitude to **my family and close relatives** for their support during difficult times and for their assistance in shaping my path.

Dear mentors, colleagues, friends, and family, I would like to shake each of your hands. I appreciate your contributions. Without all of you, this Ph.D. would never have come to fruition.

Curriculum Vitae

Dmitry Shefer
Novosibirsk, Russia
Born on 13 April 1993.

Working experience

2019 - 2023 | Doctoral Candidate (full-time)
Eindhoven University of Technology, Eindhoven, the Netherlands

2016 - 2018 | Research engineer
OCSiAl group, Novosibirsk, Russia

2013 - 2016 | Laboratory assistant
Rzhanov Institute of Semiconductor Physics, Novosibirsk, Russia

Education

2016 - 2018 | Master of Physics
Novosibirsk State University, Novosibirsk, Russia

2011 - 2016 | Bachelor of Physics
Novosibirsk State University, Novosibirsk, Russia